3-2005

Creep Behavior of an Oxide/Oxide Composite with Monazite Coating at Elevated Temperatures

Sean S. Musil

CREEP BEHAVIOR OF AN OXIDE/OXIDE COMPOSITE WITH MONAZITE COATING AT ELEVATED TEMPERATURES

THESIS

Sean S. Musil, 1st Lt, USAF

AFIT/GAE/ENY/05-M14

DEPARTMENT OF THE AIR FORCE
AIR UNIVERSITY

AIR FORCE INSTITUTE OF TECHNOLOGY

Wright-Patterson Air Force Base, Ohio

The views expressed in this thesis are those of the author and do not reflect the official policy or position of the United States Air Force, Department of Defense, or the U.S. Government.

AFIT/GAE/ENY/05-M14

CREEP BEHAVIOR OF AN OXIDE/OXIDE COMPOSITE WITH MONAZITE COATING AT ELEVATED TEMPERATURES

THESIS

Presented to the Faculty

Department of Aeronautics and Astronautics

Graduate School of Engineering and Management

Air Force Institute of Technology

Air University

Air Education and Training Command

in Partial Fulfillment of the Requirements for the

Degree of Master of Science in Aeronautical Engineering

Sean S. Musil, BS

1st Lt, USAF

March 2005

AFIT/GAE/ENY/05-M14

CREEP BEHAVIOR OF AN OXIDE/OXIDE COMPOSITE WITH MONAZITE COATING AT ELEVATED TEMPERATURES

Sean S. Musil, BS

1st Lt, USAF

Approved:

/signed/	11 Mar 05
Dr. Marina Ruggles-Wrenn (Chairman)	Date
/signed/	4 Mar 05
Dr. Shankar Mall (Member)	Date
/signed/	16 Mar 04
Dr. Theodore Nicholas (Member)	Date

Abstract

The aerospace industry has a growing need for high temperature structural materials which can withstand extreme sustained loading for use in future reusable propulsion technologies . This thesis examines one of these materials developed by the Materials and Manufacturing Directorate of the Air Force Research Lab (AFRL/ML), an oxide/oxide ceramic matrix composite (CMC), Nextel 610/monazite/alumina ($N610/LaPO_4/Al_2O_3$). This CMC consists of a porous alumina matrix reinforced by Nextel 610 fibers coated with monazite in a symmetric cross-ply $(0^o/90^o/0^o/90^{o)}s$ orientation. Monazite is an oxidation-resistant interfacial coating which was designed to inhibit oxidation and improve high temperature behavior. The material containing the uncoated fibers, $N610/Al_2O_3$, while able to withstand the high temperatures of combustion, did not however, display a level of creep resistance suitable for use.

To characterize this material, monotonic tensile tests to failure and stress-rupture (creep) tests were performed at room temperature and at elevated temperatures between 900^oC and 1200^oC. Modulus, stress and strain were monitored during the tests to characterize failure mechanisms. Residual strength of all specimens that survived 10^6 seconds in creep was also characterized. Microstructural analysis and optical microscopy were performed on all fracture surfaces. $N610/LaPO_4/Al_2O_3$ was found to have improved creep behavior over the material containing the uncoated fibers at elevated temperatures.

Acknowledgements

I would like to thank the following people for their assistance during the course of my thesis: my faculty advisor, Dr. Marina Ruggles-Wrenn, for her guidance and support throughout the course of this work, Kristin Keller (AFRL/MLLN) for providing the test specimens, her expertise on ceramic matrix composites, and initial guidance on the scanning electron microscope (SEM), Dr. Joseph Zelina (AFRL/PRTC) and Dr. Ronald Kerans (AFRL/MLLN) for their sponsorship of my thesis, Barry Page for set-up and assistance with all test equipment, Andy Pitts and Jay Anderson for their technical support, fellow students Capt Scott Cunningham for his companionship and Capt Lee Harlan for his assistance during the early testing stages, and most importantly my very supportive wife for always being there for me.

Sean S Musil

Table of Contents

Page

Page

List of Figures

Page

Page

Page

Page

Page

List of Tables

Page

CREEP BEHAVIOR OF AN OXIDE/OXIDE COMPOSITE WITH MONAZITE COATING AT ELEVATED TEMPERATURES

I. Introduction

Although composite materials are at the forefront of aviation technology, their origin can be traced back some 3,000 years ago to Ancient Egypt where straw was used as reinforcement in clay bricks for building purposes. Composite materials were sought after for their strength as compared to monolithic materials. With the discovery of more durable construction materials like metals, the interest in organic fibers was lost. It wasn't until the 1950s that the use of composite materials really began to rise with the advent of fiberglass, where glass fibers in a tough resin matrix could be produced on a large scale (8).

Since the use of aluminum began in the 1920s, composites have been the most important materials adapted for use in aviation. Composites began their history in the aviation industry in the 1950s when fiberglass made up some two percent of the structure of the early Boeing 707s. The military began researching the use of composites in the 1960s, investigating the possibility of using boron or graphite fibers in an epoxy resin for aircraft control surfaces. Production use of the boron-epoxy composites was first seen in the horizontal stabilizers of the Navy's F-14 Tomcat (8).

Since then, the use of composites has continued to grow and has become increasingly important in the aerospace industry where the search for stronger, lighter

materials is always the focus. Today, the interest of the aerospace industry is in materials which can withstand extreme loads at high temperatures. For those reasons, ceramic matrix composites (CMCs) have become the focus of investigation. They consist of ceramic fiber reinforcement in a ceramic matrix. While ceramics on their own are too brittle for use in aerospace applications, CMCs are engineered with significantly more toughness. Although CMCs are extremely strong and have the highest operating temperatures of any material, they are still susceptible to the harsh environment of the turbine engine in which oxidation occurs and becomes the primary failure mechanism.

Oxide/oxide materials have been developed where both the fiber and matrix are oxide based ceramics, such as alumina, which are inherently oxidation resistant. While oxide/oxide CMCs do show increased oxidation resistance, they still do not perform up to the levels needed for production use in aerospace applications. To further increase oxidation resistance, investigation into various fiber coatings has taken place in recent years. One such coating under investigation is monazite. It provides a weak interface between the fiber and matrix which causes the fibers to debond in the presence of an approaching matrix crack. This allows the fibers to withstand the load as the matrix fails, prolonging the life of the composite. The present study investigates the use of monazite coating in a Nextel 610/Alumina composite and characterizes the creep performance of the composite at elevated temperatures.

The sections to follow will describe this research effort. First, a brief review of CMCs will be conducted along with a discussion of pertinent research in this area. Then an overview of the material being tested, N610/$LaPO_4$/Al_2O_3, will be presented. Next, the experimental techniques and apparatus used in this study will be explained. Then the

experimental results obtained through this research will be examined. Finally, concluding remarks and recommendations for future research will be given.

II. Background

This chapter begins with a broad introduction to the basics of ceramic matrix composites (CMCs). A description of the characteristics of CMCs and their applications, especially those in the United States Air Force (USAF), will then be given. Next, factors that currently limit the use of CMCs are described, focusing on oxidation at elevated temperatures. Methods of inhibiting oxidation are then reviewed, including a discussion on the oxide/oxide class of CMCs and fiber coatings. Then, a summary of most recent research in the area of ceramic matrix composites, especially oxide/oxide composites and Nextel oxide fibers, will be give. Finally, the objective of this study will be explained, which is to investigate the creep behavior of the Nextel 610/monazite/alumina composite.

Ceramic Matrix Composites

Fibers

Ceramic fibers provide high strength and high elastic modulus, along with high temperature capability. For these reasons, ceramic fibers are very important as reinforcements in high-temperature structural materials (9:37). Ceramic fibers are categorized primarily on the basis of fiber size. They are typically either produced as multifiber tows consisting of 100-1000 smaller diameter fibers (5-15 μm) or as larger monofilaments (50-100μm) produced individually. Monofilament fibers are produced mainly for use in metal matrix composites, which are matrix dominated, where the large diameters do not limit the composite by introducing flaws on the same scale as the fiber

diameter. In CMCs, the use of smaller diameter fiber tows causes a reduction in scale of microstructural defects associated with the fibers (28:15).

Ceramic fibers can also be divided into non-oxide and oxide fibers. Non-oxide fibers are made up of primarily silicon carbide (SiC). Examples of SiC based fibers include Nicalon, Tyranno and Sylramic (31). Other non-oxide fibers are created using silicon nitride, boron carbide, and boron nitride (9:49). Oxide fibers are mostly alumina (Al_2O_3) based and may contain small amounts of SiO_2. Some examples of those are the Nextel 610, 650, and 720 fibers created by 3M or yttrium-aluminum garnet (YAG) created by General Atomics (31). Oxide fibers are designed to be inherently oxidation resistant. A drawback to oxide fibers is that they are currently extremely expensive.

Table 1 below, from DiCarlo et al (14), summarizes the key properties needed in a continuous ceramic fiber for use as reinforcement in high temperature continuous-fiber ceramic matrix composite, along with the benefit gained from each property.

Table 1. Summary of Key Fiber Properties and CMC Benefits

Fiber Property	CMC Benefit
• High Modulus	• Improves CMC stiffness and reduces matrix stresses
• High As-Produced Strength	• Improves CMC toughness and ultimate strength
• High Thermomechanical Stability	• Improves CMC as-fabricated strength, CMC strength retention and creep resistance during service
• High Oxidative Stability	• Improves CMC service life in oxidizing environments
• Small Diameter	• Improves matrix strength and facilitates fabrication of thin and complex-shaped CMCs
• Low Density	• Improves CMC specific properties for weight-sensitive applications and reduces stresses in CMC rotating components
• Low Cost	• Reduces CMC cost and improves CMC commercial viability

Matrix Materials

Ceramic matrix materials possess the ability to withstand very high temperatures, which has made them very desirable for use in high temperature structural composites. Metallic super-alloys, designed for use in jet engines, can only withstand temperatures up to 800^{o}C or as high as 1000^{o}C with an oxidation resistant coating. Above that temperature is where ceramics are required. Ceramics are made up of one or more metals combined with a nonmetal such as oxygen, carbon, nitrogen, or boron. They are generally stoichiometric, or have a fixed ratio of cations to anions. Some examples of that include alumina (Al_2O_3), silicon carbide (SiC), and silicon nitride (Si_3N_4).

Ceramic matrix materials can be categorized into glassy (amorphous) or crystalline matrices (28:13). Crystalline ceramics require higher processing temperatures than glass ceramics, which can cause damage to fibers. Ceramics matrices have very high elastic moduli, low density and high strength. The major disadvantage of ceramic matrices is that they are extremely brittle. This along with low thermal and mechanical shock resistance has put the emphasis toward developing tougher ceramics. Glass ceramics have the ability to achieve high densities at low processing temperatures. High density means low porosity and better mechanical properties, while low processing temperatures reduces the amount of damage to fibers. However, glass-ceramics are not capable of withstanding as high a temperature as polycrystalline ceramics (31:2-2).

Ceramic matrix materials can also be categorized as non-oxide and oxide matrices. Common non-oxide ceramic matrix material include silicon carbide, silicon nitride and titanium diboride. Oxide type ceramic matrix materials are most commonly alumina or zirconia. Oxide ceramics are inherently oxidation resistant, whereas non-oxide ceramics rely on a layer of silica (SiO_2) to prevent oxidation. Susceptibility of the silica layer to environmental degradation is a big problem for non-oxide ceramics.

Ceramic Fiber Coatings

In the earliest ceramic composites, fiber/matrix interfacial layers were formed by the degradation of the fiber. These layers were sufficiently weak and fractured from stress concentrations caused by approaching matrix cracks, protecting the fiber. The resulting debonding of the fiber and matrix allowed the composite to still carry a load while the matrix was cracking. However, environmental degradation of this interfacial layer has

limited the use of such composites (25:521). For this reason, the need arose to produce fiber coatings which would provide the weak fiber/matrix interface and also withstand environmental degradation. Oxide/oxide composites with sufficiently porous matrices have also shown the ability deflect matrix cracks and allow fiber/matrix debonding. In composites with dense matrices, interfacial coatings are necessary to provide the weak interface.

Fiber coatings such as boron nitride (BN) and carbon have been widely used in ceramic composites; however, their use is limited because they readily oxidize at elevated temperatures. In recent years, the emphasis has been on developing oxide fiber coatings which are inherently oxidation resistant and still able to produce the weak fiber/matrix interface.

Interfacial coatings also prevent degradation of the fiber through interaction with the matrix material. One example of that is Nextel 610 fiber which has show to degrade through interaction with a fine grained alumina matrix when sintered at 1200^{o}C (23:667). Nextel 610/Alumina composites will be examined in this investigation. An oxide fiber coating which has exhibited weak bonding and chemical stability to alumina is monazite ($LaPO_4$). This thesis will focus on the effect of monazite coating on the Nextel 610 fiber in an alumina matrix.

The two most common morphological defects associated with fiber coating have been fiber bridging and incomplete fiber coverage. Figure 1 and Figure 2, from Davis et al (12), illustrate fiber bridging and incomplete fiber coverage respectively.

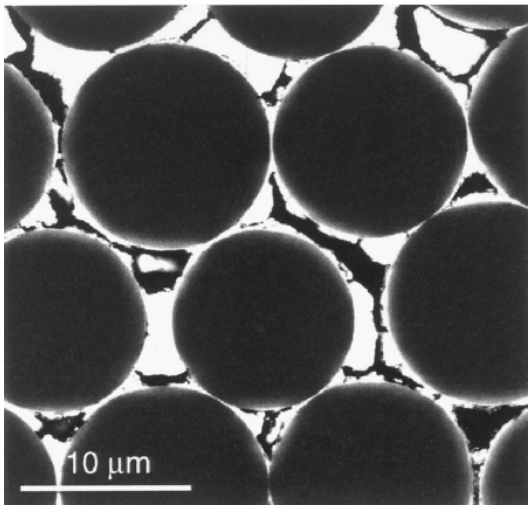

Figure 1. Fiber Bridging

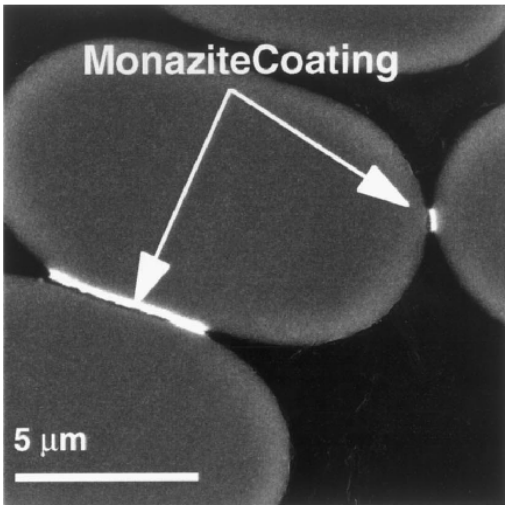

Figure 2. Incomplete Fiber Coating

Fiber bridging occurs when coated fibers bond together in bundles and limit infiltration of matrix between fibers. When fiber coating coverage is incomplete, the ability of the coating to create a weak interphase is lacking and fiber matrix bonding occurs causing embrittlement of the composite (12:584).

Fabrication of Ceramic Matrix Composites

In general, CMCs are developed in a two stage process. First, a reinforcement phase is incorporated in to an unconsolidated matrix, followed by matrix consolidation. For composites containing coated fibers as reinforcement, an additional step is needed up front to coat the fibers. During the fiber incorporation stage, fibers must also be aligned. The most common technique for fiber incorporation is the slurry infiltration process. This process involves a fiber tow being passed through a tank containing slurry (matrix powder, carrier liquid and organic binder) and then wound onto a drum or take-up wheel

and dried. The resulting “tape” is then cut in sections, stacked in the desired fiber orientation and consolidated.

Many techniques can be used to consolidate the matrix; however, hot pressing is the most commonly used of those techniques. Hot pressing produces composites with very superior quality provided the thermal mismatch between the elements of the composite is low. Cold pressing followed by sintering is another technique for consolidation. This process involves a lot of matrix shrinking during sintering and the resulting composite has a lot of cracks. Other techniques include melt infiltration, in situ chemical reaction, and sol-gel and polymer pyrolysis. Melt processing produces a virtually pore-free, high density matrix, but requires very high temperatures. In situ chemical reactions include chemical vapor deposition (CVD) and chemical vapor infiltration (CVI). Sol-gel and polymer pyrolysis techniques have been successful, but often yield high shrinkage and repeated impregnations are needed to produce a substantially dense matrix (9).

Two considerations must be observed when pairing together a matrix material with a fiber: thermal compatibility and chemical compatibility. High processing temperatures coupled with the low ductility of ceramics, lead to matrix (or fiber) cracking during cooling when a thermal mismatch is present. Thermal strain in a composite is proportional to $\Delta\alpha\Delta T$, where $\Delta\alpha$ is the difference between the linear coefficient of thermal expansion of the fiber and that of the matrix and ΔT is the change in temperature. Chemical compatibility prevents degradation at the fiber matrix interface at elevated processing and heat treating temperatures. Degradation can be caused by chemical reactions between the materials or phase changes in either component.

Properties of CMCs

Ceramic matrix composites offer a variety of attractive mechanical properties including high stiffness, high strength, low thermal expansion, and extremely high melting temperatures.

In CMCs, relative elastic modulus values of the fiber and matrix, as the ratio of E_f/E_m determines the amount of matrix microcracking. Failure strains for CMCs tend to be rather low compared to those of polymer matrix composites (PMC) or metal matrix composites (MMC). In both PMCs and MMCs, the failure strain of the matrix is much higher than that of the fiber. The situation is reversed in CMCs. In a PMC or MMC, the fibers fail first at their weak points and the composite fails at the location of the most fiber fractures. For CMCs two situations can occur. In strongly bonded CMCs, the fiber and matrix fail at the matrix failure strain, whereas in a weakly bonded CMC the matrix would start to crack, then the fibers would bridge the cracks and it would finally fail according to the failure strain of the fiber. Since fibers are the stronger link in CMCs, the weaker interface is desirable (9).

Of particular interest to military applications of CMCs are low dielectric constant materials, such as oxides and nitrides, which allow absorption of RF energies in the radar wavelengths (9).

Aerospace Applications

The aerospace industry has been a major thrust in the research and development of ceramic materials. Among the areas of greatest interest in the benefits of ceramic materials are spacecraft, space communication, and propulsion technologies. Ceramics

are being sought after for their high specific strength, low specific weight, low thermal expansion, and their ability to retain strength at elevated temperatures. Ceramic matrix composites also offer improved damage tolerance over monolithic ceramics.

Propulsion technologies are particularly interested in CMCs for their ability to improve thrust-to-weight ratios. This ratio can be increased by decreasing weight, increasing thrust, or both. The low specific weight inherent in CMCs allows for significantly lighter structures compared to those created from metal alloys. Achieving higher thrust values requires increasing turbine inlet temperatures. Technology advances over the past few decades have increased inlet temperatures to over 1300^{o}C with the use of single crystal metal superalloys. In order to increase turbine inlet temperatures any further would require the use ceramics, especially those able to withstand environmental degradation at such high temperatures (32:2-11).

The space environment experiences large temperature variations, between -160^{o}C and 93^{o}C, which become an obstacle when trying to maintain precise alignment of communication and sensor systems. The high stiffness and low thermal expansion coefficients of CMCs, makes them very attractive materials for use in space communication applications. High strength becomes secondary in the weightlessness of the space environment. An example of that is the mechanical arm of the space shuttle, which is made of graphite-epoxy composite. On earth the arm would not even be able to support its own weight of 411 kg, but in space it is designed to handle payloads of up to 24,500 kg (34:5). Other space applications include portions of the space shuttle and future space planes, which need to withstand extreme temperatures. Space planes in

particular will fly at speeds and altitudes at which equilibrium temperatures are far hotter than those experienced by the space shuttle (34:1)

An example of CMC applications in advances propulsion systems is the Integrated High Performance Turbine Engine Technology (IHPTET) program. This collaborative effort was started in 1987 between the Army, Navy, Air Force, NASA, DARPA and industry to double aircraft propulsion capability by 2005. The purpose of IHPTET is to meet future engine performance goals by the use of advanced materials, innovative structural designs, and improved thermodynamics. Among the accomplishments of IHPTET using CMCs are SiC/SiC composite liners for combustor walls, low and high pressure turbine vanes utilizing 3-D fiber architectures, hybrid bearing using ceramic elements, and C/SiC exhaust nozzles which require no cooling (33).

Other aerospace applications of CMCs include F-16 afterburner flaps, rocket nozzle extensions, and rocket-engine thrust chamber components. Afterburner flaps in the General Electric F110 turbofan engine used in the F-16 experience temperatures in excess of 1000^{o}C. Nickel based superalloy, Rene' 41, has been used to create these flaps, but demonstrate excessive creep deformation resulting in shorter than intended life spans. As a replacement material, CMCs are being tested by the Air Force Research lab because of their ability to resist creep when exposed to temperatures above 1000^{o}C for extended times (30: 2-13). Currently carbon/carbon nozzles are being use on the upper stage engine built by Pratt & Whitney for the Delta III launcher. The use of CMCs in thrust chambers not only reduces weight, but also provides resistance to thermal shock and stability to chemical attack from liquid propellants (29:410).

Oxidation

Oxidation occurs in CMCs when they are exposed to the oxygen in air at elevated temperatures and is the biggest limiting factor in high temperature applications. The effect of oxidation is a shorter life at elevated temperatures and limitations on use at those temperatures. It is of particular concern in composites containing carbon where at elevated temperatures the carbon is eventually completely dissipated away in the form of carbon monoxide or carbon dioxide. This includes composites such as carbon/carbon (C/C), carbon/silicon carbide (C/SiC), and silicon carbide/silicon carbide (SiC/SiC). These composites have excellent high temperature strength, but they readily oxidize at high temperatures. In C/SiC composites a thermal mismatch between the fiber and matrix cause matrix cracks during the cool-down stage of processing. These cracks allow oxygen to reach and attack the fibers. SiC/SiC composites use a pyrolytic carbon fiber coating to allow fiber/matrix interface debonding. When the composite is loaded beyond the tensile strength of the matrix, the matrix will crack allowing oxygen to attack the carbon coating (30:24). Figure 3 is a schematic representation of the progression of oxidation of a coated fiber through a matrix crack (20).

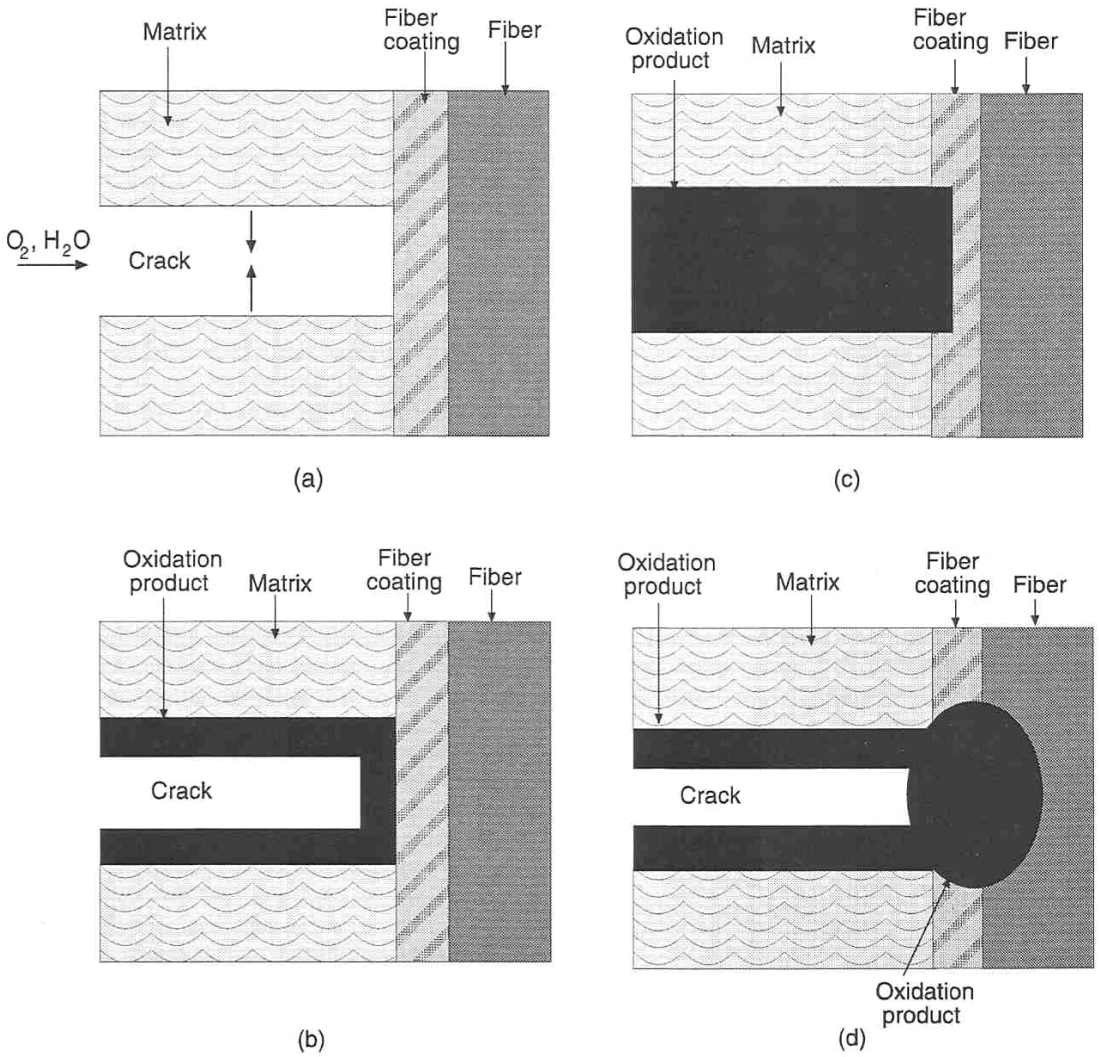

Figure 3. Schematic Representation of Oxidation Progression through a Matrix Crack

Oxidants, such as oxygen and water vapor, diffuse through an open matrix crack, oxidizing the sides of the crack and fiber coating as shown in Figure 3a. Next, the oxidation product begins the fill the crack area, reducing its width, as depicted in Figure 3b. In Figure 3c, the crack has been sealed by oxidation products before the coating was oxidized, preventing significant damage to the fiber/coating/matrix interface. In other

cases, the coating may become breached by oxidation prior to the crack sealing and oxygen may still diffuse through the oxidation product of the fiber coating and continue to oxidize the fiber, as shown in Figure 3d (20).

Composites containing carbon, boron nitride or SiC are all susceptible to embrittlement by the infiltration of oxygen through matrix cracks which attacks the fiber/matrix interface. The ability of the interface to enable debonding and crack bridging is severely inhibited by this oxidation. This process substantially limits the use of such composites at elevated temperatures, by requiring them to operate below the matrix cracking stress level. This deficiency has prompted the search for CMCs comprised of environmentally stable (oxidation resistant) oxide components (27:2077).

Overcoming Oxidation

The family of oxide/oxide composites has been developed to combat the issue of oxidation at elevated temperatures. Development of all-oxide composites has progressed along two separate microstructural design paths. The first method is based on producing a weak fiber/matrix interface. This method requires the use of stable oxide fiber coatings to create the weak interface between the fiber and a dense matrix. The second method utilizes the formation of a strong interface, but builds upon it by using a porous matrix to provide crack deflection paths. In the latter case, design and microstructural stability are critical. Matrices need to be sufficiently low in toughness to enable crack deflection, but still able to maintain strength. The objective is to produce a matrix with fine, uniformly distributed porosity (27:2077). The first method requires proven oxide interfacial coatings, such as monazite, which not only provide the weak interface, but are also

oxidation resistant and chemically stable with the composite constituents. The composite in this investigation will follow this approach by using a monazite coating on a Nextel 610 fiber, comprised of over 99% alumina, in an alumina matrix.

Previous Work

Over the past few years, significant research has been accomplished in the area of oxide/oxide ceramic matrix composites.

The potential for monazite to promote crack deflection was first demonstrated by Morgan and Marshall in 1995. Since then Monazite coatings have been tested on numerous fiber/matrix combinations. Chawla et al tested monazite coating on Saphikon (single crystal α-alumina) fibers in an alumina matrix (10). Their results showed that monazite coating was an effective method of creating weak interfacial bonds between monazite and alumina. Much research has been done using a monazite coated Nextel 610 fiber in an aluminosilicate matrix. Cazzato et al (14), were also able to show that the monazite coating could produce a weak interface, however, they also observed decreased tensile strength and strain to failure in specimens with the monazite coating. This was attributed to the fiber coating technique and fiber bridging caused by clumped tows of coated fibers (7). Investigations have also been performed on monazite coated Nextel fiber tows, in an effort to determine the effect of various monazite precursors on fiber strength (4).

Most of the recent research has focused on unidirectional composites, while it still remains a challenge to demonstrate monazites effectiveness as a weak interface material in 2-D laminated composites. Little investigation has been performed on cross-ply

laminated composites involving monazite coated fibers. Also, because of Nextel 720 fiber's improved creep resistance over the Nextel 610 fiber, a lot of research has been done with coated and uncoated N720 in both alumina and aluminosilicate matrices. N610 fiber has also been investigated, primarily uncoated in aluminosilicate matrices. One extensively research composite of that nature was the General Electric Gen-IV. Results from Zawada et al (37) show fairly poor creep resistance of the N610 fiber which limited the composite's use at temperatures above 1000^{o}C.

This investigation will focus on the Air Force Research Laboratory, Materials and Manufacturing Directorate developed N610/Monazite/Alumina composite. Keller et al (22) tested the effectiveness of monazite coating after long-term exposure to elevated temperatures. The investigation looked at both N610/Monazite and N610/Monazite/Alumina composites exposed to temperatures of 1100^{o}C and 1200^{o}C for varying lengths of time. Samples with uncoated fibers showed significant strength loss after short term exposure at 1200^{o}C, while samples with monazite coated fibers showed a smaller initial reduction in strength, but remained constant through 1000 h at 1200^{o}C. Push-out testing demonstrated that the matrix/monazite/fiber interface was weak and became weaker after longer-term thermal exposure (22).

Little to no creep-rupture testing has been preformed on the cross-ply N610/Monazite/Alumina composite prior to this investigation.

Thesis Objective

The objective of this thesis will be to characterize the creep behavior of the Nextel 610/Monazite/Alumina composite. As previously mentioned, oxidation is the largest

problem facing high temperature use of CMCs. It occurs when a composite is exposed to elevated temperatures for extended periods of time at certain stress levels. Creep-rupture testing, which involves sustained loading under elevated isothermal conditions, is the best way to demonstrate a composites ability to withstand oxidation and retain strength in high temperature applications. Resistance to creep at elevated temperatures is vital to the long term durability required for high temperature aerospace applications.

III. Material and Specimen

This section will discuss in detail the material under investigation. Nextel 610/Alumina and Nextel 610/Monazite/Alumina will be compared and contrasted on both microstructure and material properties. The actual test specimens will then be discussed, including processing of the material, specimen shape and tabbing of the specimens.

Nextel 610/Alumina vs. Nextel 610/Monazite/Alumina

Nextel 610/Alumina and Nextel 610/Monazite/Alumina composites used in this investigation were developed by the Materials and Manufacturing Directorate of the Air Force Research Lab, AFRL/MLLN, located on Wright-Patterson Air Force Base, Ohio.

Nextel 610 Fiber (N610)

The fiber reinforcement used to develop both composites under investigation is the Nextel 610 (N610) fiber developed by the 3M Corporation. It was developed in the mid 90s to have uniquely high tensile strength and creep resistance. It is almost entirely made up of alumina, an oxide of aluminum. While most commercially available fibers contain silica or other non-crystalline phases, Nextel 610 is fully crystalline. N610 fibers are essentially pure (>99%) poly-crystalline alumina, α-Al_2O_3, and contains no glassy phases. This improves creep resistance, as amorphous phases would become viscous at elevated temperatures. This also allows the fiber to retain its strength at high temperatures (1). Fully crystalline fibers containing high amounts of α-Al_2O_3 are also very chemically

stable which leads to environmental stability in corrosive atmospheres. Table 2 lists typical properties of the N610 fiber as reported by the manufacturer.

Table 2. Properties of Nextel 610 Fibers

Composition (wt %)	
Al_2O_3	>99
SiO_2	0.2 - 0.3
Fe_2O_3	0.4 - 0.7
Average Grain Size (μm)	0.1
Filament Diameter (μm)	10 - 12
Density (g/cm^3)	3.88
Tensile Elastic Modulus (GPa)	373
Tensile Strength (MPa)	3100

As seen from the table, the average grain size within the fiber is only 0.1 μm. In oxides with grains that small, creep rate is inversely proportion to grain size. Figure 4, from Johnson et al, is a Nextel 610 fiber showing its uniform, high density microstructure with grain size of ~100 nm (20).

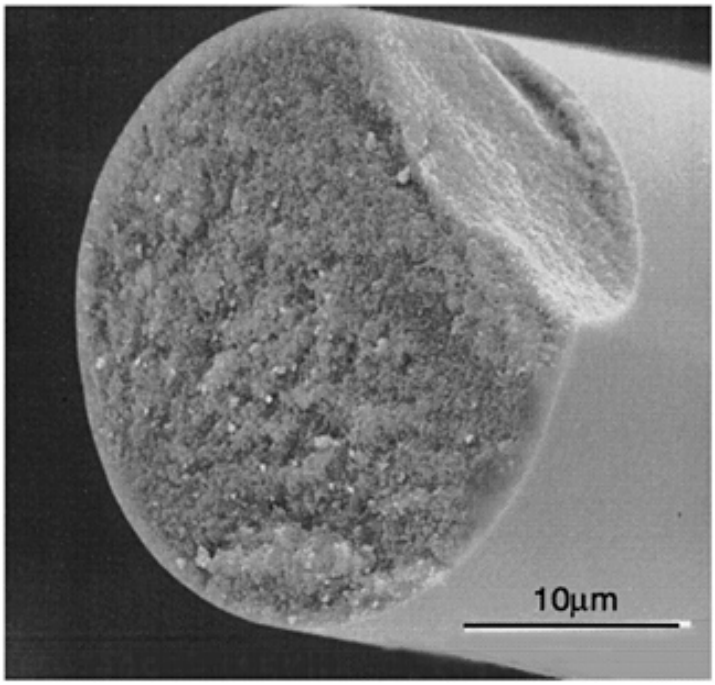

Figure 4. Fine-grained Nextel 610 Fiber

Nextel 720 is another commercially available fiber developed by 3M. It is made up of approximately 85% α-Al_2O_3 and 15% SiO_2 forming α-Al_2O_3 /Mullite. Its mullite content with an average grain size of 0.5 μm leads to higher creep resistance. However, its lower content of alumina and larger overall grain sizes lend to a significantly lower tensile strength of 2100 MPa (2). Thus, fine grain size and high content of alumina are advantageous for high strength. Fine grained alumina does also have its drawbacks. At elevated temperature it is susceptible to large amounts of grain growth with cause loss of retained strength. Grain growth is inhibited in N720 by the addition of mullite which causes reduced grain boundary sliding allowing it to retain more strength at higher temperatures.

Alumina Matrix

Al_2O_3 is also used as the matrix material for the composite under investigation. Alumina exists in only one stable form, α-alumina. It typically has strengths in the 300-900 MPa range, depending on grain size. For crystalline alumina, the strength is around 300 MPa, but is tougher than its amorphous counterpart due to inherent crack bridging ability. Additional properties include a modulus of 380 GPa and a coefficient of thermal expansion of 8.8 x $10^{-6}/^{o}$C (26). As previously mentioned, alumina is an oxide of aluminum, and therefore oxidation resistant. At temperatures above 800^{o}C, alumina has shown a friction coefficient of 0.40, the same as at temperatures below 200^{o}C (38: 115). Low friction coefficient reduces friction with fibers during pull-out prolonging failure.

During the sintering stage of processing, shrinkage can occur at 1100^{o}C, but actual sintering does not occur until 1400^{o}C (38:112). The sintering temperature for the composite in this investigation was 1200^{o}C, causing matrix shrinkage and microcracking in the matrix during processing. This is an inherent flaw in CMCs which require high processing temperatures.

Monazite Coating

In order to retain the oxidation resistance inherent in an oxide/oxide composite, oxide fiber coatings are most commonly used. Over the past 15 years, many oxidation resistant fiber-matrix interphase coatings have been investigated, and the most successful coating has been monazite, $LaPO_4$. It was first investigated by Morgan and Marshall in 1995 (22). They found LaPO4 to have a modulus of 133 GPa and a coefficient of thermal expansion of 9.6 x $10^{-6}/^{o}$C (26). Monazite is an encompassing name for the lanthanide

phosphate class of compounds. Its success stems from the ability to create a high energy or "weak" interface with the alumina fiber. This allows the interface to debond readily in the presence of the stress intensity caused by a propagating crack. This process is referred to as "non-wetting". Another benefit of monazite coating is relatively machinable and soft with a melting temperature of 2072^{o}C (6:2793), well above the temperature range of the other composite elements. Monazite also proves to be chemically stable with alumina when it is present in a stoichiometric lanthanum-to-phosphate ratio (La:P ratio of 1:1). Nonstoichiometric monazite can severely degrade the fiber strength and affect the ability of the interface to debond. This has been one of the most significant obstacles to overcome in the coating process.

The N610 fibers used in this investigation were coated with monazite using a sol-gel dip coating technique. This technique allows for better reproducibility of coating thickness and requires a low processing temperature. Low processing temperature reduces not only fabrication cost, but also the potential for coating degradation and interaction of the fiber and coating during processing (10). Solution based precursors allow the stoichiometric ratio to be controlled accurately; however, obtaining continuous, uniform, bridge-free coatings proves difficult (20).

Composite Microstructure

Figure 5 is a schematic of the microstructural design of the Nextel610/Monazite/Alumina composite. The top image depicts both 90^{o} (left-to-right) and 0^{o} (out-of-the-page) plies. Tows of ~ 400 fibers are clearly visible in the 0^{o} ply. Subsequent images within the figure depict higher magnification schematics of the

microstructure, showing both the coated fibers and the continuous network of alumina particles that make up the matrix.

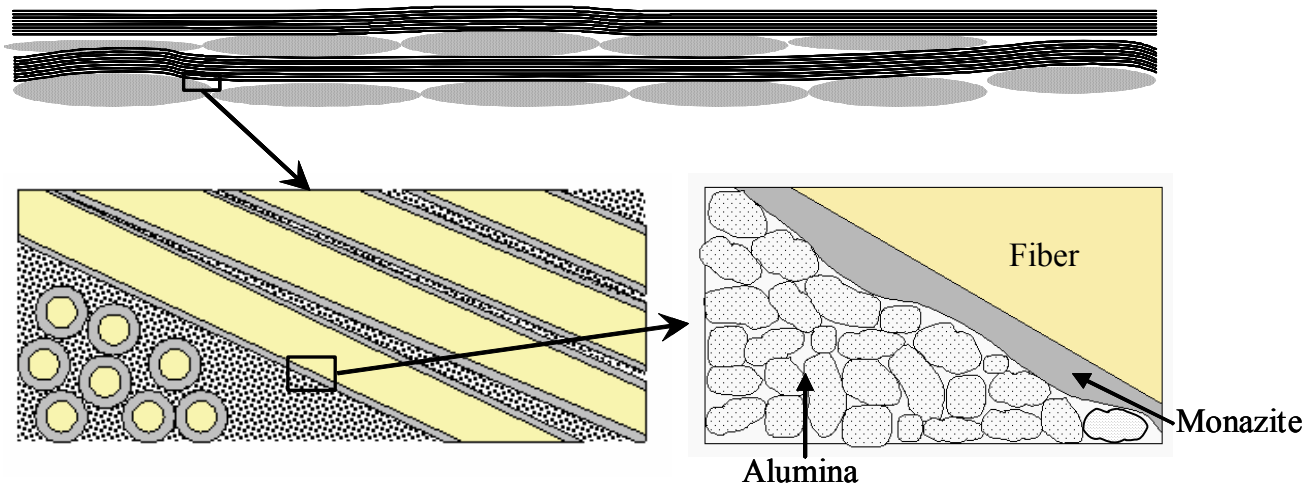

Figure 5. Microstructural Design Schematic for Nextel 610/Monazite/Alumina

Composite Fabrication

Processing

Nextel 610 fiber tows were desized in air at 1100°C and then coated with a monazite precursor solution at a rate of ~5 cm/s in an 1100°C furnace. The monazite sol was washed multiple times to remove any residual ions which could cause loss of fiber strength after coating. After coating, the fiber tows were filament wound onto a take-up wheel without any sizing used over the coating. Fibers were then drawn through a slurry and wound into a tape on a drum using an AFRL/MLLN developed filament winder. A schematic of the slurry infiltration process is shown in Figure 6 (9).

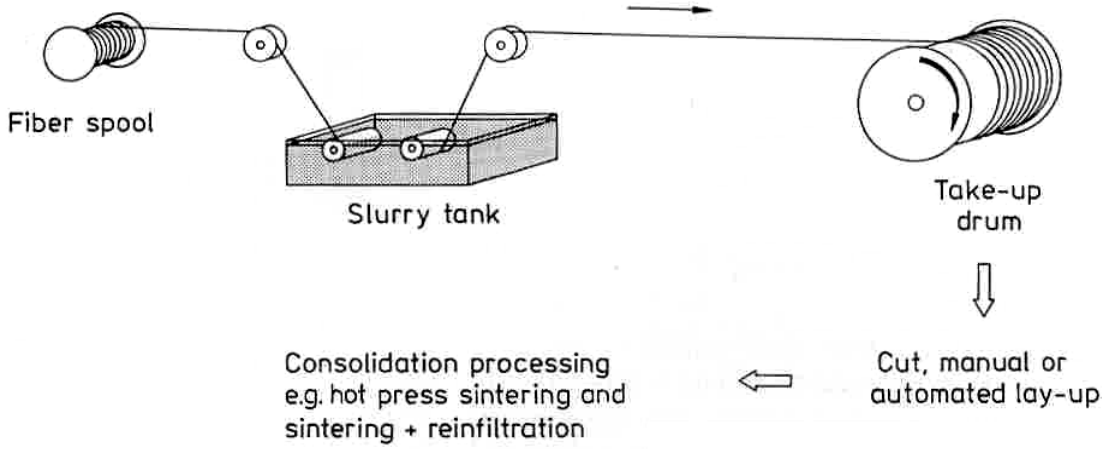

Figure 6. Schematic of Slurry Infiltration Process

Slurry for uncoated fibers contained 15 vol% alumina powder (AKP-53, Sumitomo Corp.) and 85 vol% alumina sol (alumina nitrate + deionized water + citric acid + ethylene glycol), while the slurry for the coated fibers was 10 vol% alumina powder and 90 vol% alumina sol. Monazite coating is thought to "soak up" more slurry . Fiber volume fractions were calculated by counting the number of wheel revolutions for a given tape width.

The tape sections were then cut from the spool and stacked into a metal mold while still wet. The composite was laid up in an 8-layer symmetric cross-ply orientation of $[(0^o/90^o)_2)]$s. Figure 7 shows a schematic representation of this cross-ply lay-up.

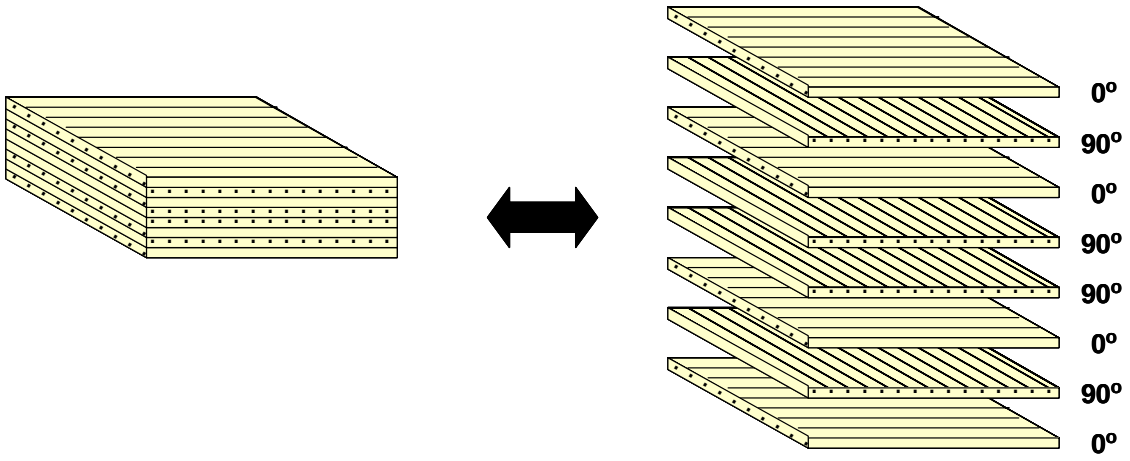

Figure 7. Schematic Representation of $(0^o/90^o/0^o/90^o)$s Ply Lay-up

The mold was then placed in a vacuum bag and a roughing pump was used to apply a vacuum. The bag was then placed on a Carver press containing heat platens and consolidated under ~1000 psig, with a maximum temperature of ~85°C. After several hours at this condition, the sample was removed and placed in a drying oven at ~100°C overnight. After drying, the sample was heat treated at 1200°C for 5 h in air. During the heating cycle, a one hour hold at low temperature was conducted to remove any residual organics in the matrix. Control samples, N610/Alumina, containing uncoated fibers were produced with the same procedure (21).

During the cooling stage of processing, thermal mismatches amount the composite constituents cause then to shrink at different rates. Since the coefficient of thermal expansion of the matrix ($8.8 \times 10^{-6}/^oC$) is larger than that of the fiber ($7.9 \times 10^{-6}/^oC$) it shrinks faster causing microcracking to occur throughout the matrix of the composite. This is a common problem when processing ceramic composites. Extensive surface microcracking can be seen in a top view of an as-received test specimen, shown in Figure

8, while interlaminar matrix cracks can be seen in a side view of an as-received specimen shown in Figure 9.

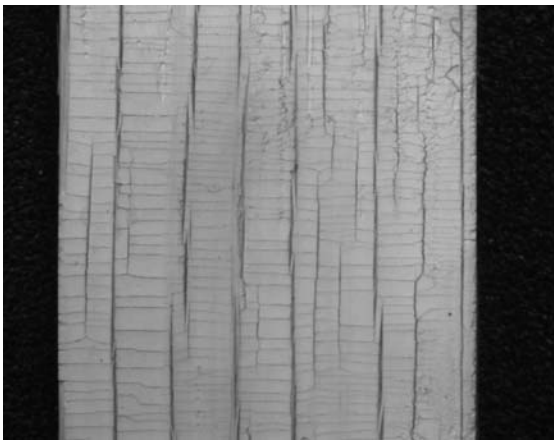

Figure 8. Surface Microcracking

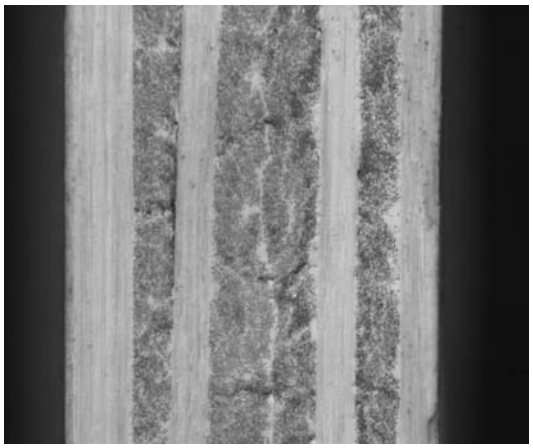

Figure 9. Interlaminar Microcracking

Test Specimen

Test specimens were cut from the composite panels by two methods throughout this investigation. Some specimens were cut using an abrasive water-jet machine at Kerf Wajerjet. These specimens were then cleaned using an ultrasonic bath, soaked in alcohol and finally dried in a oven to remove any residual liquid. Other specimens were cut using a diamond-grit cut/grinding approach at Bomas Machining, and were cleaned before they were returned.

A specimen length of 126 mm (~5 in) was chosen as slightly shorter than the 6 in panel length obtained during composite production, to eliminate the non-uniform edges of the material due to hand lay-up of the plies. A reduced gage section (dogbone) shape

was chosen for test specimens to promote gage section failures during testing. Figure 10 shows the exact specimen geometry. Circular insert shows fiber orientation and is not machined into the specimens.

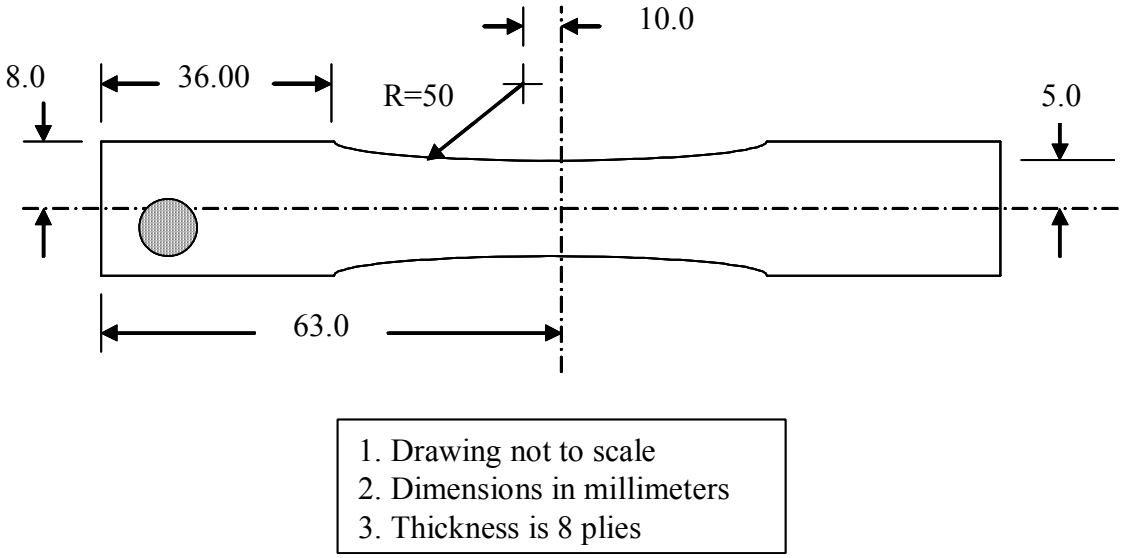

Figure 10. Test Specimen Geometry

Test specimens used in both tensile and creep-rupture tests we tabbed using a glass-fabric/epoxy material. Glass fabric/epoxy works well as a tabbing material because it is a more compliant material and reduces the stress concentration introduced by discontinuity at the tab end. It is also a very tough and fairly strong material which can absorb the surface damage caused by the hydraulic wedge grips (3). The purpose of tabbing is twofold; first to transfer the load from the hydraulic wedge grips to the test specimen without causing stress concentrations due to uneven gripping surfaces, and second to protect the surface of the composite from damage by the grips. Specimen areas to be

tabbed and tab surfaces were cleaned using M-Prep Neutralizer. The tabs were then coated with an M-Bond Catalyst to ensure secure bonding of the tab to the specimen. Five drops of M-Bond Adhesive in a “X” pattern were used to bond the tab to the specimen. Pressure was applied for 15 seconds to evenly distribute adhesive and create a strong bond. An example of a tabbed specimen can be seen in Figure 11.

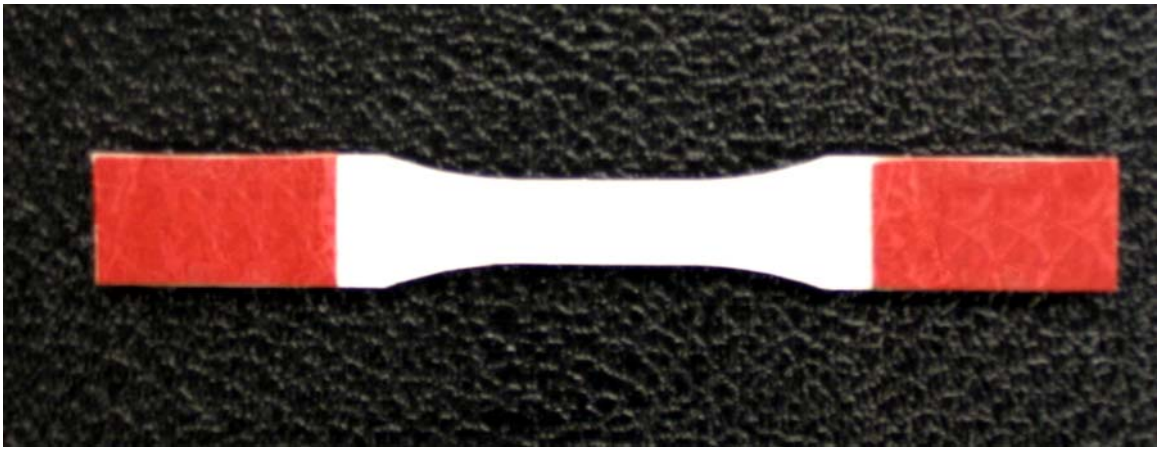

Figure 11. Tabbed Test Specimen

IV. Experimental Setup and Testing Program

This section describes the equipment used to characterize the Nextel 610/Monazite/Alumina composite, along with the procedures for testing and post-test analysis.

Test Equipment

Equipment used in testing falls into three main categories: Microstructural characterization equipment (discussed in *Post Failure Analysis* section), mechanical test apparatus, and high temperature equipment.

Mechanical Test Apparatus

Four main pieces of equipment used in characterizing the Nextel 610/Monazite/Alumina composite fall into this category. They included the servo hydraulic machine, the chilled water system, the extensometer, and the computer software.

The servo hydraulic machine utilized for all testing was a Material Test Systems (MTS) Corporation axial test system configured horizontally. Although this machine has a 25 kN (5500 lb) capacity, the highest load reached during testing was only 7.1 kN (1605 lbs). The machine utilized a pair of MTS 647.02A-01 Hydraulic Wedge Grips. The grips each contained a pair of interchangeable wedges with flat griping surfaces coated with a layer of surf alloy to prevent slipping of the test material. Each wedge contained an inlet and outlet to allow cooling water to pass through during testing and maintain a

suitable grip temperature. The grip pressure was controlled by an MTS 685.53 Hydraulic Grip Control attached to the test stand which is capable of pressures up to 20.7 MPa (3000 psi). Grip pressures varied from 3.5 to 8 MPa (500 - 1160 psi) during testing based on the maximum load required for each test, to prevent slipping. Grip pressure was also carefully chosen so that the specimen was not crushed when gripped.

Prior to testing, the grips were aligned using an MTS 709 Alignment System consisting of an MTS 609 Alignment fixture fitted with twelve strain gages and MTS 709 Alignment Software. The alignment specimen's strain levels were zeroed out, and then gripped under no load. The position and rotation of the right grip was then adjusted using the alignment fixture until the strain levels were again close to zero. This procedure eliminated any bending or twisting stresses on test specimen caused by improper alignment of the grips. The MTS Alignment Fixture is shown in Figure 12.

Figure 12. MTS 609 Alignment Fixture

An MTS model 661.20E-01 load cell, also with a 25 kN capacity, measured the load applied to the test specimen by the hydraulic piston. Figure 13 depicts the test stand with the servo hydraulic machine, the furnace, and the extensometer assembly.

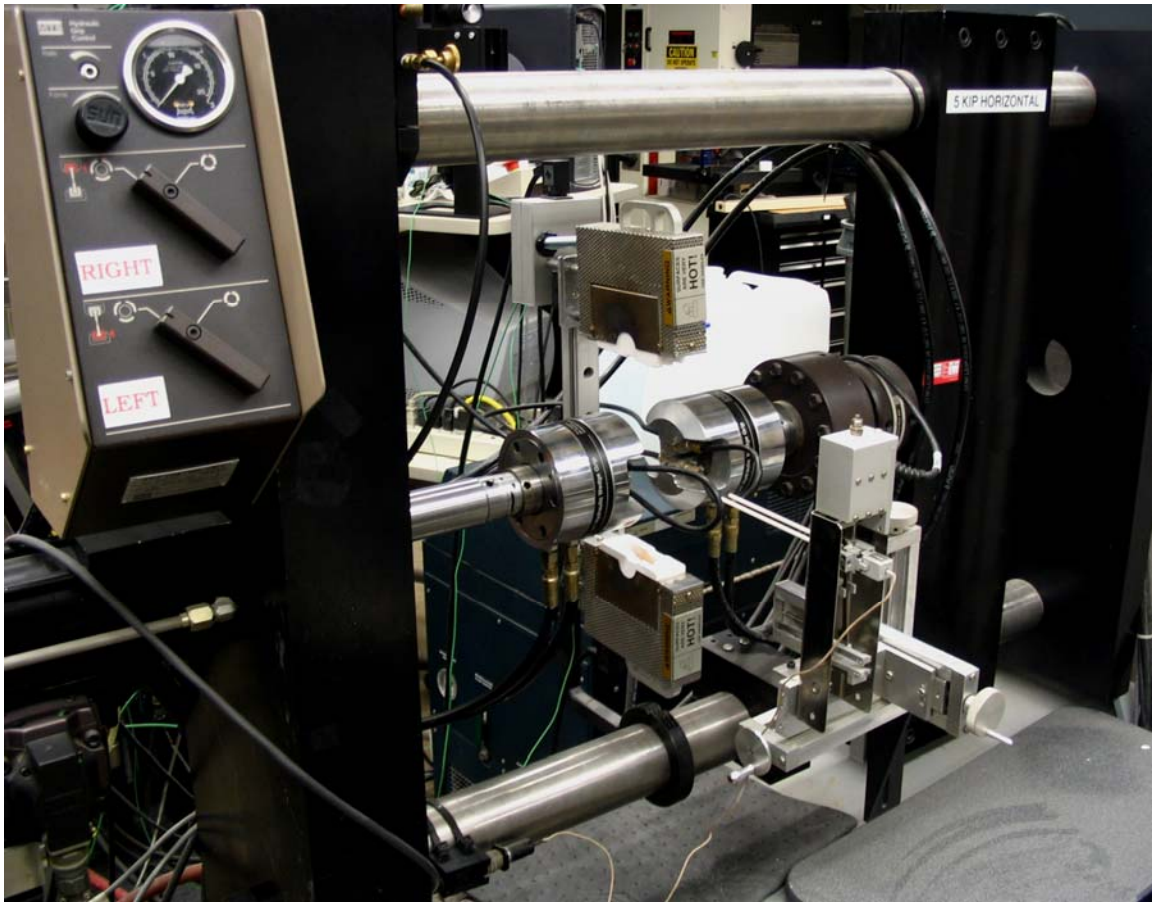

Figure 13. MTS Servo Hydraulic Machine

The machine supplying the cool water for grip cooling was a NESLAB model HX-75 chilled water system. This system became extremely important during elevate

temperature testing to keep the grips cool while area surrounding the furnace was very hot. The chiller was connected to the test stand by rubber hosing and distributed to the wedges via 6.35 mm ($^1/_4$ in) outer diameter black plastic tubing after passing through a water pressure regulator at the top of the stand. The HX-75 pumped distilled water at 9^{o}C. This system was used during all high temperature testing, including temperature calibration runs.

Strain was measured with an MTS high temperature uniaxial extensometer model number 632.53E-14. It included two 3.5 mm diameter alumina rods with a 12.7 mm (0.5 in) gage length and a cone-shaped tip for mounting on flat specimens. The extensometer can measure strains between +20 and -10% for a maximum specimen temperature of 1200^{o}C (2200^{o}F) and can provide up to 300 g of contact force through spring tension. A heat shield is also part of the assembly to protect the extensometer and conditioning electronics. Figure 14 shows the extensometer assembly. An MTS calibrator model 650.03 was used to calibrate the extensometer prior to testing.

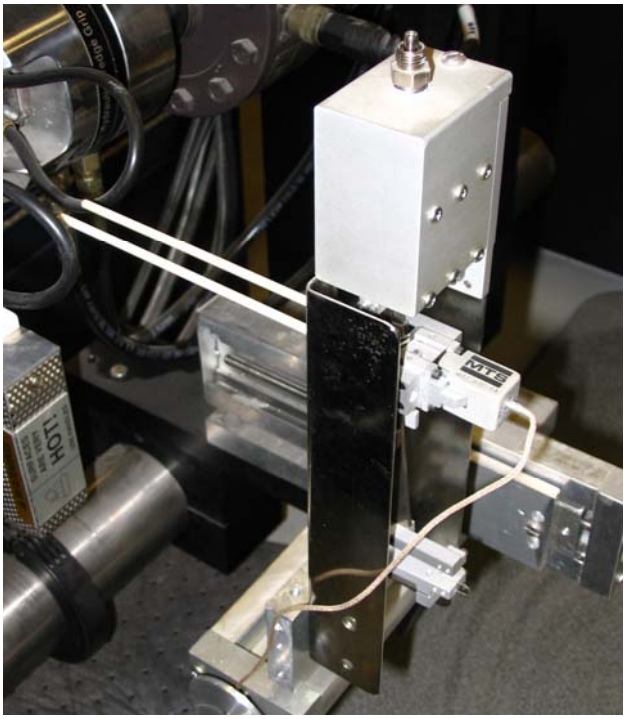

Figure 14. MTS High Temperature Uniaxial Extensometer Assembly

The computer software used to control the servo hydraulic machine and furnace was MTS TestStar IV. Its Multi Purpose Testware (MPT) feature was used to program each type of test and acquire data during testing. The software allowed for completely automated testing and data acquisition. Figure 15 shows an example of an MPT test program used during a creep test.

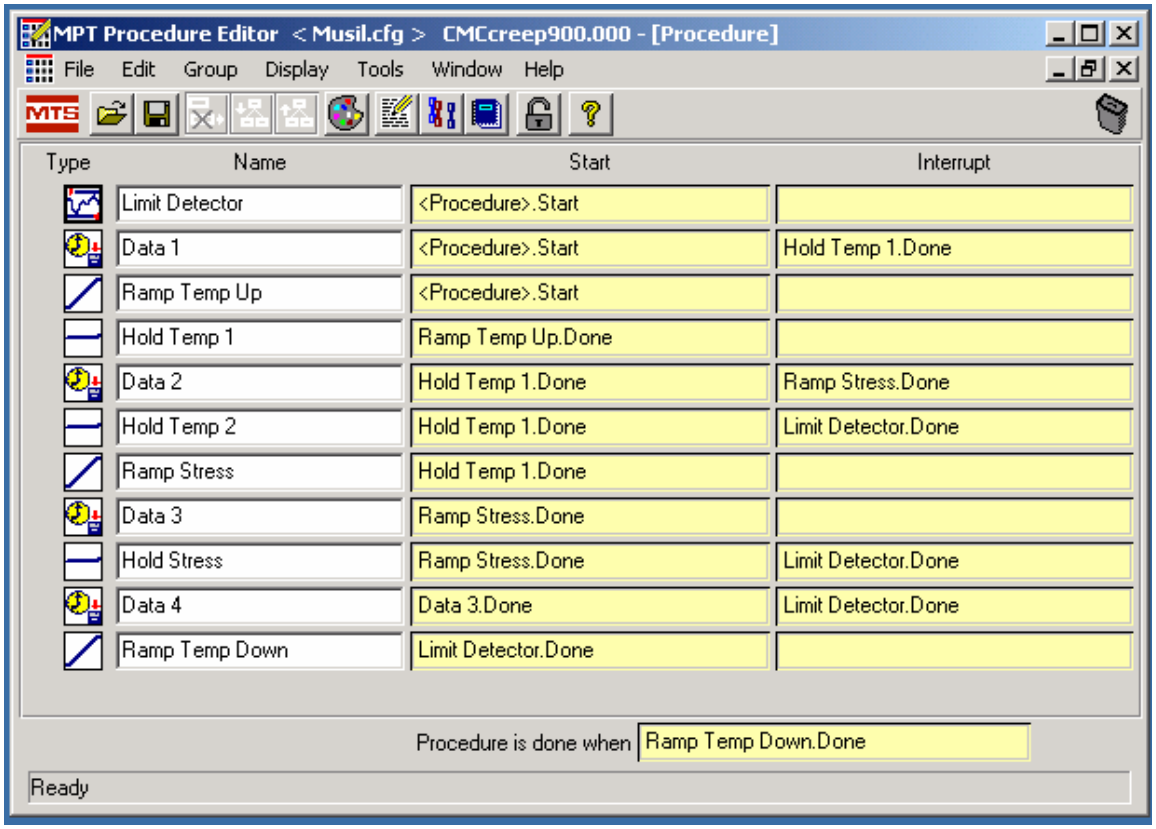

Figure 15. MPT Creep Test Procedure

High Temperature Equipment

Testing at elevated temperatures, which ranged between 900 and 1200°C, was accomplished by using a single zone Amteco Hot Rail Furnace System and a single zone MTS 653.01A High Temperature Furnace. The MTS furnace was only used for 1200°C tests and the Amteco furnace was used for the rest of the tests. Both furnaces were made up of two halves, each containing one silicon carbide heating element, mounted above and below the gripped specimen. Figure 16 shows the bottom portion of the Amteco furnace in place below the specimen.

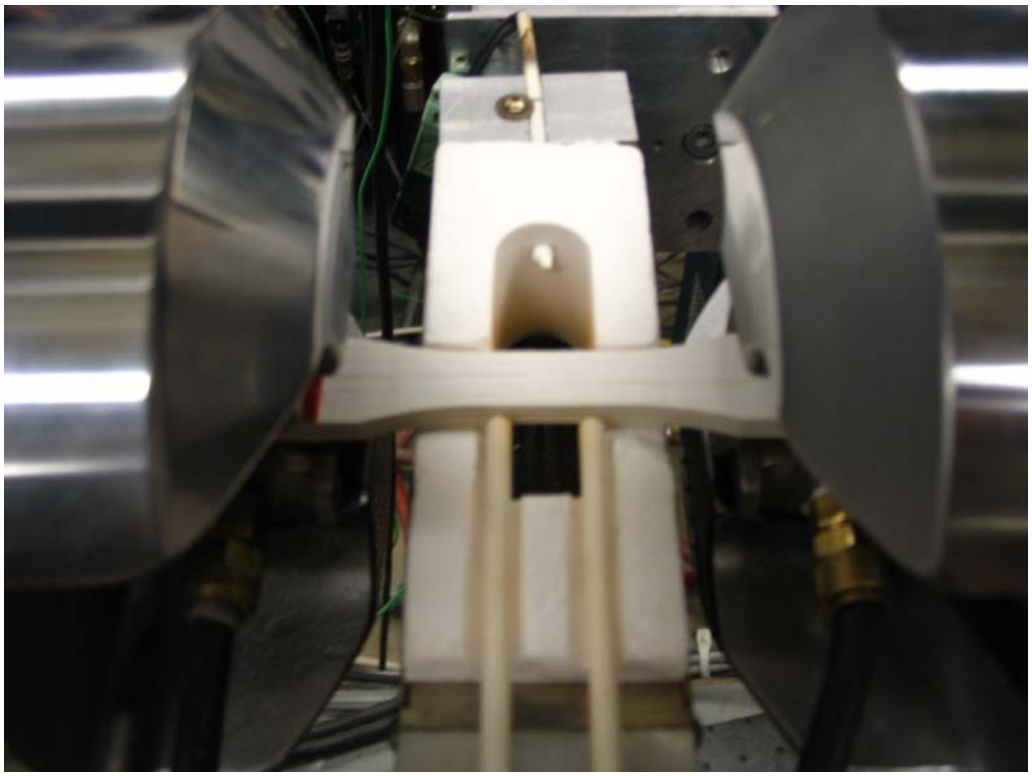

Figure 16. Furnace in Place below Specimen

The MTS furnace allowed for 19 mm of the specimen to be exposed to the elevated temperature, while the Amteco allowed 15 mm. The furnace chamber was made of a removable fibrous alumina insert, which was carved out to allow room for only the specimen and extensometer rods when the two halves are closed together. This allows for minimum heat loss during testing. The furnace was controlled by an MTS 409.83 Temperature Controller unit. An S-type thermocouple mounted in the top half of the furnace provided a temperature feedback loop to the controller unit. Power was supplied to both furnace halves equally by the unit until the temperature sensed by the thermocouple matched that of the desired temperature in the chamber.

In order to calibrate the appropriate chamber temperature for a desire specimen temperature, a test specimen was fitted with two Omega Engineering, Inc P10R-015 0.38 mm diameter S-type thermocouples. One thermocouple was mounted to the top of the specimen and the other to the bottom just off center to ensure continuity of the specimen temperature. S-type thermocouples were used for their ability to operate at high temperatures and accuracy at those temperatures. Figure 17 shows a schematic of the

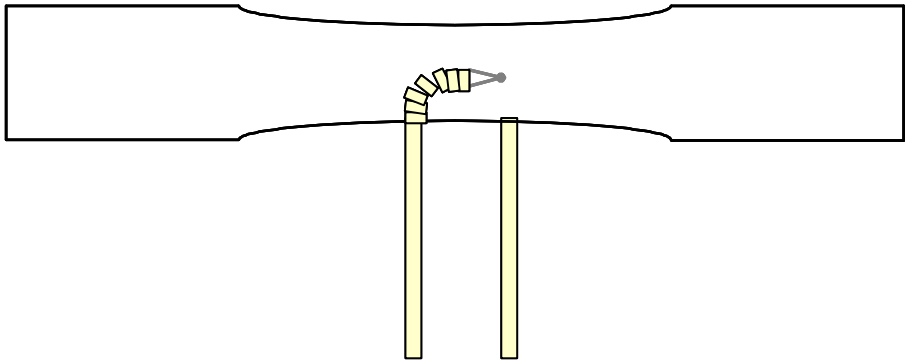

Figure 17. Schematic of Temperature Specimen

temperature specimen with the top thermocouple in view. The thermocouples were fed through a series of ceramic insulators to shield all but the tips and maintain separation between the wires. They were held in place with additional S-type thermocouple wire and bonded to the specimen using Zircar alumina cement. The temperature specimen was then baked just under 100^{o}C for one hour to harden and remove any water from the cement. The ends of the thermocouples were positioned such that they could pass through the extensometer holes in the furnace chamber.

Test Procedures

Test procedures for both monotonic tension tests and creep tests are described below. In addition, procedures for calibrating and maintaining furnace temperatures are presented. For all testing, including temperature calibrations, the first side of the specimen was mounted in the grips of the servo hydraulic machine under stroke control while the other was mounted under load control. Gripping under load control assures zero load on the specimen throughout the heating process despite thermal expansion of the material. The extensometer rods were then brought in contact with the specimen using spring tension and the strain value was zeroed out prior to testing.

Test Temperature

In order to insure proper specimen temperature during all high temperature testing, the MTS furnace needed to be calibrated for each test temperature. This was done using the aforementioned temperature specimen along with an Omega Engineering, Inc. OMNI-CAL-8A-110 portable, two-channel temperature sensor. The temperature specimen was mounted in the grips with minimal grip pressure (~1 MPa). Once gripped the two halves of the furnace were closed around the specimen allowing the thermocouples to pass through the extensometer holes. The thermocouples were then hooked up to each channel of the temperature sensor to monitor specimen temperature on both the bottom and top surfaces.

Using the MPT software, the furnace temperature was raised to the desired specimen temperature at a rate of 1^{o}C per second. When the furnace reached the programmed temperature, it was then adjusted manually until the readings from the two thermocouples

mounted to the specimen were as close to the desired temperature as possible. The furnace temperature was then allowed to stabilize and was further adjusted for an exact controller setting for each specimen temperature desired. Specimen temperature was found to reach equilibrium at approximately 15 minutes for all temperatures. At equilibrium the top and bottom thermocouples were within ± 2^{o}C of each desired temperature. It was found that to reach a desired specimen temperature, the temperature of the furnace did not need to be as high. Table 3 below depicts the desired test temperatures along with their respective furnace controller settings. The asterisk on the controller setting for 1200^{o}C indicates that it was found using the MTS furnace, while the rest were found using the Amteco furnace.

Table 3. Temperature Controller Settings

Specimen Temp (^{o}C)	**Controller Setting (^{o}C)**
1200	1259*
1100	904
1000	801
900	714

Monotonic Tension Tests

Monotonic tension tests to failure were performed on tabbed specimens of both the Nextel 610/Alumina and the Nextel 610/Monazite/Alumina. These tests were performed under stroke control with a constant loading rate of 0.05 mm/sec. This loading rate results

in failure in less than 60 seconds which minimizes time dependent behavior during elevated temperature tests (3). For high temperate tests, the specimen was heated at a rate of 1^{o}C/sec, and then allowed a 15 min dwell time prior to load-up for the temperature to stabilize. During testing, data acquisition included load, strain, stroke, stroke command, stroke abs error and temperature. Tension tests were run at every test temperature to obtain information on baseline ultimate tensile strength (UTS), modulus of elasticity (E) and coefficient of thermal expansion (α). Ultimate tensile strength in MPa was obtained by dividing the maximum load value, in N, before failure by the specimen's cross-sectional area in mm. Modulus values were calculated as the slope of the stress-strain curve over the 5-25 MPa stress range. Thermal strains were subtracted during data analysis to ensure that only mechanical strain was represented in the stress-strain curves.

Creep – Rupture Tests

The main focus of this investigation was on creep-rupture behavior. Creep-rupture test were carried out in the following manner. Load rate for these tests was based on the linear portion of the stress-strain curves. That portion of the curve was converted from stress vs. strain to load vs. time from which the slope was calculated to be 700 N/s (~160 lb/s). All creep tests were then run under load control with that load-up rate until the maximum load for the test was reached. Maximum load was determined as the desired creep stress level multiplied by the individual specimen cross sectional area. Figure 18 depicts the applied stress-vs-time profile for a given creep stress level and a 700 N/s load-up rate. Data acquisition during creep test consisted of stroke, strain, load, load command, load abs error and temperature. The run-out condition for creep tests was

defined as survival of 100 h which represents the amount of time at maximum temperature for typical applications of this material.

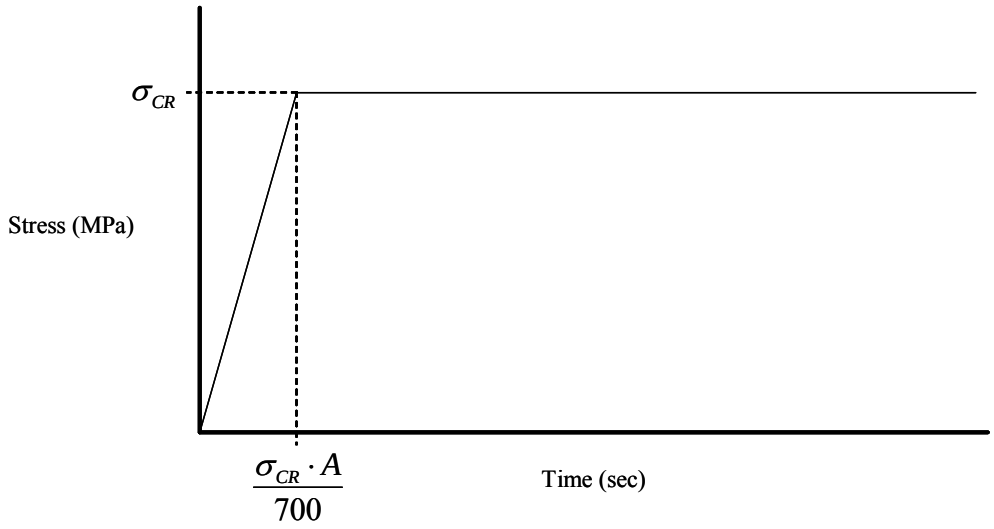

Figure 18. Stress vs. Time Behavior for Creep Tests

During creep-rupture testing, differences in elastic constants, creep rates, and stress-relaxation behavior between the fiber and the matrix can cause a time dependent redistribution of stress. When creep is present, the creep resistance mismatch causes a higher stress in the component with higher creep resistance and a decrease in stress for the less creep resistant component. Figure 19, from Holmes and Wu (19), illustrates the stress redistribution in a 0^o layer of a composite with a more creep resistant fiber, which is typically the case (19:194).

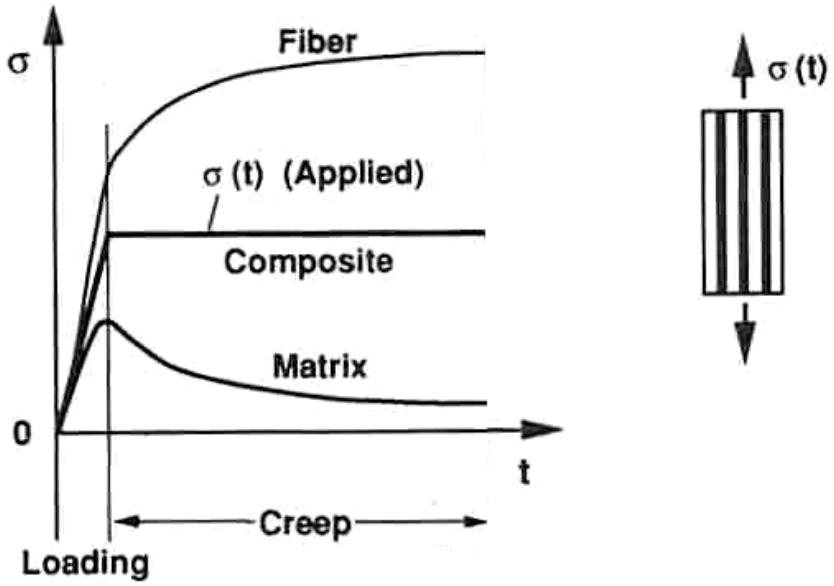

Figure 19. Stress Redistribution during Creep

This phenomenon places great emphasis on the creep resistance and tensile strength of the fiber. This also illustrates what happens when the matrix begins to crack and the load is transferred to the fibers for continued survival during creep.

Post Failure Analysis

The post failure analysis consisted of microstructural analysis using a Scanning Electron Microscope (SEM), as well as optical microscopy. Microstructural analysis was conducted on both the virgin (untested) material and the fracture surfaces of the test specimens for comparison.

SEM Analysis

SEM analysis was accomplished using a FEI FP 2011/11 Quanta 200 HV Scanning Electron Microscope shown in Figure 20. This form of microscope bombards the specimen with electrons and builds an image from those electrons that are reflected. Since ceramic materials are not good conductors and tend to build up a charge of electrons which distorts the SEM image, the specimens were coated with a conductive layer of gold prior to analysis. The gold coating was applied using an SPI MODULE 11430 Sputter Coater shown in Figure 21.

Figure 20. FEI Quanta 200 HV Scanning Electron Microscope

Figure 21. SPI MODULE Sputter Coater

The sputter coater uses positively charged argon gas ion plasma in a vacuum sealed chamber to strike a gold target knocking off the metal atoms which fall onto the specimen below. Prior to coating, the fractured specimen halves were cut down to a length that was usable in the SEM and mounted to an SEM test stand. Figure 22 below shows a coated specimen attached to a stand for use in the SEM.

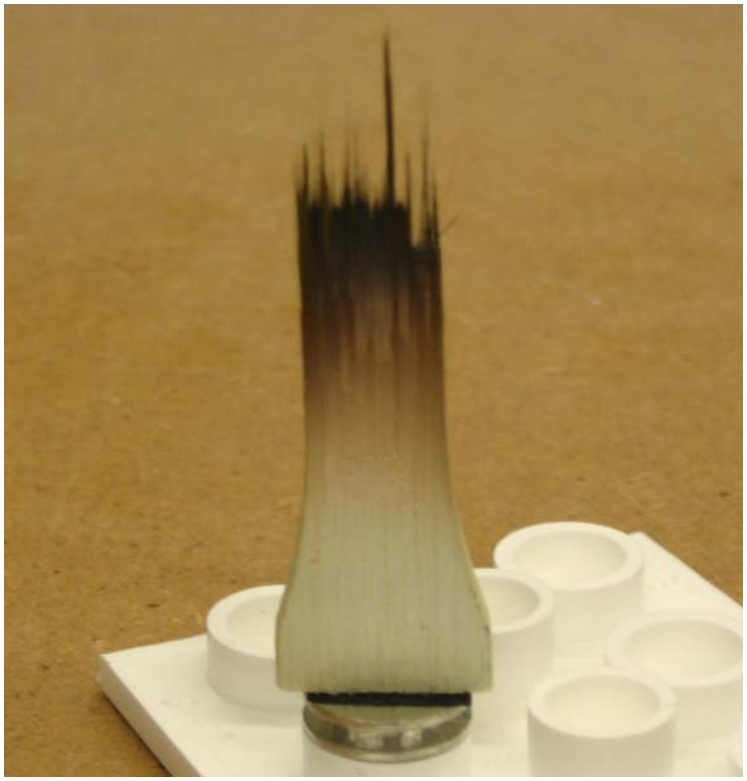

Figure 22. Sputter Coated Specimen for SEM Analysis

Optical Microscopy

Optical Microscopy was performed using a Zeiss Stemi SV II Optical Microscope incorporating a Zeiss AxioCam HRc digital camera. Virgin material was examined at lower magnification to demonstrate inherent flaws in the composite due to processing. Fracture surfaces of tested specimens were viewed at varying levels of magnification to depict amounts of fiber pullout during failure, as well as for lower magnification images of the material's post test microstructure.

V. Results and Discussion

This chapter will describe, in detail, the findings of this experimental investigation. It will begin with a brief discussion of thermal strain values calculated for all tests. Then there will be a discussion of the monotonic tension tests that were performed and the results of those tests. Finally, the creep test results will be presented and explained. Microstructural analysis will accompany each section

Thermal Strain

Thermal strain values were recorded in all elevated temperature tests and then used to calculate a coefficient of thermal expansion (CTE), α, value for each test. These results are summarized in Table 4. Coefficient of thermal expansion was evaluated by using the thermal strain equation shown below:

$$\varepsilon_{th} = \alpha \cdot \Delta T \qquad (1)$$

where ε_{th} is thermal strain and ΔT is the temperature change in ^{o}C. Temperature change values were based on a consistent initial specimen temperature of 23^{o}C for all tests.

Table 4. Linear Coefficient of Thermal Expansion Summary

Specimen Number	Material	Test Type	Test Temperature (^{o}C)	ε_{th} (mm/mm)	α ($10^{-6}/^{o}$C)
T1	N610/$LaPO_4$/Al_2O_3	tensile	900	0.006966	7.943
T2	N610/$LaPO_4$/Al_2O_3	tensile	1000	0.007506	7.683
T3	N610/$LaPO_4$/Al_2O_3	tensile	1100	0.008493	7.886
T4	N610/$LaPO_4$/Al_2O_3	tensile	1200	N/A	N/A
T6	N610/Al_2O_3	tensile	1100	0.007936	7.369
T7	N610/Al_2O_3	tensile	1200	0.009484	8.058
C1	N610/$LaPO_4$/Al_2O_3	creep	1200	0.009269	7.875
C2	N610/$LaPO_4$/Al_2O_3	creep	1100	0.008386	7.786
C3	N610/$LaPO_4$/Al_2O_3	creep	1100	0.008993	8.351
C4	N610/$LaPO_4$/Al_2O_3	creep	1100	0.008077	7.500
C5	N610/$LaPO_4$/Al_2O_3	creep	1100	0.009376	8.706
C6	N610/$LaPO_4$/Al_2O_3	creep	1000	0.007523	7.700
C7	N610/$LaPO_4$/Al_2O_3	creep	900	0.006902	7.870
C8	N610/$LaPO_4$/Al_2O_3	creep	900	0.006774	7.725
C9	N610/$LaPO_4$/Al_2O_3	creep	900	0.006721	7.663
C10	N610/$LaPO_4$/Al_2O_3	creep	900	0.006798	7.751
C11	N610/$LaPO_4$/Al_2O_3	creep	900	0.007355	8.387
C12	N610/Al_2O_3	creep	900	0.006593	7.518
C13	N610/Al_2O_3	creep	900	0.006805	7.759

The average values for the coefficient of thermal expansion are 7.916 x $10^{-6}/^{o}$C and 7.676 x $10^{-6}/^{o}$C, for N610/$LaPO_4$/Al_2O_3 and N610/Al_2O_3 respectively. According to 3M, the linear coefficient of thermal expansion for the Nextel 610 fiber alone is 7.9 x $10^{-6}/^{o}$C (29). Specimens with monazite coated fibers are allowed to fully expand via the weak

interface, whereas uncoated fibers become bonded to the matrix and thermal expansion is slightly inhibited. Specimen T4 was omitted from these calculations due to an extensometer slip.

Monotonic Behavior

Monotonic tensile tests to failure were performed to determine baseline ultimate tensile strength (UTS) and modulus of elasticity (E) values at each temperature. Monotonic tensile test results are summarized in Table 5.

Table 5. Summary of Monotonic Tensile Test Results

Specimen Number	**Material**	**Test Temperature (^{o}C)**	**UTS (MPa)**	**E (GPa)**	**ε_f (%)**	**Failure Location (inside/outside gage section)**
T1	N610/$LaPO_4$/Al_2O_3	900	180.09	83.06	0.3115	inside
T2	N610/$LaPO_4$/Al_2O_3	1000	162.48	78.05	0.2783	inside
T3	N610/$LaPO_4$/Al_2O_3	1100	157.39	76.37	0.3441	inside
T4	N610/$LaPO_4$/Al_2O_3	1200	129.54	49.80	1.4251	inside
T5	N610/Al_2O_3	RT	116.70	129.18	0.0943	inside
T6	N610/Al_2O_3	1100	104.83	115.84	0.1078	inside
T7	N610/Al_2O_3	1200	94.88	49.49	0.4613	inside

For temperature up to 1100^{o}C, failure strain (ε_f) exhibits no temperature dependence; while strength (UTS) and stiffness (E) decrease only slightly with increasing test temperature. At 1200^{o}C tensile behavior is highly nonlinear and large losses in strength and toughness, along with much larger failure strains, are observed. Strength decreases

9.7% between 900°C and 1000°C, 3.1% between 1000°C and 1100°C, and 17.7% between 1100°C and 1200°C. Stiffness drops 6.0% between 900°C and 1000°C, 2.2% between 1000°C and 1100°C, and 34.8% between 1100°C and 1200°C. Stress-strain curves obtained are presented below in Figure 23 for N610/Monazite/Alumina and Figure 25 for N610/Alumina.

It is known that tensile behavior of a cross-ply composite is 0° fiber-dominated. Hence tensile stiffness of the composite can be approximated based on the stiffness of the fibers using the following relationship:

$$E_c = \left(\frac{V_f}{2} \right) \cdot E_f \tag{2}$$

where E_c is the composite modulus, V_f is the fiber volume fraction, and E_f is the fiber modulus. Using an average fiber volume fraction of 48.7% and 41.8% for coated and uncoated fiber containing composites respectively, along with the RT modulus of 380 GPa for N610, composite moduli of 92.5 MPa and 79.4 MPa can be calculated respectively. Stiffness values for uncoated fiber-containing specimens found in this investigation indicate that the matrix and transverse fibers (90°) also contribute to the composite stiffness by increasing it to 129.18 MPa at RT. Experimental stiffness values for coated fiber-containing specimens indicate that the presence of the monazite fiber coating reduces composite stiffness.

Failure location refers to whether the test specimen failed inside or outside of the extensometer gage section. All tensile specimens in this investigation failed inside the gage section.

Stress – Strain (σ – ε) Curves

Stress-Strain curves obtained for N610/Monazite/Alumina at 900, 1000, and 1100°C are shown in Figure 23.

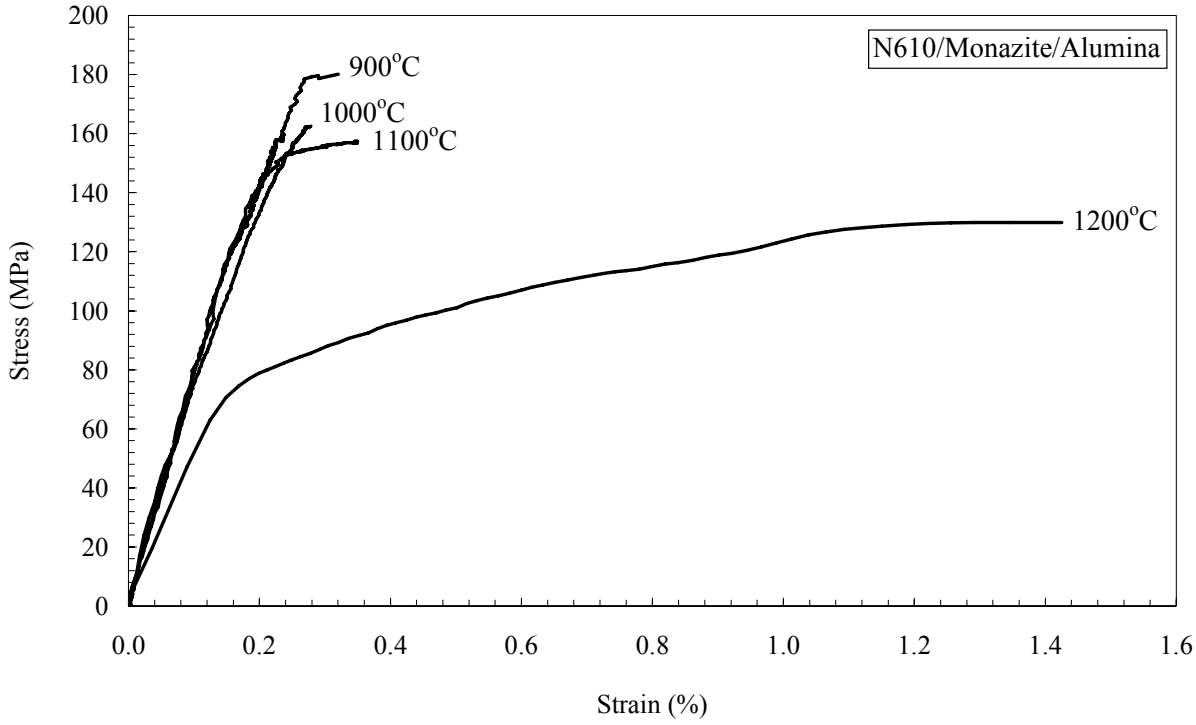

Figure 23. Stress-Strain Curves for N610/Monazite/Alumina

All curves display nearly linear elastic behavior initially. The stress-strain curves depart from linearity at $\varepsilon \approx 0.27\%$ for 900°C, $\varepsilon \approx 0.22\%$ for 1000°C, $\varepsilon \approx 0.15\%$ for

1100°C, and ε ≈ 0.12% for 1200°C. Seemingly inelastic (non-linear) behavior seen in the curves is actually progressive matrix cracking and crack deflection. This mechanism is thought by Chou et al to start as a transverse crack (crack in a 90° ply), progress into a matrix crack (crack in matrix of 0° ply), and finally cause fiber/matrix debonding and sliding (11). At the point of initial deviation from linearity, matrix cracks form in either matrix-rich regions or 90° plies at lower stress levels than they would in a 1-D composite. Matrix cracks originating in 90° plies proceed through the composite by a tunneling mechanism (16:45). Figure 24 from Evans et al (16), shows how matrix crack growth occurs in 2-D CMCs.

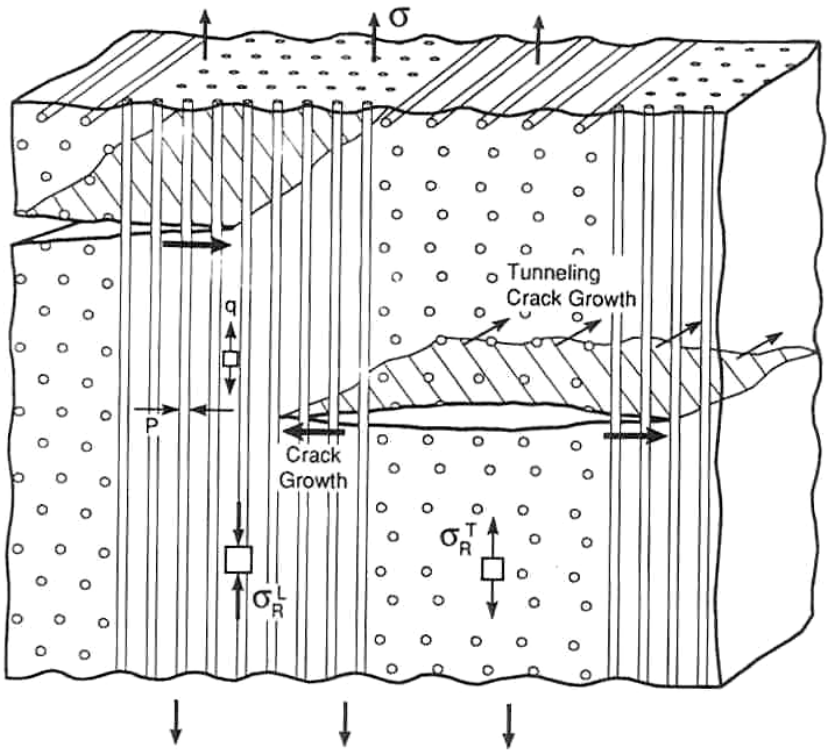

Figure 24. Crack Growth Mechanisms in 2-D CMCs

Inelastic deformation characteristics which enable the composite to retain strength in the presence of cracks are important to its attractiveness for use in high temperature applications. Crack deflection by the monazite coating causes the matrix and fibers to debond resulting in fiber pullout. During this process of continual matrix cracking, the load is transferred to the fibers prolonging composite failure. The amount of measured strain during this process was a function of the exact failure location in reference to the location of the extensometer rods on the specimen and how long the extensometer was able to maintain contact with the specimen. Fiber pullout is evidence that the monazite coating did create the desired week interface between the fiber and the matrix allowing cracks to be deflected and preserving strength at high temperatures.

Due to the number of test specimens, a RT tensile test for N610/Monazite/Alumina was not conducted. However, an approximate tensile strength can be calculated from the average room temperature tow strength of 1.13 GPa for N610 fiber heat treated at 1200^{o}C for 5 h presented by Keller et al (22:327). Normalizing the fiber tow strength for an average fiber volume fraction of 48.7% and a cross-ply orientation (~50% of fibers in loading direction), room temperature tensile strength would be approximately 275 MPa.

Stress-strain curves for N610/Alumina obtained at 23^{o}C (RT) and 1100^{o}C are shown in Figure 25, on the same strain scale as those for N610/Monazite/Alumina.

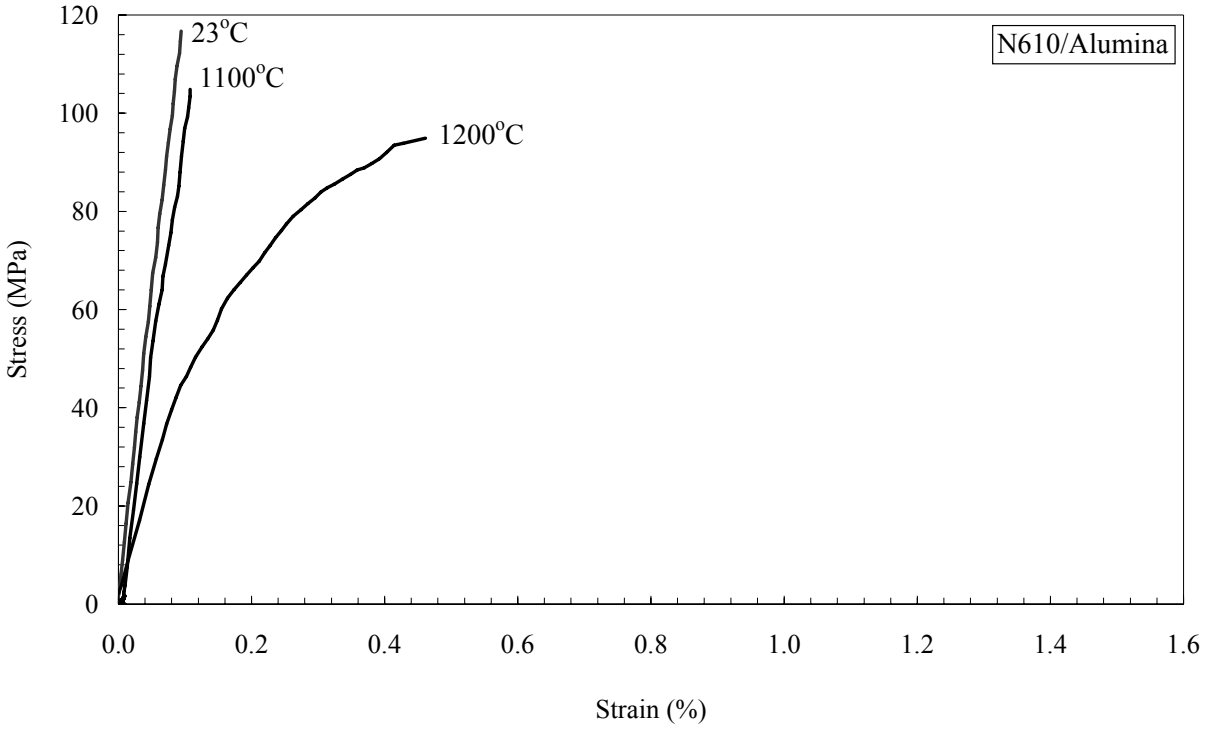

Figure 25. Stress-Strain Curves for N610/Alumina

Up to 1100°C, the curves are nearly linear-elastic until failure with no evidence of non-linearity associated with fiber pullout. Only a small decrease in tensile strength between 1100°C and RT indicates that the composite is able to retain its strength at high temperatures. However, lack of fiber-pullout demonstrated that without the monazite coating, the fiber and matrix become bonded together during processing. This results in the lower tensile strength as compared to the monazite containing specimens, as matrix cracks are not deflected and propagate directly into the fiber causing failure at lower stress levels. Due to the number of test specimens, a 900°C tensile test wasn't performed. Tensile strength for 900°C was estimated at 110 MPa between the RT and 1100°C values.

The effect of the monazite coating is more clearly seen in Figure 26, depicting stress-strain curves for both composites at 1100°C.

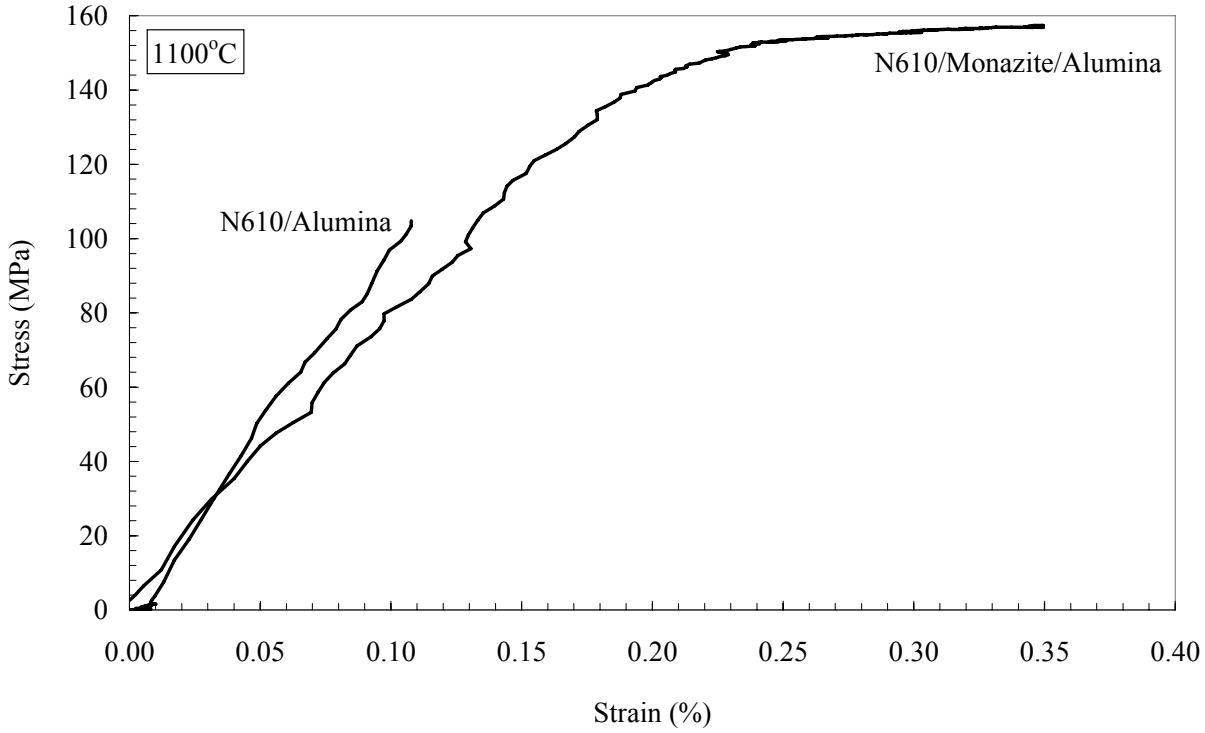

Figure 26. Stress-Strain Curves at 1100°C

It is seen that the stress level at which the stress-strain curve for N610/Monazite/Alumina specimen departs from linearity is approximately equal to the UTS for N610/Alumina specimen. In the coated fiber containing specimen, crack deflection by the monazite coating allows the fibers to absorb the load while the matrix is failing, thus perpetuating a much higher tensile strength. In the control specimen, the

matrix and fiber have become bonded and cracks are able to propagate straight through the fiber causing planar fracture surfaces with little to no fiber pullout.

This behavior is supported in Figure 27, from DiCarlo et al (14), which depicts the ideal stress-strain behavior of a continuous fiber reinforced ceramic composite.

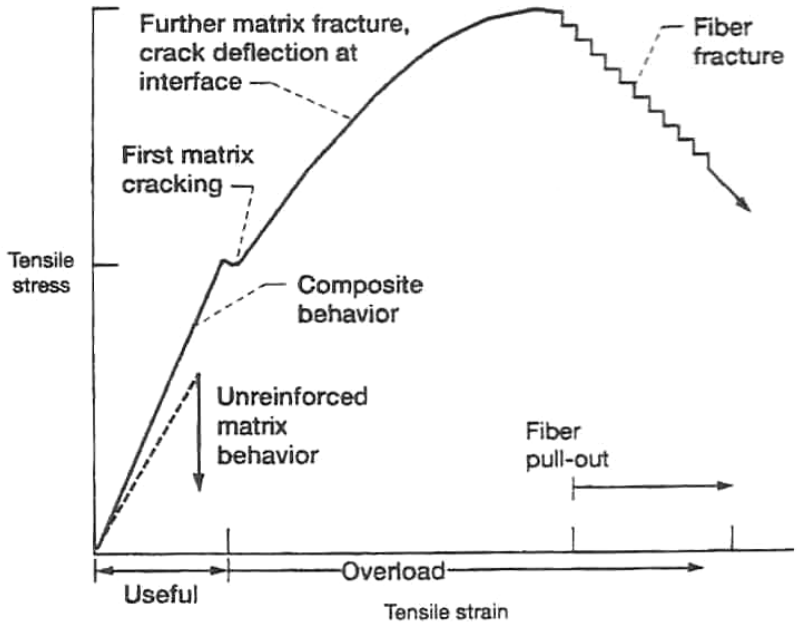

Figure 27. Ideal Stress-Strain Behavior of a CMC

The composite without the monazite coated fiber will fail at or just after the onset of matrix cracking due to the bonding of the fiber and matrix. Therefore the curve never departs the nearly linear portion shown above. However, the composite with the coated fibers which deflect matrix cracks, is able to sustain the load while the matrix continues to fracture, thus entering the nonlinear portion shown above. Upon the onset of fiber fracture, pullout begins. As mentioned previously, only small amounts of pullout are

visible in the above stress-strain curves, because the extensometer rods lose contact with the test specimen when fiber fracture occurs.

Microstructure

Fracture surfaces for N610/Alumina specimens obtained from monotonic tensile tests display nearly planar fractures at different locations in each ply. The location at which each ply failed corresponded to the location of the most fiber fractures within the ply. Tensile fracture surfaces are shown below for N610/Alumina at 23^{o}C in Figure 28, 1100^{o}C in Figure 29, and at 1200^{o}C in Figure 30. Specimen width is approximately 10 mm for all specimens.

Figure 28. Tensile Fracture Surface of N610/Alumina at 23^{o}C

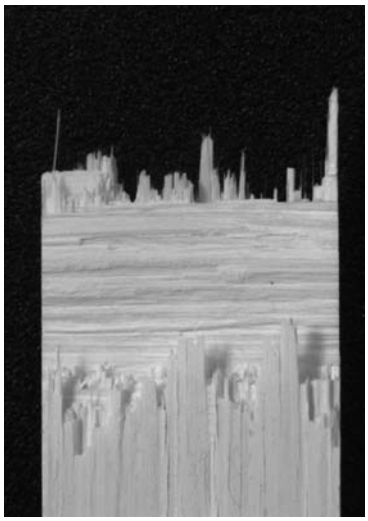

Figure 29. Tensile Fracture Surface of N610/Alumina at 1100^{o}C

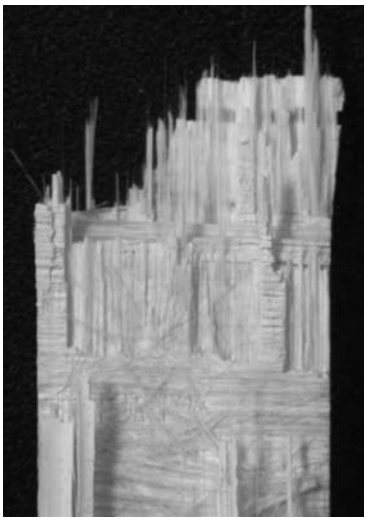

Figure 30. Tensile Fracture Surface of N610/Alumina at 1200^{o}C

Fracture surfaces at RT and 1100^{o}C show only small amounts of uniformly distributed fiber pullout. Where present, pullout is mainly groups of bonded fibers vice

single filaments. Fiber bonding most likely occurred during processing, as room temperature fracture surfaces exhibit the same behavior. The amount of pullout seems to increase slightly with increasing test temperature between RT and 1100°C. Lack of fiber pullout also corresponds to the tensile curves for specimens at RT and 1100°C, by nearly linear behavior until failure. Failure of the matrix and fibers occur simultaneously in these specimens. Failure appears to start from surface flaws on both the top and bottom faces of the specimen, propagating inward until delamination occurs between the two 90° layers at the center. At 1200°C, the matrix is significantly weakened and matrix cracking begins at approximately 45 MPa. Since the test temperature is equal to that of the heat treatment temperature, fiber/matrix bonds created during processing are released. This allows fibers to debond from the matrix and regions of random fiber pullout are seen in Figure 30. Again failure appears to have started from two surface locations, propagating inward with delamination occurring between the first 90° layer and the second 0° layer. Delamination during fracture is more easily seen in side views of the fractures surfaces, depicted below at 23°C in Figure 31, 1100°C in Figure 32, and at 1200°C in Figure 33. Thickness is approximately 3 mm for RT and 1100°C specimens, and approximately 3.5 mm for the 1200°C specimen.

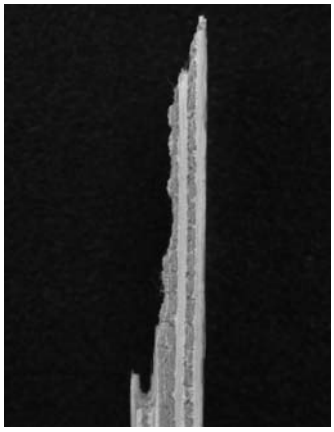

Figure 31. Tensile Fracture Surface of N610/Alumina at 23°C (Side)

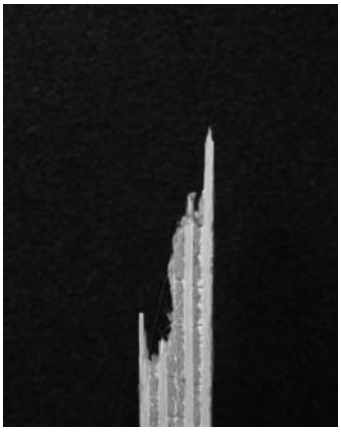

Figure 32. Tensile Fracture Surface of N610/Alumina at 1100°C (Side)

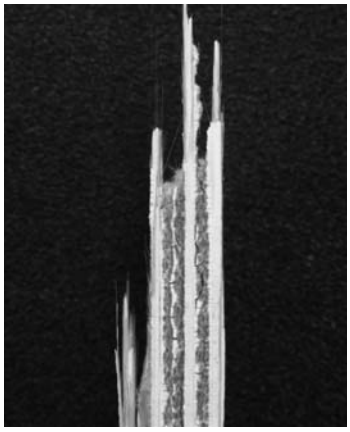

Figure 33. Tensile Fracture Surface of N610/Alumina at 1200°C (Side)

The SEM image in Figure 34, of the specimen tested at 1100°C, shows a continuation of the delamination through the center of the composite. Figure 35 shows the delamination at higher magnification down the surface of fracture.

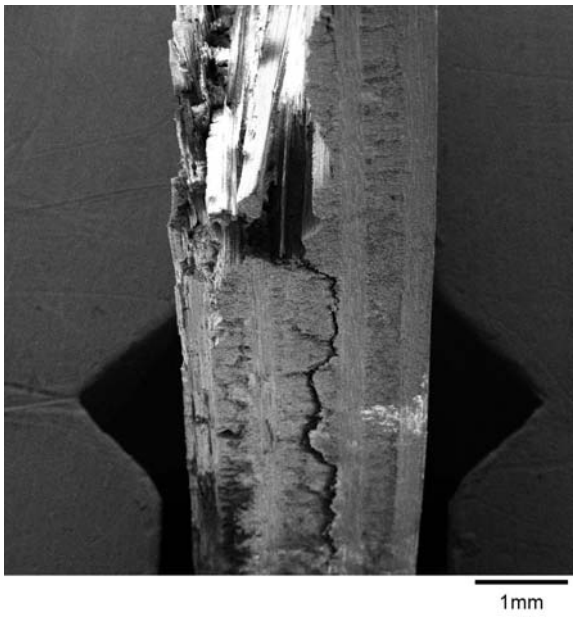

Figure 34. SEM Image Showing Delamination at 20x Magnification

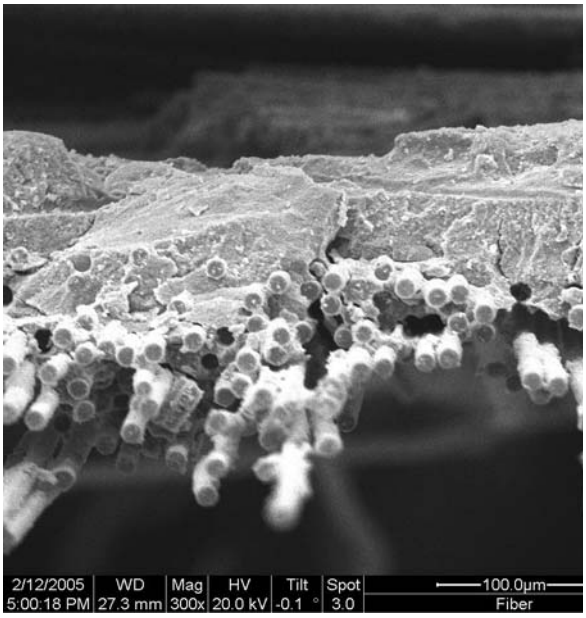

Figure 35. SEM Image Showing Delamination at 300x Magnification

Fracture surfaces for N610/Monazite/Alumina specimens obtained from monotonic tensile tests also appear very similar to each other. In contrast to the N610/Alumina composite, fracture surfaces show extensive amounts of uniformly distributed fiber pullout. Pullout is also very brush-like and is almost entirely single fibers as opposed to groups of bonded fibers. Fracture surfaces for can be seen for the test at 900^{o}C in Figure 36, 1000^{o}C in Figure 37, 1100^{o}C in Figure 38, and at 1200^{o}C in Figure 39.

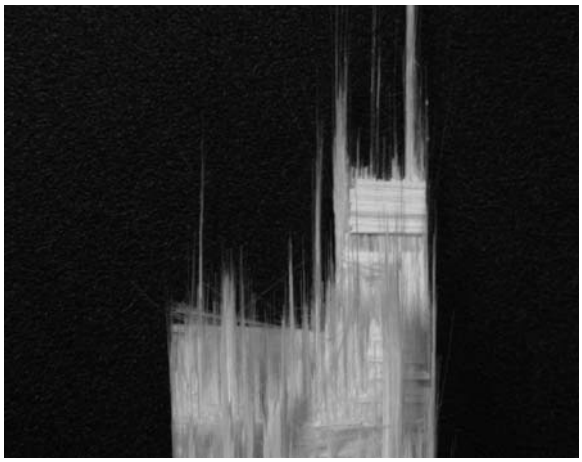

Figure 36. Tensile Fracture Surface of N610/Monazite/Alumina at 900°C

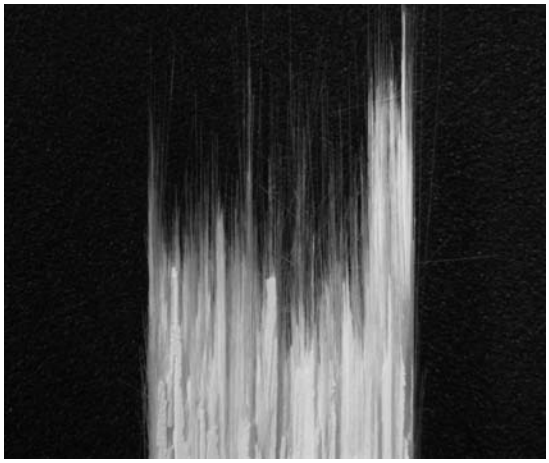

Figure 37. Tensile Fracture Surface of N610/Monazite/Alumina at 1000°C

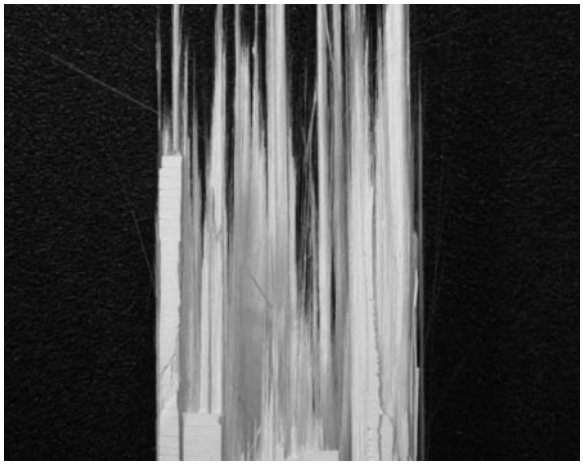

Figure 38. Tensile Fracture Surface of N610/Monazite/Alumina at 1100°C

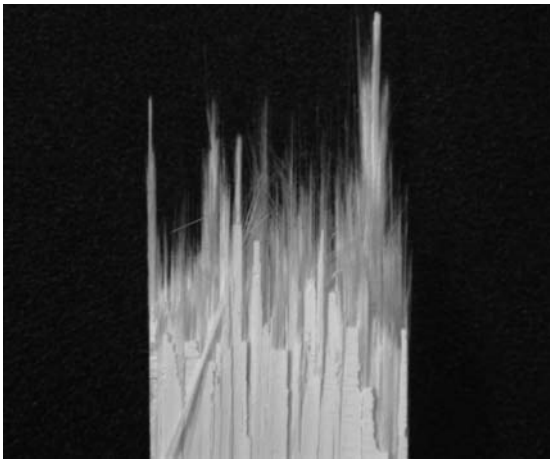

Figure 39. Tensile Fracture Surface of N610/Monazite/Alumina at 1200°C

Addition of the monazite fiber coating clearly provided the weak interface between the fiber and matrix that was desired, allowing the fibers to debond readily. Tensile strength was increased significantly, as was strain to failure. Pullout length varies significantly across fracture surfaces. At the time of fracture, the fibers were supporting the entire load and finally failed at their weakest location.

Side views of the tensile fracture surfaces indicate uniform pullout in each of the 0^o layers. They can be seen for tensile tests performed at 900^oC in Figure 40, 1000^oC in Figure 41, 1100^oC in Figure 42, and at 1200^oC in Figure 43.

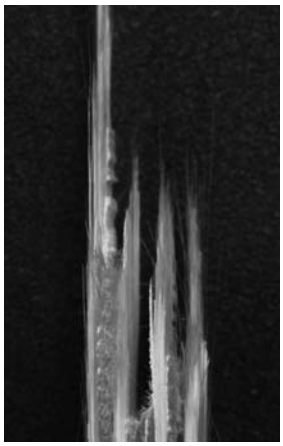

Figure 40. Tensile Fracture Surface of N610/Mon/Alumina at 900^oC (Side)

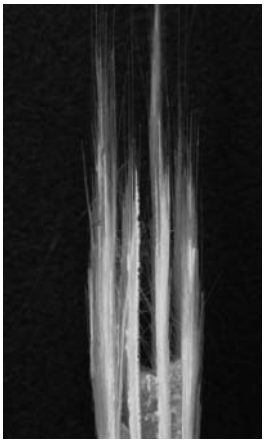

Figure 41. Tensile Fracture Surface of N610/Mon/Alumina at 1000^oC (Side)

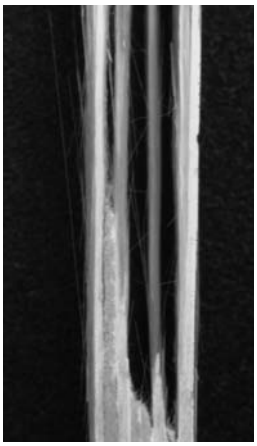

Figure 42. Tensile Fracture Surface of N610/Mon/Alumina at 1100^oC (Side)

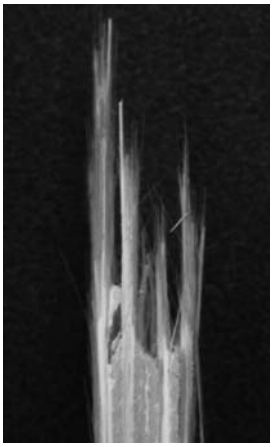

Figure 43. Tensile Fracture Surface of N610/Mon/Alumina at 1200^oC (Side)

Failure of the 90^o plies are basically planar and occurred at or near the same level in the composite. Matrix cracks could have propagated through each layer deflected around the fibers by the monazite coating and, in some cases, traveled along a debonded fiber socket causing failure in the next transverse ply at a slightly different level. Specimens that show 90^o layer failures at very different levels indicate multiple flaws could have caused the separation in failure planes.

On a microscopic scale, the extensive pullout of the N610/Monazite/Alumina composite can be seen to clearly contrast the planar fracture surfaces of the N610/Alumina composite. Figure 44 shows an SEM image of the fracture surface for the N610/Alumina, while Figure 45 shows the fracture surface for the N610/Monazite/Alumina specimen. Both specimens were tested at 1100^{o}C.

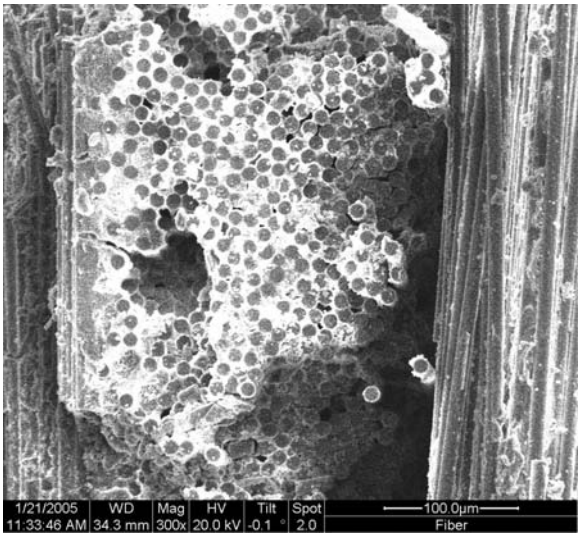

Figure 44. Tensile Fracture Surface of N610/Alumina at 1100^{o}C at 300x Mag.

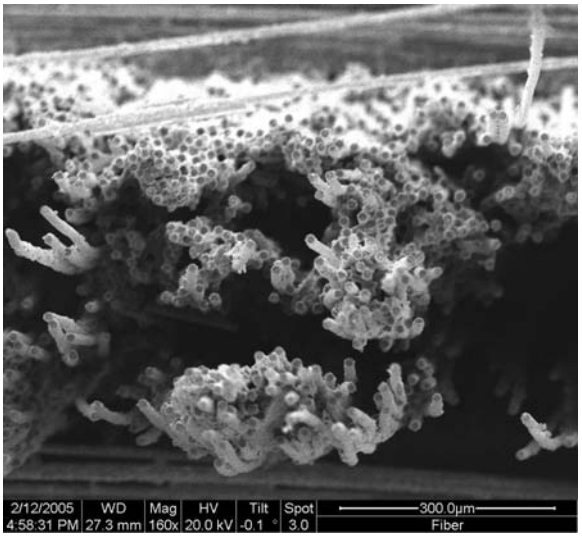

Figure 45. Tensile Fracture Surface of N610/Mon/Alumina at 1100^{o}C at 160x Mag.

Deep holes indicate location of pullout from the opposite half of the specimen. The specimen with monazite coated fibers shows large differences in fiber pullout lengths, while the specimen with the uncoated fibers fracture at approximately the same length with some groups of fibers pulled out slightly.

Further magnification (500x) of the N610/Alumina specimen tested at 1100°C, depicts a group of fibers bonded together. This fiber bridging, shown in Figure 46, inhibits the infiltration of matrix material during processing and leads to embrittlement, as seen from the corresponding linear stress-strain curve. Particles of matrix and coating that are still bonded to the fiber after pullout can also be seen in the image.

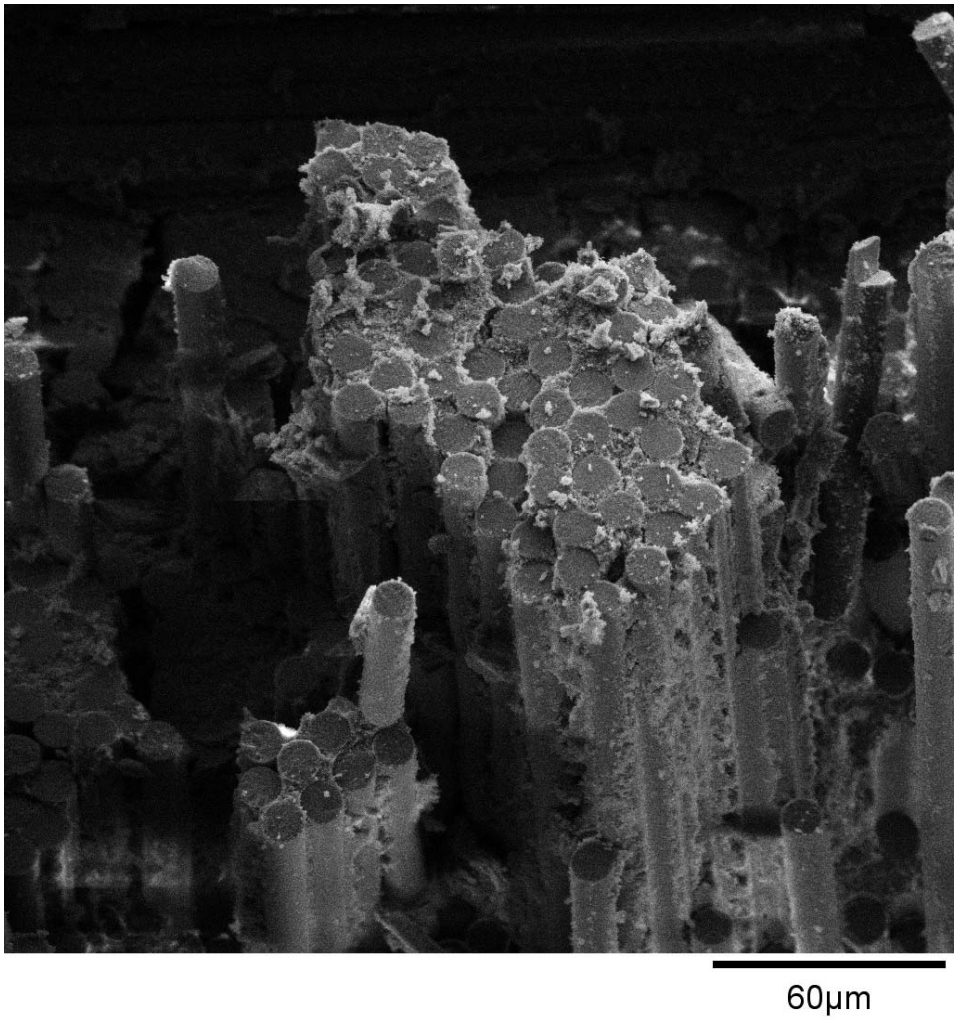

Figure 46. Tensile Fracture Surface of N610/Alumina at 1100°C at 500x Mag.

Still further magnification of N610/Monazite/Alumina fracture surfaces, show fiber pullout holes, which can be seen in Figure 47 and Figure 48.

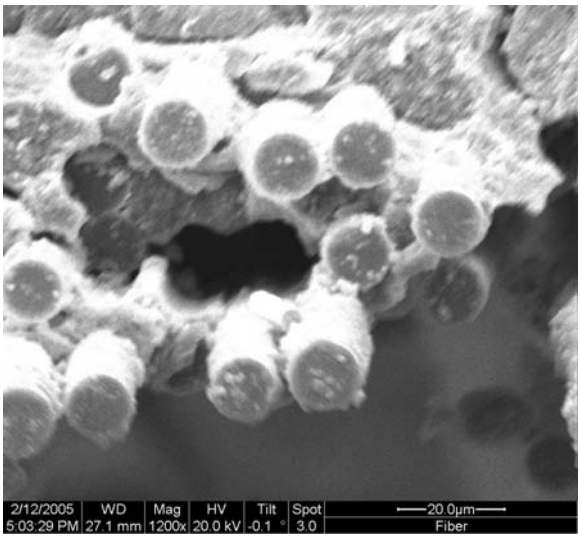

Figure 47. SEM Image shows Fiber Pullout Holes in N610/Mon/Al at 1200x Mag.

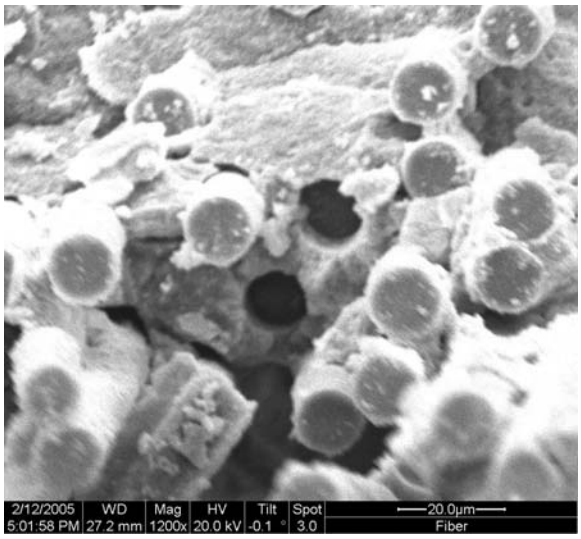

Figure 48. SEM Image shows Fiber Pullout Holes in N610/Mon/Al at 1200x Mag. (2)

Creep Behavior

Creep-Rupture (Stress-Rupture) tests were performed at temperatures of 1200, 1100, 1000 and 900°C. Creep-rupture test results are summarized in Table 6.

Table 6. Summary of Creep-Rupture Test Results

Specimen Number	Test Temperature (°C)	Creep Stress Level		Creep Strain (%)	Time to Rupture (s)	Failure Location (inside/outside gage section)
		(MPa)	(% UTS)			
C1	1200	104	80.00	3.110	56.5	inside
C2	1100	40	25.42	7.662	50,432	inside
C3	1100	80	50.83	3.365	1,452	inside
C4	1100	100	63.54	1.585	360	inside
C5	1100	120	76.25	0.703	75	inside
C6	1000	80	49.24	0.049	63,060	inside
C7	900	80	44.42	0.040	522,365*	inside
C8	900	120	66.63	0.044	432,175*	inside
C9	900	130	72.19	0.047	40,655	inside
C10	900	140	77.74	0.035	54,075	inside
C11	900	150	83.29	0.026	805	inside
C12	900	73	66.36	0.060	350,055	inside
C13	900	80	72.73	0.033	19,995	inside

* Runout (defined as surviving 100 h in creep)

As previously presented in Table 4, specimens C1-C11 are N610/Monazite/Alumina composites, while C12 and C13 are N610/Alumina composites.

Initial creep-rupture test performed at 1200°C indicated a very poor creep life of only 56.5 seconds. Test temperature was then lowered to 1100°C and a full family of creep-rupture test was performed at varying creep stress levels. Creep performance at 1100°C was determined to still be undesirable for any intended application. Test temperature was again lowered to 1000°C and a scoping test was performed at a creep stress level of 80 MPa to determine if creep behavior would be acceptable. While significantly longer creep life (63,060 s) was obtained versus the same creep stress level at 1100°C (1,452 s), it was still not at an acceptable level for stress level of only ~50% UTS. Therefore, test temperature was lowered again to 900°C. A full range of creep stress levels were investigated at this temperature and creep life was found to be acceptable with runouts occurring at creep stress levels of 80 and 120 MPa.

Creep of Nextel 610 Fiber

Tests performed by Wilson and Visser indicate that the N610 fiber is able to retain 70% of its room temperature strength at test temperatures up to 1000°C (34), thus making 1000°C the fiber's maximum use temperature. This temperature limit is observed in the composite also, as creep life at temperatures above 1000^{o}C is extremely poor. These results will be presented in the sections that follow.

Effect of Creep Stress Level

Only one stress level was tested at 1200^{o}C due to the extremely short creep life, even for 80% UTS. The creep-rupture curve can be seen in Figure 49.

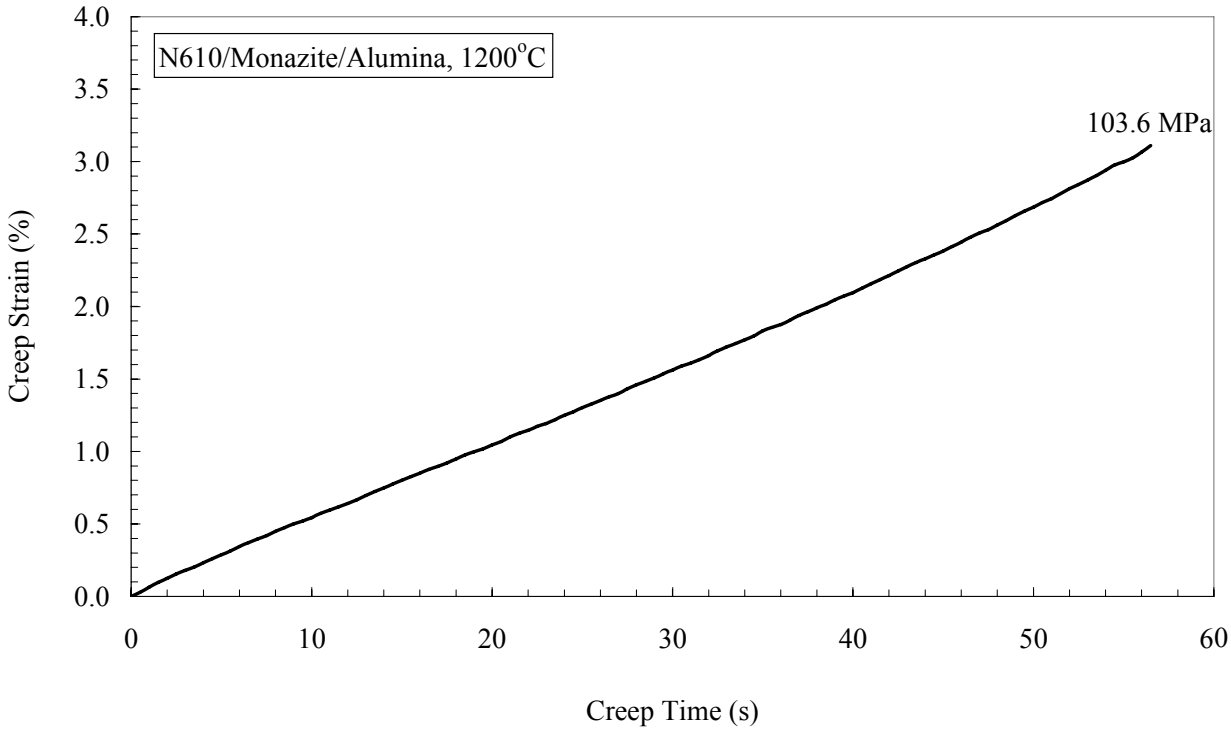

Figure 49. Creep of N610/Monazite/Alumina at 1200°C

Though the test lasted less than a minute, small regions of both primary and tertiary creep can be seen. The curve transitions from primary creep to secondary creep after only 2 s and remains nearly linear until about 2 s before failure when the creep rate begins to accelerate and a transition to tertiary creep is observed. A large amount of strain accumulation was observed, corresponding to a large amount of measured fiber pullout.

Creep-rupture curves at 1100°C and stress levels of 40, 80, 100, and 120 MPa are shown in Figure 50. The time scale of the plot has been truncated to more clearly view the curves for stress levels above 40 MPa. The arrow at the end of the visible portion of the 40 MPa curve indicates that the curve continues past 2000 s.

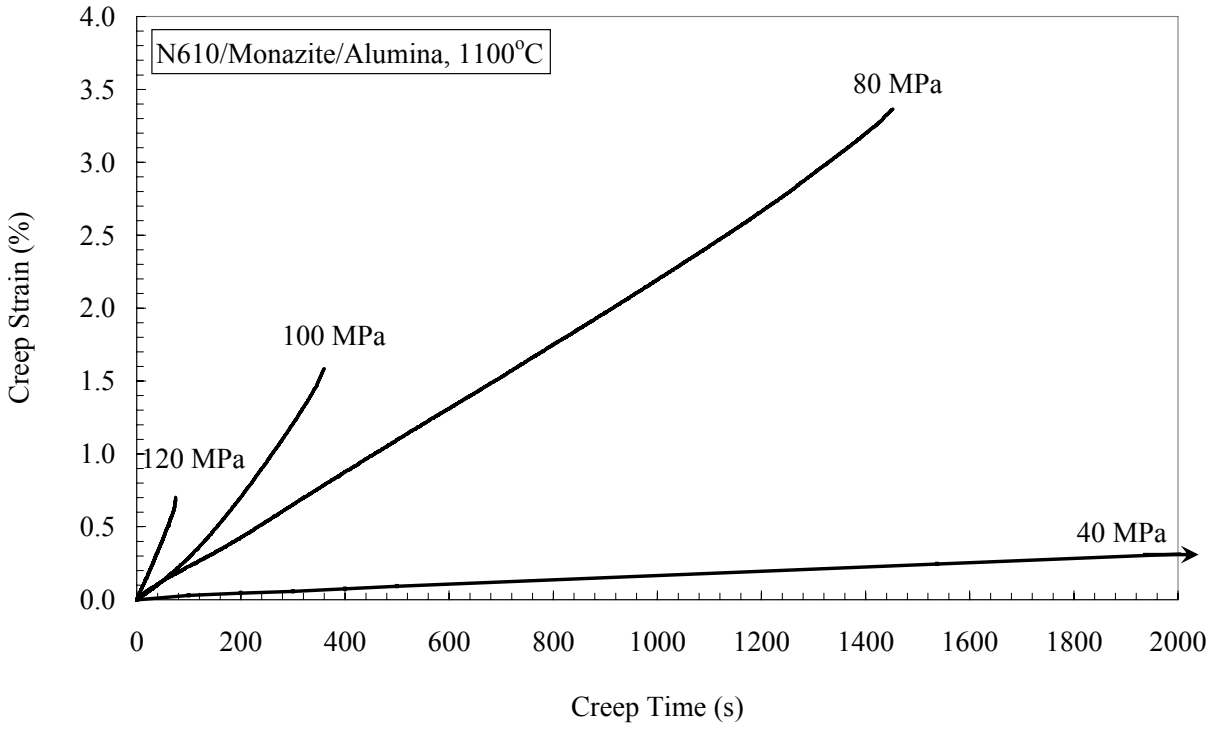

Figure 50. Creep of N610/Monazite/Alumina at 1100°C

Curves at all creep stress levels contain small regions of both primary and tertiary creep. Larger stress levels demonstrated larger creep rates and smaller failure strains. Although not visible in the figure, the 40 MPa test failed at 50,432 s and 7.66% strain. Strain accumulation at this stress level indicates premature failures at higher stress levels which have higher creep rates. If "allowed" to continue at those rates, failure strains would be greater for larger stress levels. This is seen at 75 s, the rupture time for the 120 MPa test, where the 40 MPa stress level had only accumulated ~0.02% strain, while the

80, 100, and 120 MPa tests have accumulated 0.18% strain, 0.21% strain, and 0.70% strain respectively.

The creep-rupture curve obtained at 1000°C with a creep stress of 80 MPa can be seen in Figure 51.

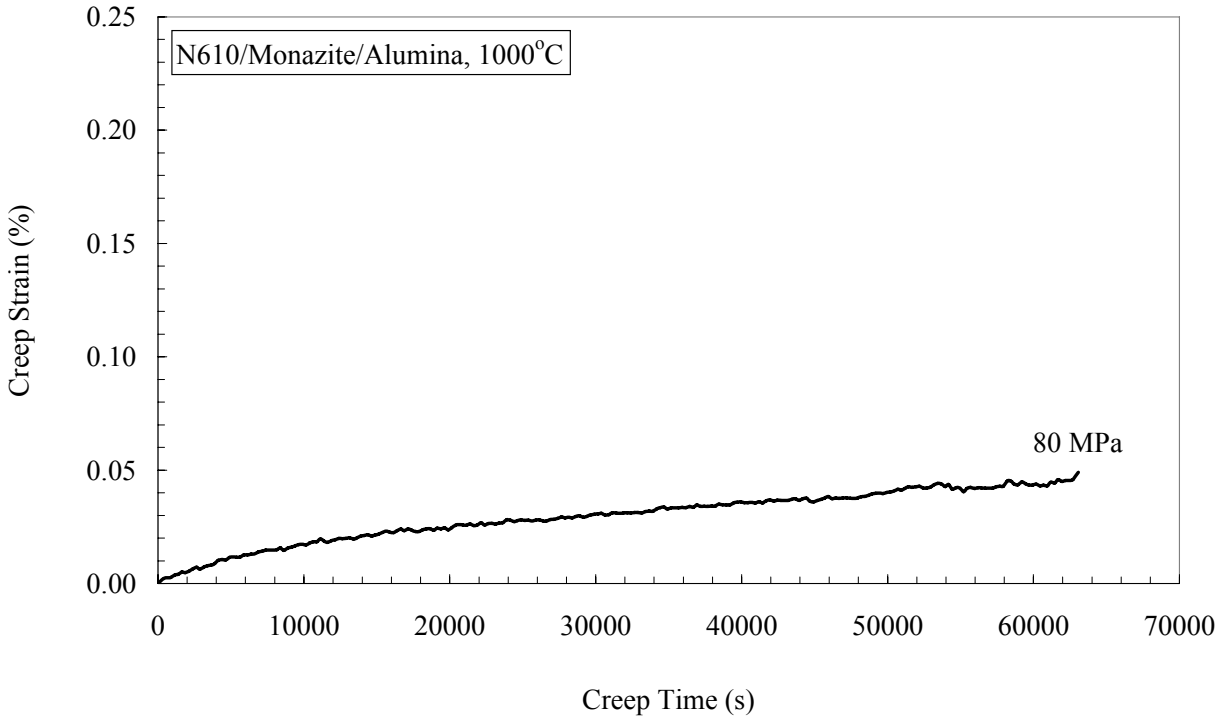

Figure 51. Creep of N610/Monazite/Alumina at 1000°C

Creep life is significantly improved at this temperature with a 4,343% increase over the observed creep life at 1100°C for the same stress level. Again the curve shows a region of primary creep with a transition to secondary creep occurring at approximately 10,000 s. The curve then remains nearly linear until just before failure when a small region of tertiary creep is observed. In addition, much less creep strain was accumulated

compared to what was seen at 1100°C. Although the increase in creep life is significant from that of 1100°C, for a stress level corresponding to less than 50% UTS, it is still not sufficient for extended use at this temperature.

Creep-rupture curves for 900°C are shown in Figure 52. Again, at the creep stress of 80 MPa a runout was achieved, and the test was interrupted after 164 h.

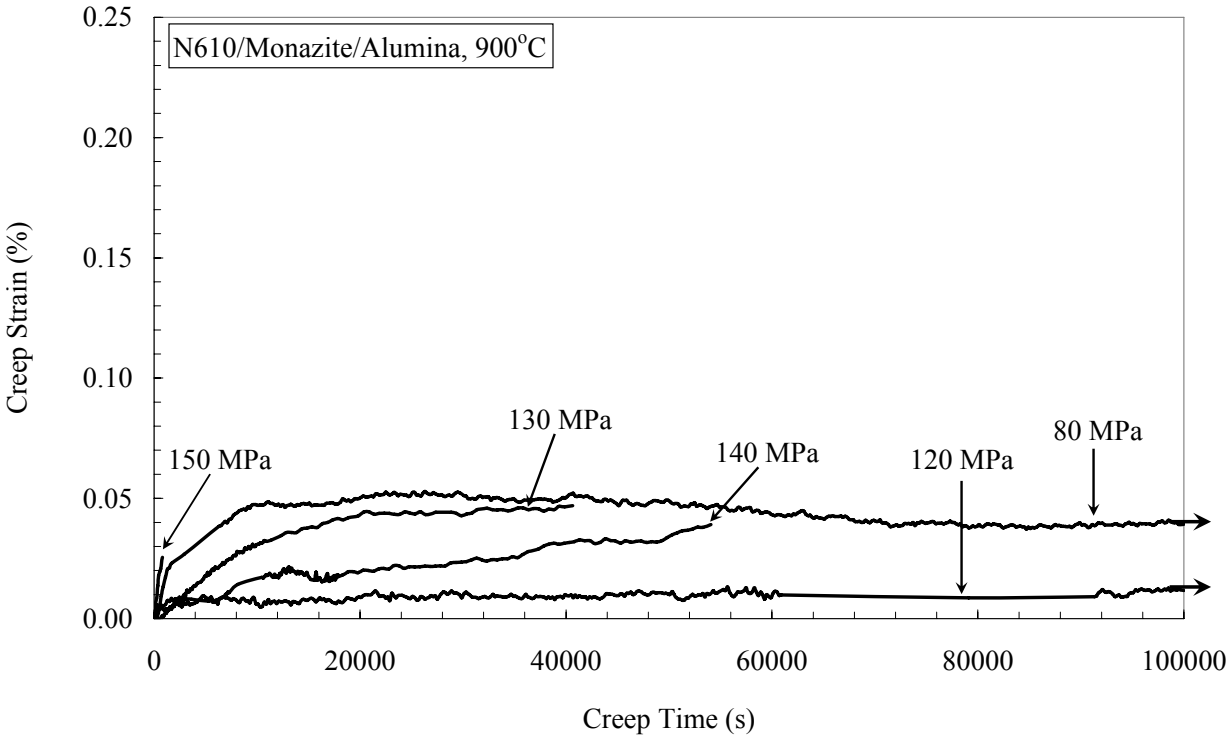

Figure 52. Creep of N610/Monazite/Alumina at 900°C

A runout was also achieved at a creep stress of 120 MPa, which was interrupted after approximately 120 h. Again, the time scale has been truncated to more easily see curves for the higher stress levels. All curves show regions of primary and secondary creep;

however, only the tests that failed showed regions of tertiary creep. The 150 MPa stress level curve displays an extremely short region of primary creep and transitions to secondary creep rapidly. A small amount a tertiary creep is also seen is this test, just before failure. Tests at stress levels of 80 and 120 MPa remained nearly linear until the test was stopped at the indicated time. Strain accumulation is still in the range or 0.00-0.05%, as in the 1000^{o}C tests.

Again, creep life has significantly improved with an 828% (at the time the test was stopped) increase at the 80 MPa creep stress level. Failure of the composite at a creep stress of 130 MPa and a runout at a creep stress of 120 MPa indicates that the operating limit at 900^{o}C lies between those stress levels. Therefore applications at this temperature must not exceed 120 MPa, or 66.63% UTS, in order to maintain a sufficiently long creep life.

Creep-rupture tests were also performed at 900^{o}C on the N610/Alumina composite at creep stresses of 73 and 80 MPa. Those curves can be seen in Figure 53, on the same scale as the results for the N610/Monazite/Alumina at 900^{o}C.

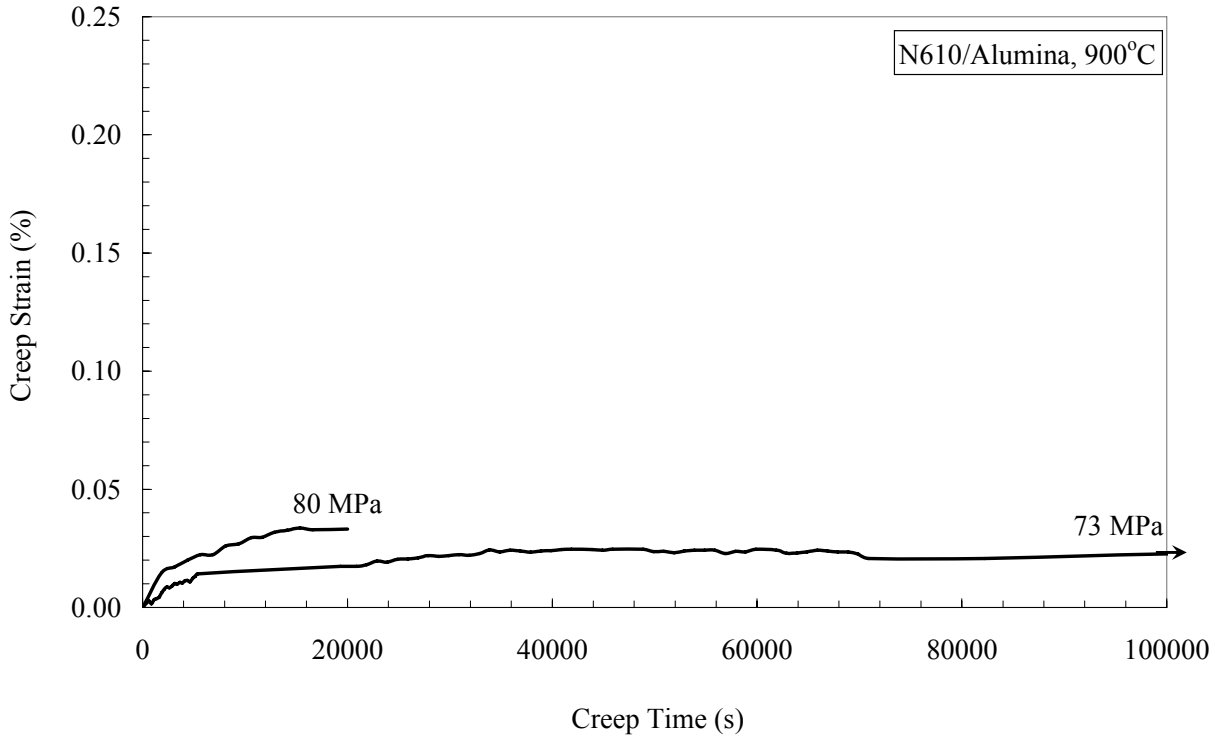

Figure 53. Creep of N610/Alumina at 900°C

Number of test specimens limited the creep testing on the N610/Alumina composite to just two stress levels. Creep life at a stress level of 80 MPa was fairly short, only surviving 19,995 seconds (5.6 h). Significant improvement in creep life is seen at a stress level of 73 MPa, as this test survived 350,055 s (97.2 h), just short of the runout criterion. Therefore the use range of the N610/Alumina composite is limited to at or below a stress level of 73 MPa, or 66.36% UTS. This is almost exactly the same range as the N610/Monazite/Alumina composite in % UTS. However, the ability of the monazite coated fibers to increase the UTS of N610/Monazite/Alumina by nearly 64%, allows the composite to operate under significantly higher loads at the same temperature. This is

clearly seen in Figure 54 which shows the creep-rupture curves for both composites at 900°C and creep stresses of 80 MPa.

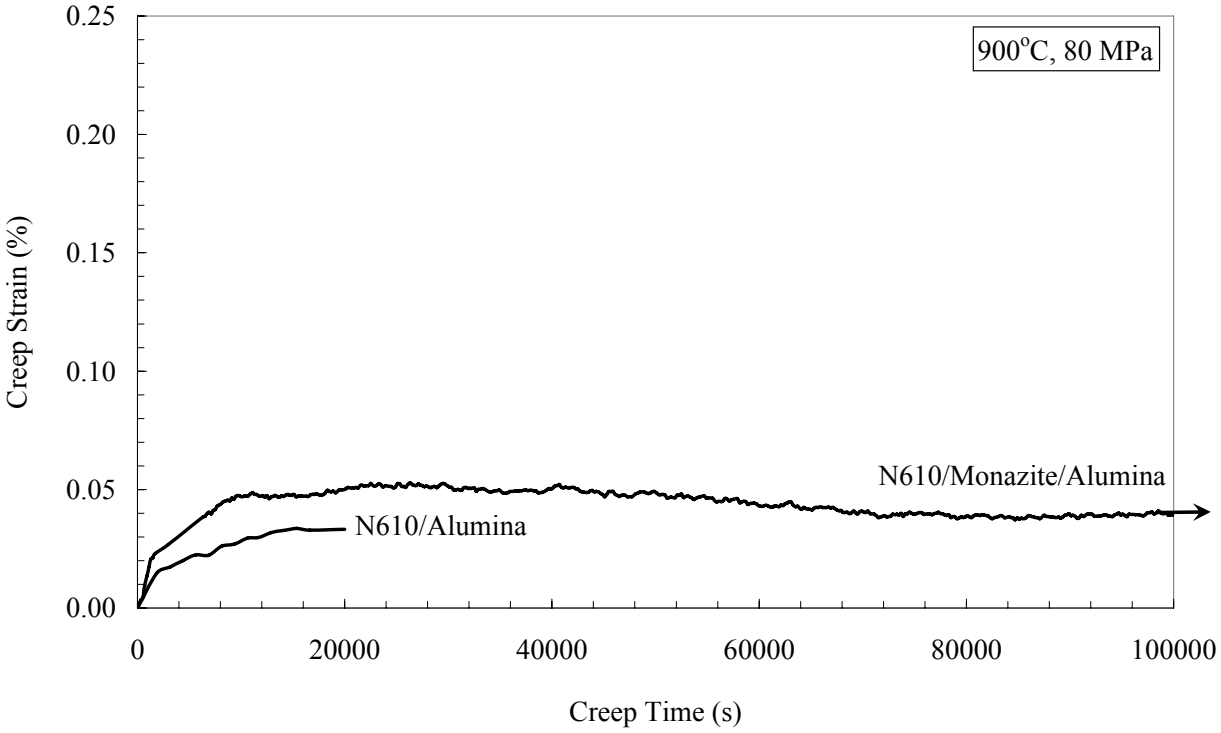

Figure 54. Creep at 900°C, 80 MPa

The N610/Alumian specimen only survived 19,995 s, while the N610/Monazite/Alumina specimen reaches 522,365 s before being stopped. This is a minimum of a 2,612% increase in creep life at this creep stress level. Creep strain accumulation is about the same for both composites, with the N610/Monazite/Alumina specimen showing slightly more creep strain which can be attributed to the propagating matrix cracks and associated fiber pullout not seen with the N610/Alumina specimen.

A comparison at similar creep stress levels in % UTS is shown in Figure 55. Neglecting the higher UTS of the N610/Monazite/Alumina composite, an increase in creep life can still be seen at the same % UTS stress level.

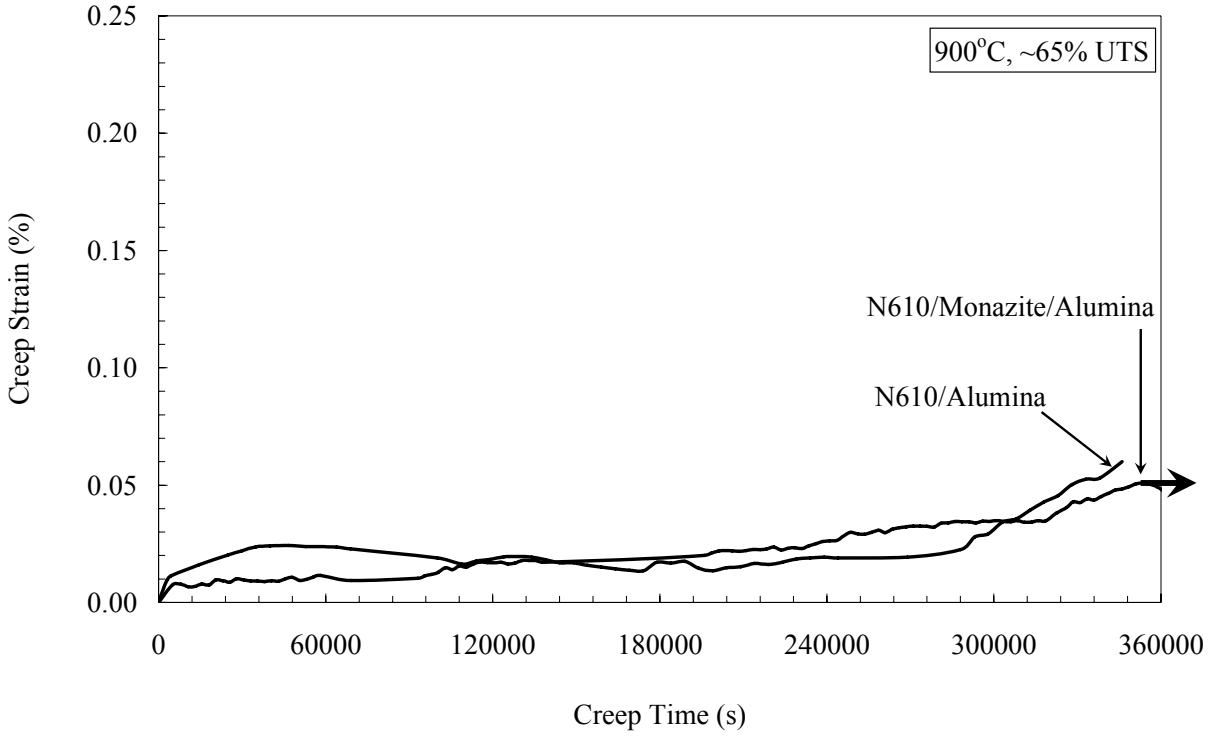

Figure 55. Creep at 900°C, ~65% UTS

At creep stresses of ~65% UTS, creep life is still increased by a minimum of 23.5% with the addition of the monazite coating. Creep strain accumulation at this stress level is similar for both composites. A region of tertiary creep is seen in the N610/Alumina curve, resulting in slightly more strain accumulation by that composite at failure. The

N610/Monazite/Alumina curves stays nearly linear until the test was stopped, as previously mentioned.

Effect of Test Temperature

By comparing creep-rupture curves at the same creep stress levels, measured in MPa, the effect of temperature on creep life can be determined for that stress level. Figure 56 shows curves for N610/Monazite/Alumina at a stress level of 80 MPa at test temperatures of 900, 1000, and 1100°C. Creep-rupture curves for specimens C3, C6, and C7 are displayed.

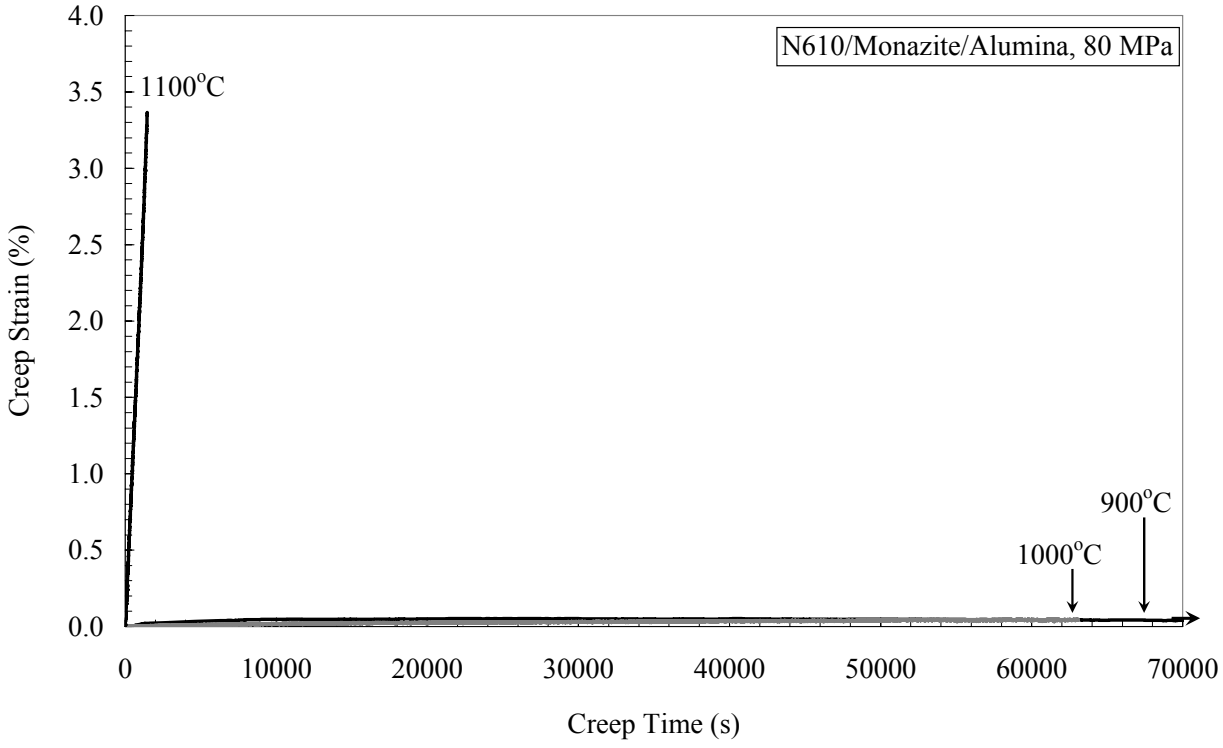

Figure 56. Creep of N610/Monazite/Alumina at 80 MPa Creep Stress

The creep time scale has again been truncated in order to see all curves clearly. As seen in the figure, there is a dramatic increase in creep life with decreasing test temperature. Creep life increases by 4,343% from 1100^{o}C to 1000^{o}C and by a minimum of 828% from 1000^{o}C to 900^{o}C. The increase in creep life between 1100^{o}C and 900^{o}C is at least 35,976%. Creep strain accumulation also reduces significantly when moving from 1100^{o}C to 1000^{o}C, decreasing 98.5% from 3.365% strain to 0.049% strain. Creep strain reduces only another 18.4% between 1000^{o}C and 900^{o}C. The total decrease in strain between 1100^{o}C and 900^{o}C is 98.8%.

Creep-rupture curves for N610/Monazite/Alumina at temperatures of 1100 and 900^{o}C for a creep stress of 120 MPa are shown in Figure 57. Creep-rupture curves for specimens C5 and C8 are displayed.

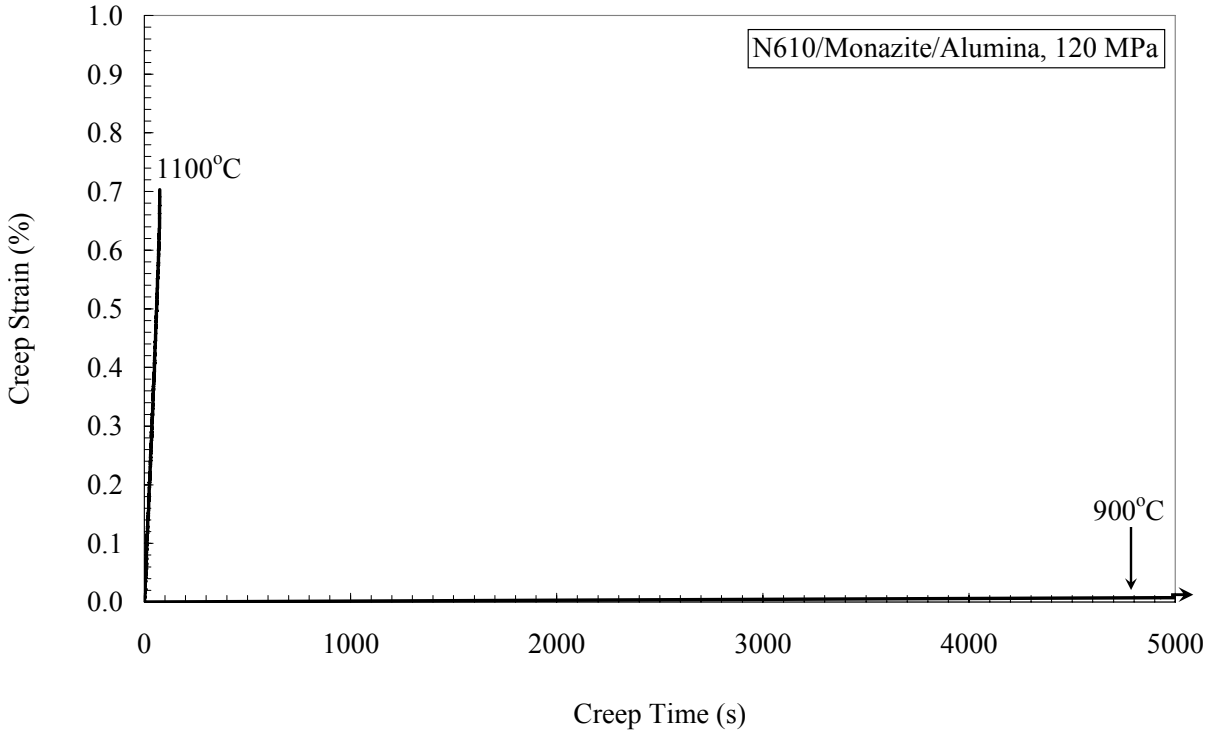

Figure 57. Creep of N610/Monazite/Alumina at 120 MPa Creep Stress

Again, significant increase in creep life and decrease in creep strain is observed for this creep stress level from 1100°C to 900°C. Creep life increased by at least 576233%, while creep strain decreased by 93.7% from 0.703% strain to 0.044% strain. At this creep stress level, change in temperature had a much greater impact on creep life than at the 80 MPa creep stress level. The reduction in creep strain was similar for both stress levels.

Next, the effect of temperature is investigated based on creep stress levels in terms of % UTS, so it is independent of the UTS for each composite. Figure 58 shows creep-rupture curves at temperature of 1100 and 900°C for a creep stress of ~65% UTS. Creep-rupture curves for specimens C4 and C8 are displayed.

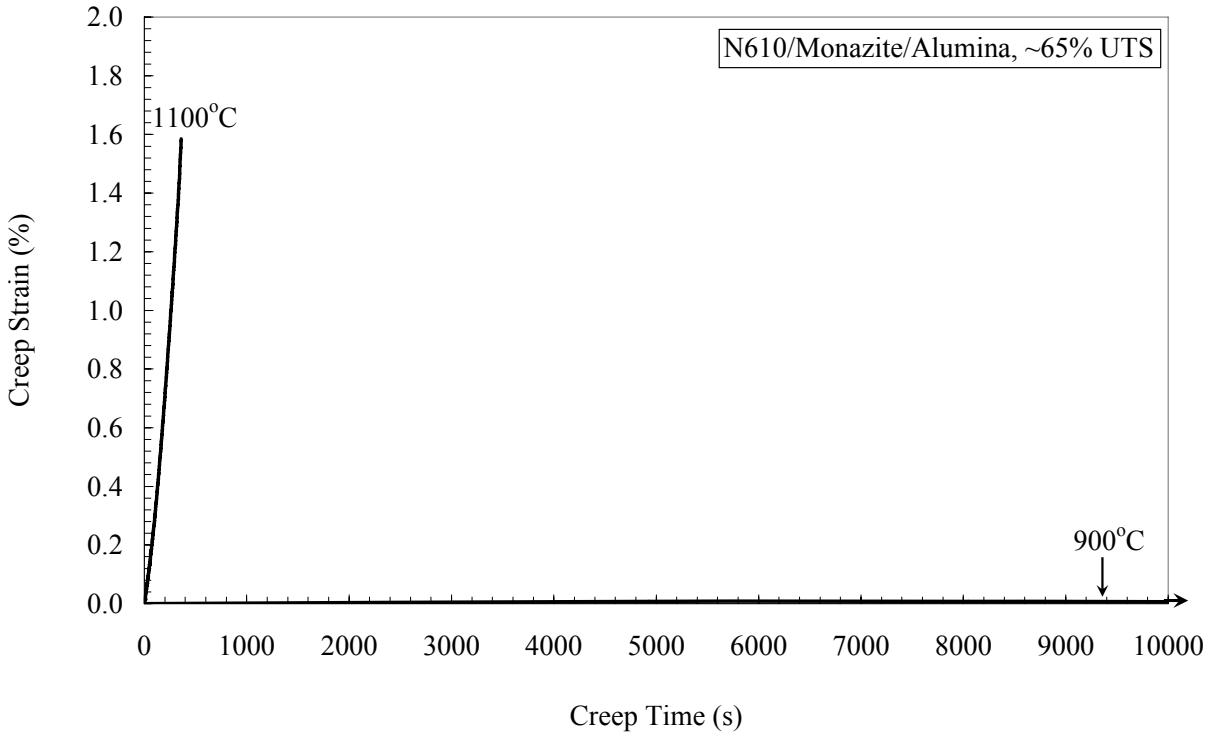

Figure 58. Creep of N610/Monazite/Alumina at ~65% UTS Creep Stress

In this case, creep life increased by at least 120,882% and creep strain decreased by 97.2%. While the composite did not perform well at 1100°C at ~65% UTS, it does however, perform well at 900°C at the same stress level with a runout at that temperature.

Figure 59 shows the effect of temperature at a stress level of ~80% UTS. Creep-rupture curves for specimens C1, C5, and C10 are displayed.

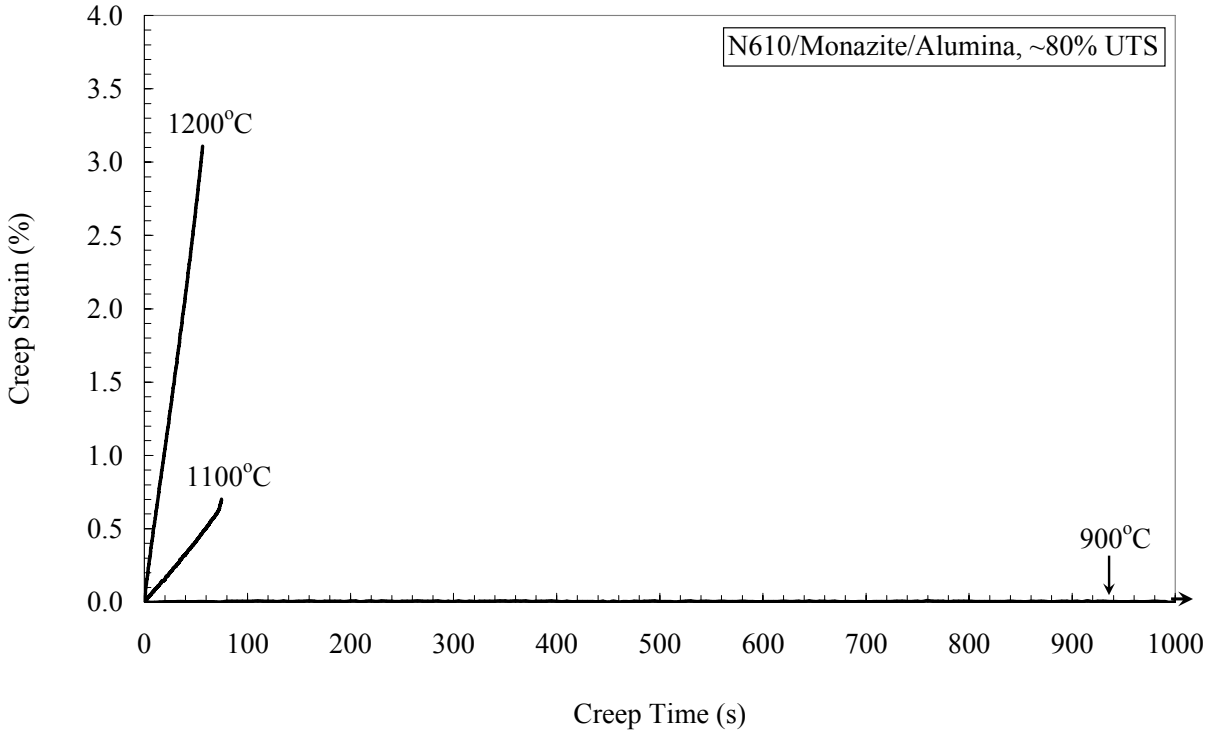

Figure 59. Creep of N610/Monazite/Alumina at ~80% UTS Creep Stress

Between temperatures of 1200°C and 1100°C, creep life only increases by 32.7%. Creep strain decreases 77.4% over the same temperature change, but is still fairly large for applications of this composite. Further decrease in temperature from 1100°C to 900°C yields an increase in creep life of 72,100% from 75 s to 54,075 s and a decrease in creep strain of 95% from 0.703% strain to 0.035% strain. While this is a significant improvement in creep life, it is still only 54,075 s (15 h) and is not sufficient to support applications of this composite at this level of creep stress.

Creep – Rupture Curves

Creep stress, in MPa, is plotted versus time to rupture for N610/Monazite/Alumina at test temperatures of 900°C, 1000°C, 1100°C, and 1200°C in Figure 60.

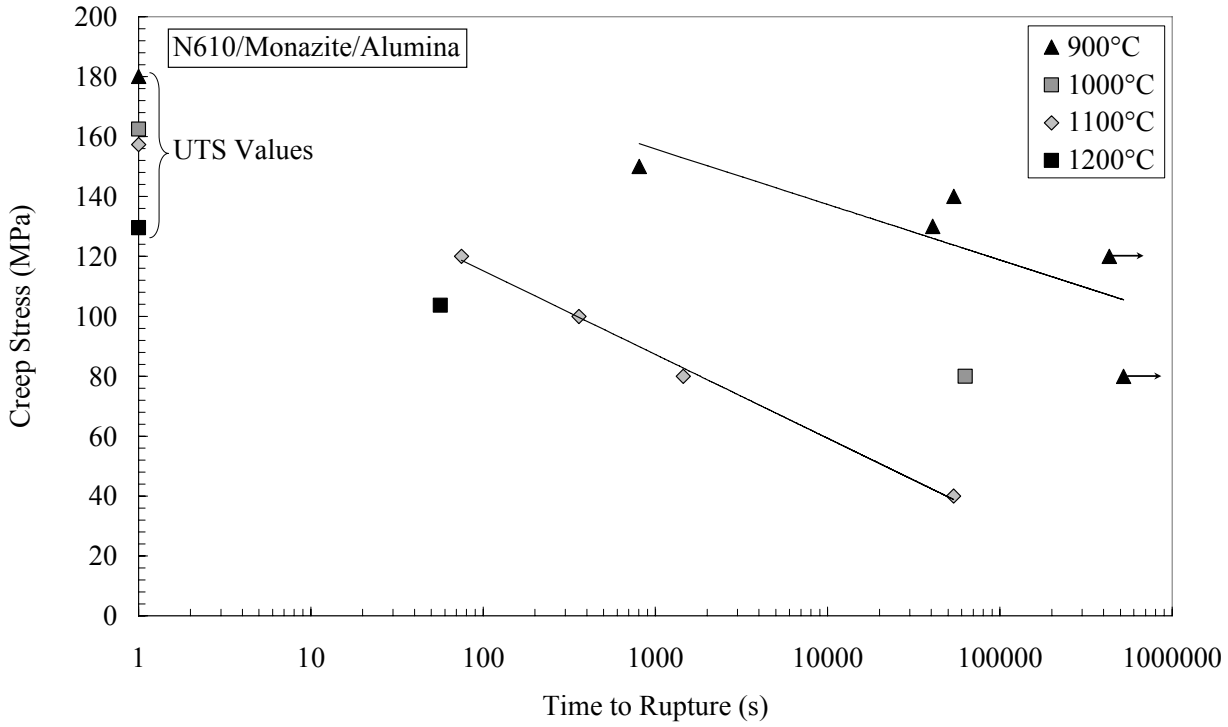

Figure 60. Creep Stress (MPa) vs. Time to Rupture for N610/Monazite/Alumina

At 1100°C, no creep stress limit can be determined as all test failed short of the runout criteria. If the trend line were extended, the composite would reach the 100 hr limit at a creep stress of approximately 20 MPa. Creep lives at this temperature are far too short for any extended application. At 900°C, failure at a creep stress 130 MPa and runout at a creep stress of 120 MPa, puts the creep stress limit at approximately 120 MPa

for this temperature. While large increases in creep life can be seen with decreasing temperature, it is not until 900°C that the composite demonstrates sufficient creep life at high enough stress levels to withstand any practical application at that temperature. Therefore, the operating limit of this composite is seen to be 900°C at stresses below 120 MPa. This corresponds to data from Johnson et al (20), which shows that the single filament strength of the N610 fiber begins to decay significantly after 900°C. Between 900°C and 1200°C, N610 loses approximately 56% of its tensile strength (20:32).

Figure 61 displays the same creep stress versus time to rupture points, but with creep stress represented in % UTS.

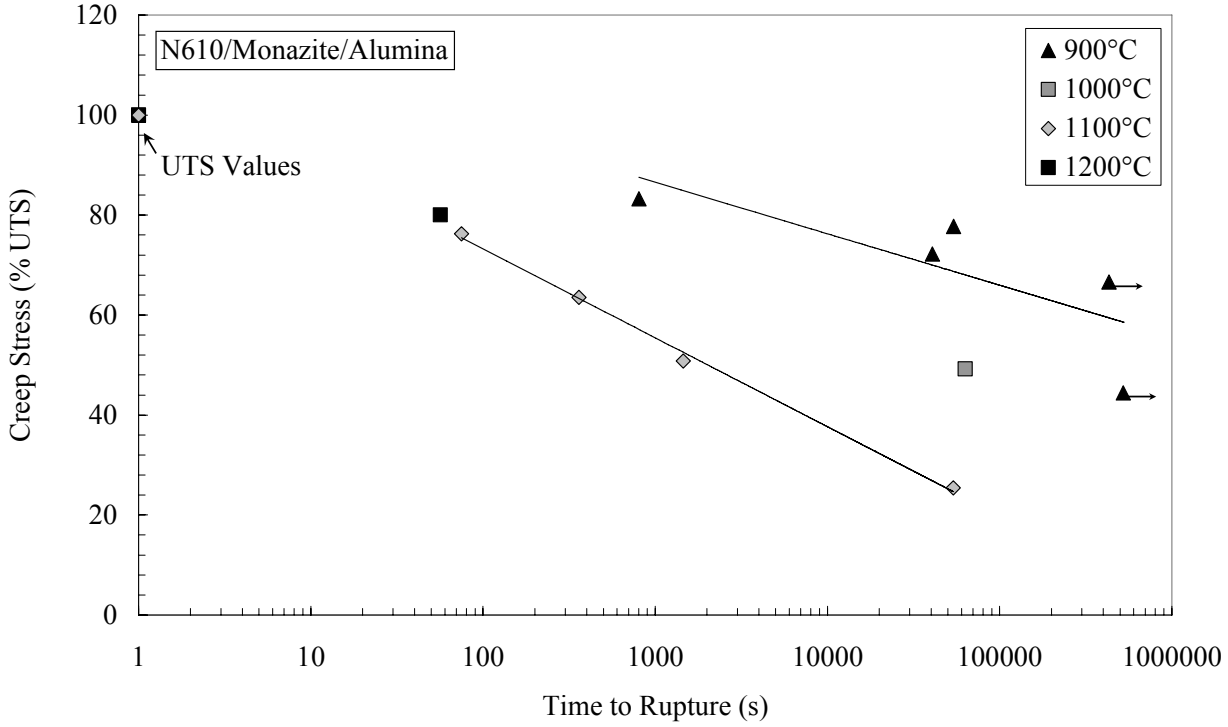

Figure 61. Creep Stress (% UTS) vs. Time to Rupture for N610/Monazite/Alumina

At 1100°C, the 100 h runout criteria would be met at approximately 13% UTS. By decreasing test temperature to 900°C, the creep stress limit has been raised to approximately 67% UTS. This much larger stress operating regime would allow the composite to be used in many high load applications at or below 900°C.

Figure 62 compares the creep stress versus time to rupture points for both N610/Monazite/Alumina and N610/Alumina at 900°C, with stress in MPa.

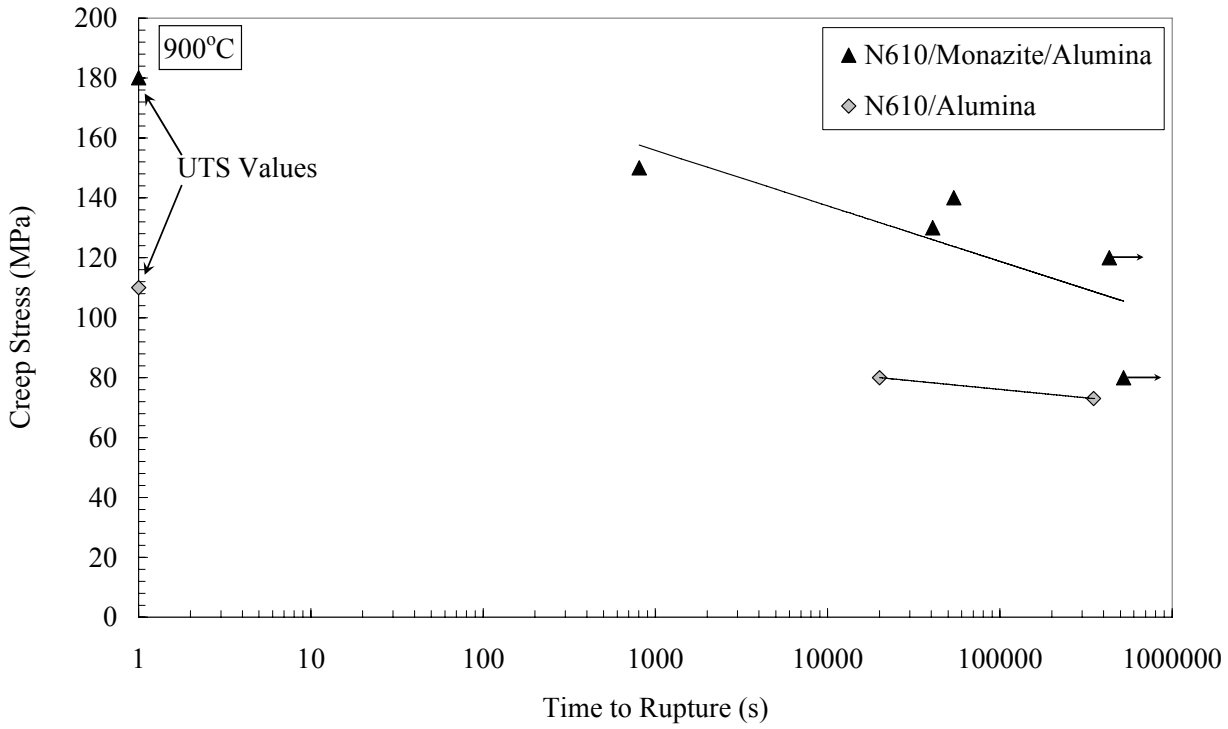

Figure 62. Creep Stress vs. Time to Rupture at 900°C (Stress in MPa)

Much of the improvement in creep life at this temperature can be attributed to the sizable increase in strength afforded by the addition of the monazite fiber coating. At a creep stress of 80 MPa, the additional of the monazite fiber coating increases creep life by at least 139.5 h (2612%). The increase in strength allows the N610/Monazite/Alumina composite to operate at lower % UTS stress levels than the N610/Alumina composite, when at the same creep stress in MPa. A creep stress limit for N610/Alumina cannot be accurately predicted from just two test points; however, it is significantly lower than that of the N610/Monazite/Alumina.

Figure 63 shows the same creep stress versus time to rupture points, but this time stress is displayed in % UTS.

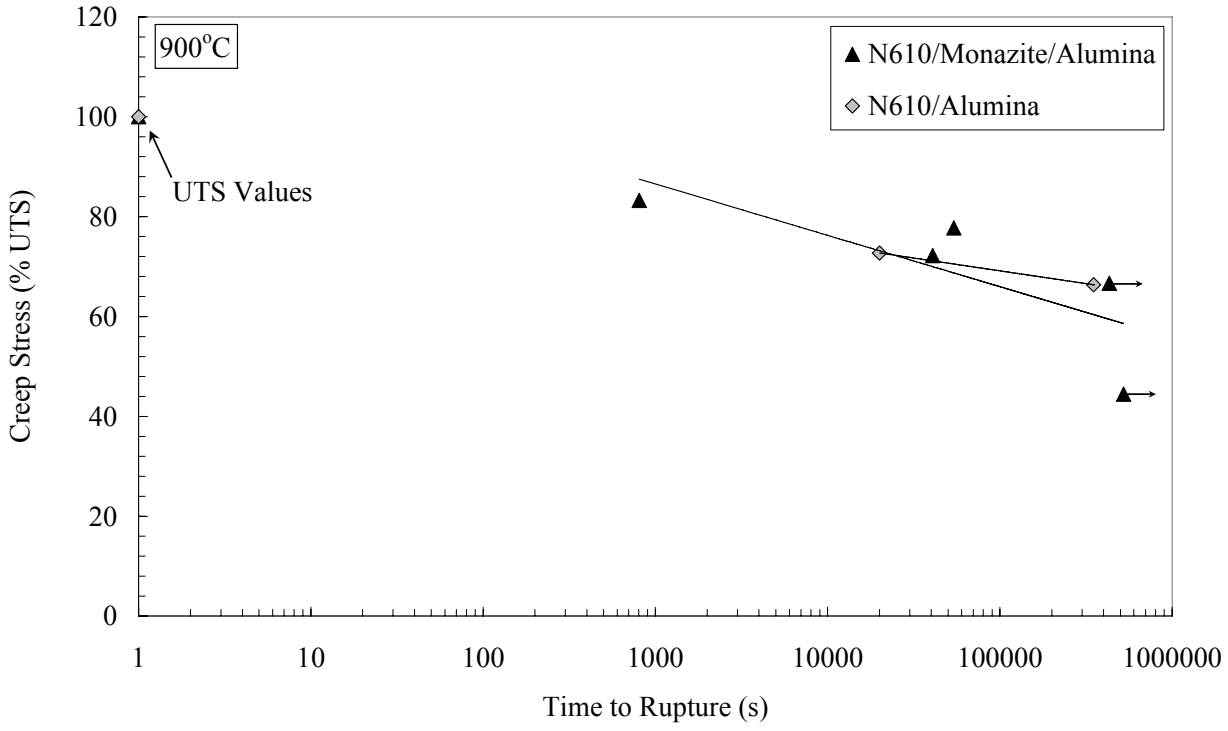

Figure 63. Creep Stress vs. Time to Rupture at 900°C (Stress in % UTS)

With the effect of the increased tensile strength unseen in this representation, the N610/Monazite/Alumina still shows increased creep life at the same % UTS stress levels. For example, at approximately 72% UTS, creep life is increased by 5.74 h (203%) and at approximately 66% UTS it is increased by 22.8 h (123%).

Creep Strain Rate vs. Creep Stress Level

Minimum creep strain rates where reached in all creep-rupture tests. Those results are summarized in Table 7. Creep rates are plotted versus creep stress for N610/Monazite/alumina at 900, 1000, 1100 and 1200^{o}C in Figure 64.

Table 7. Summary of Creep Rate Results

Specimen Number	Material	Test Temperature (^{o}C)	Creep Stress Level		Creep Rate (s^{-1})
			(MPa)	(% UTS)	
C1	N610/$LaPO_4$/Al_2O_3	1200	104	80.00	5.0315E-04
C2	N610/$LaPO_4$/Al_2O_3	1100	40	25.42	1.4153E-06
C3	N610/$LaPO_4$/Al_2O_3	1100	80	50.83	2.1112E-05
C4	N610/$LaPO_4$/Al_2O_3	1100	100	63.54	2.4577E-05
C5	N610/$LaPO_4$/Al_2O_3	1100	120	76.25	7.9016E-05
C6	N610/$LaPO_4$/Al_2O_3	1000	80	49.24	4.5900E-09
C7	N610/$LaPO_4$/Al_2O_3	900	80	44.42	1.0723E-09
C8	N610/$LaPO_4$/Al_2O_3	900	120	66.63	3.2733E-09
C9	N610/$LaPO_4$/Al_2O_3	900	130	72.19	1.2971E-09
C10	N610/$LaPO_4$/Al_2O_3	900	140	77.74	3.8377E-09
C11	N610/$LaPO_4$/Al_2O_3	900	150	83.29	1.3574E-07
C12	N610/Al_2O_3	900	73	66.36	5.5174E-10
C13	N610/Al_2O_3	900	80	72.73	6.9087E-09

Creep rates increased with both increasing stress level and decreasing test temperature. At a creep stress level of 80 MPa, creep rate decreased four orders of magnitude (99.97%) between 1100^{o}C and 1000^{o}C, but only decreased by less than one order of magnitude (76.64%) between 1000^{o}C and 900^{o}C.

Creep or stress exponent (n) values were determined from the creep rate vs. creep stress data using the temperature-independent Norton-Bailey equation:

$$\dot{\varepsilon} = A\sigma^{n} \tag{3}$$

where $\dot{\varepsilon}$ is minimum creep strain rate, A is a pre-exponential constant, σ is the creep stress level. These values are shown next to there corresponding data in each figure.

Figure 64 depicts minimum creep strain rate plotted against creep stress for the N610/Monazite/Alumina composite at temperatures of 900^{o}C, 1000^{o}C, 1100^{o}C, and 1200^{o}C.

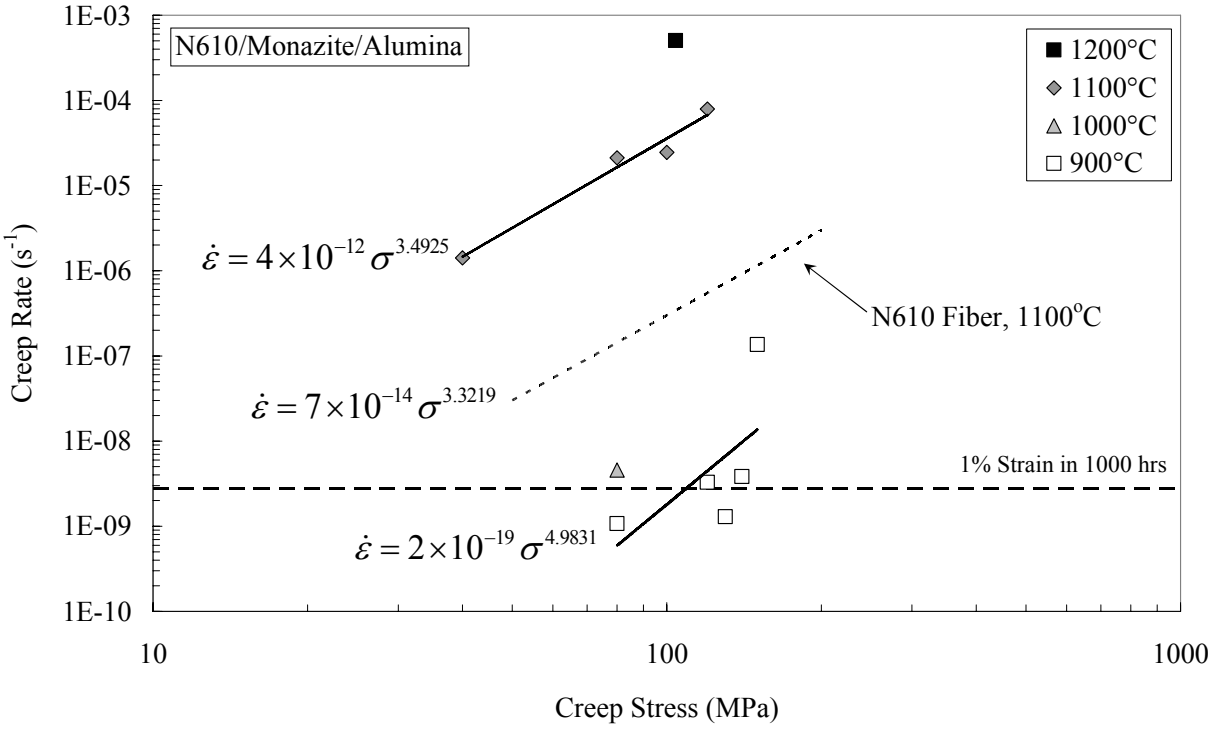

Figure 64. Creep Rate vs. Creep Stress for N610/Monazite/Alumina

The composite's stress exponent at 1100°C (3.4925) is extremely close to that of the fiber alone at 1100°C (3.3219), which demonstrates the fiber dominance during the creep process. However, the composite exhibits higher strain rates than the fiber alone for the same stress levels. This may be attributed to fiber degradation during processing which reduces creep resistance. The line depicting a strain rate corresponding to 1% strain in 1000 h (2.78 x 10^{-9}/s), indicates an allowable threshold value for extended use at elevated temperatures. At 900°C, the composite operates around the threshold value, while at higher temperatures the creep rates are too high for practical use.

Figure 65 displays creep rate vs. creep stress data plotted for both composites at a test temperature of 900°C.

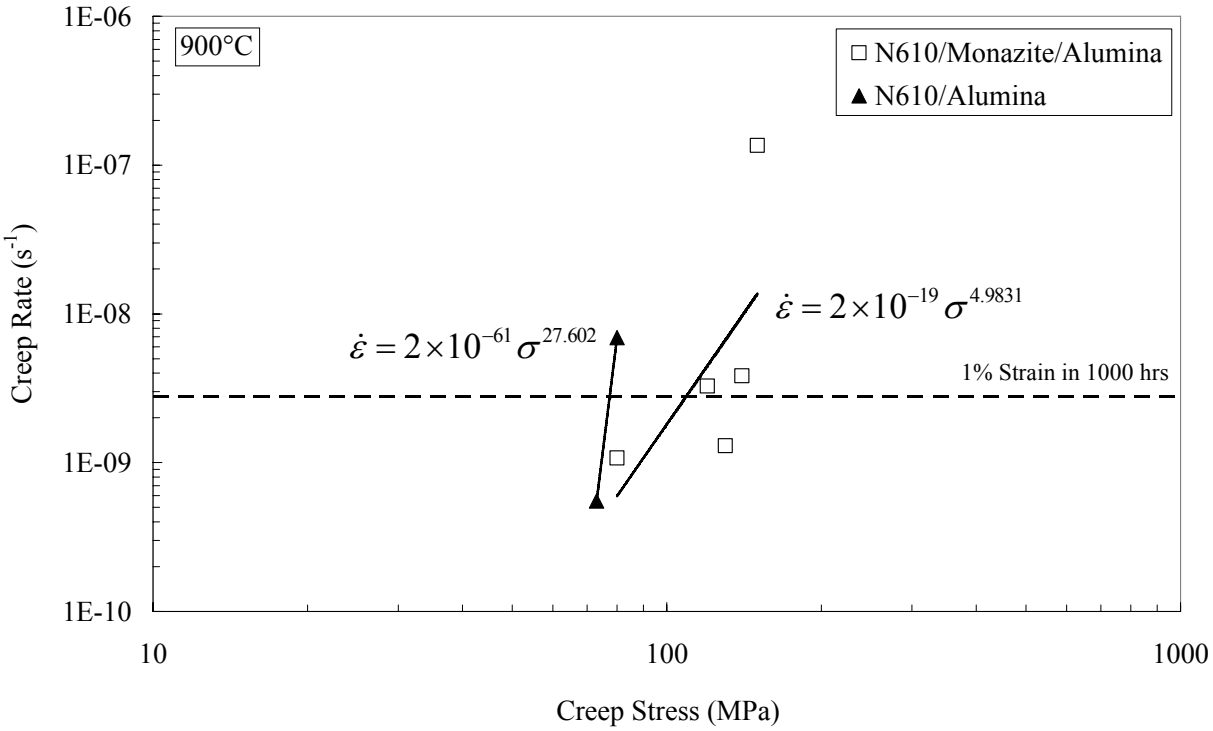

Figure 65. Creep Rate vs. Creep Stress at 900°C

Both composites show strain rates in approximately the same range. The stress exponent for N610/Alumina (27.602) is over five times that of N610/Monazite/Alumina (4.9831). This can partially be attributed to the fact that the N610.Alumina composite was only tested in the 66-73% UTS range, while the N610/Monazite/Alumina was tested in the 44-83% UTS range. If plotted over the same stress range, in % UTS, both materials would show similar high stress exponents. Strictly looking at stress level in MPa, the

N610/Monazite/Alumina composite is able to perform better at significantly higher stress levels. This again, can be attributed to the ability of the monazite coating to increase the strength of the composite by nearly 64%.

Residual Properties

Monotonic tensile tests to failure were performed on both of the runout specimens at 900°C to obtain residual properties. These results are summarized in Table 8.

Table 8. Summary of Residual Properties

Specimen Number	Test Type	UTS		Modulus, E		ε_f (%)
		(MPa)	(% Retained)	(GPa)	(% Retained)	
T1	Tensile	180.09	N/A	83.06	N/A	0.3115
C7	Creep (80 MPa for 164 h)	173.10	96.12	80.02	96.34	0.2800
C8	Creep (120 MPa for 120 h)	164.52	91.35	74.94	90.22	0.2870

Figure 66 shows the stress-strain curves for both runout specimens along with the original 900°C stress-strain curve obtained via tensile test to failure.

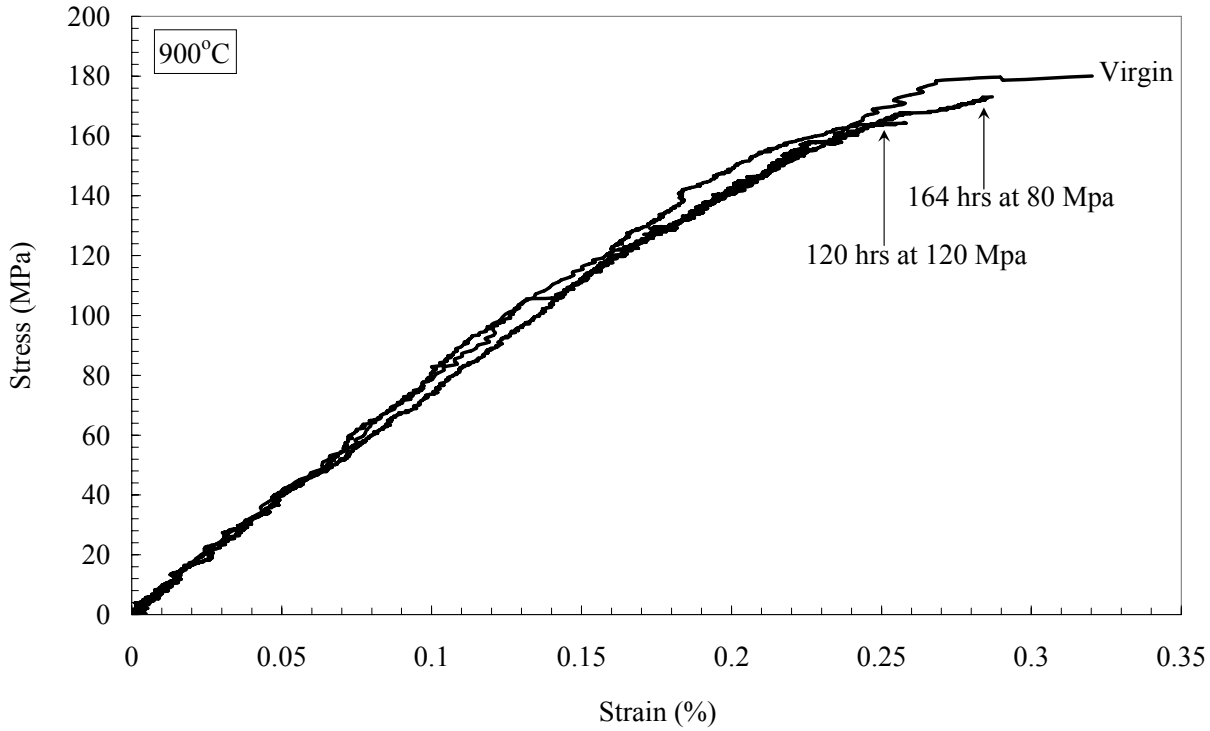

Figure 66. Stress-Strain Curves for Residual Tensile Tests

Both specimens retained a significant amount of tensile strength and elastic modulus. Similar amounts of loss are seen for both strength and modulus for each specimen. Greater losses are seen in the specimen that was exposed to the higher creep stress level. The specimen that was exposed to the lower creep stress level accumulated less strain at failure. This may be due to the longer exposure of 164 h to elevated temperature compared to 120 h for specimen C8.

Such small amounts of loss in strength and stiffness, along with the small amounts of creep strain accumulation, demonstrate the composite's ability to perform well even after 100+ h at 900°C.

Microstructure

Images of fracture surfaces of the N610/Monazite/Alumina composite at all temperatures and creep stress levels display large amounts of uniformly distributed fiber pullout. Fibers pulled out as single filaments or as small bundles in all cases.

The fracture surface for the creep test performed at 1200°C with a stress level of 103.6 MPa can be seen in Figure 67 and from the side in Figure 68. Specimen width is approximately 10 mm and thickness is approximately 3 mm.

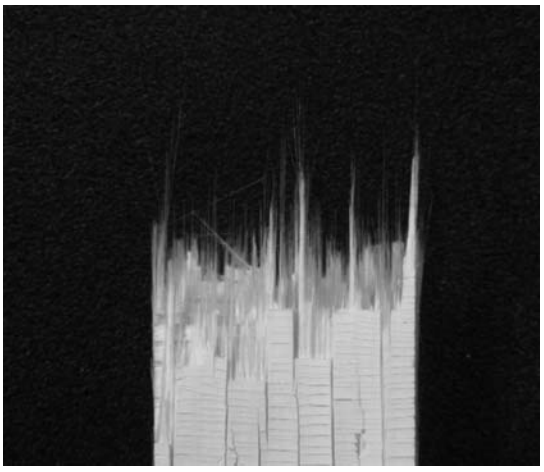

Figure 67. Creep Fracture Surface of N610/Monazite/Alumina at 1200°C

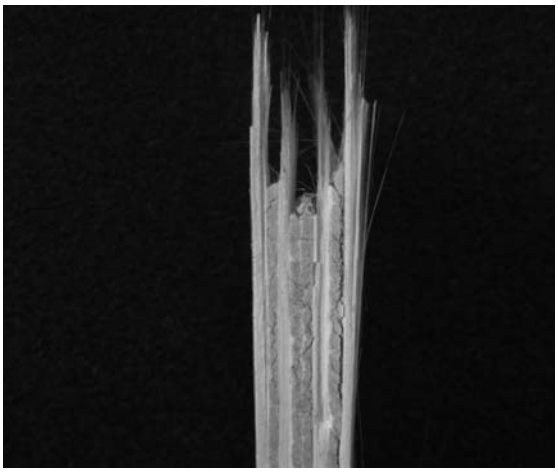

Figure 68. Creep Fracture Surface of N610/Monazite/Alumina at 1200°C (Side)

The side view shows failures occurred at different levels in each ply. Mechanisms for failure are depicted back in Figure 24.

For tests at 1100°C, fiber pullout length in N610/Monazite/Alumina specimens is directly proportional to the creep stress level. Pullout length increases with increasing stress level; however, creep strain at failure is inversely proportional to pullout length. The fracture surfaces for the N610/Monazite/Alumina specimens tested in creep at

1100°C are shown in Figure 69 from a creep stress of 40 MPa, in Figure 70 from a creep stress of 80 MPa, in Figure 71 from a creep stress of 100 MPa, and in Figure 72 from a creep stress of 120 MPa. Specimen widths are all approximately 10 mm.

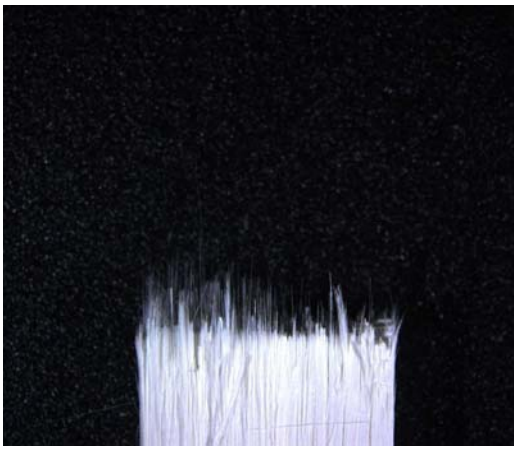

Figure 69. Creep Fracture Surface of N610/Mon/Alumina at 1100°C, 40 MPa

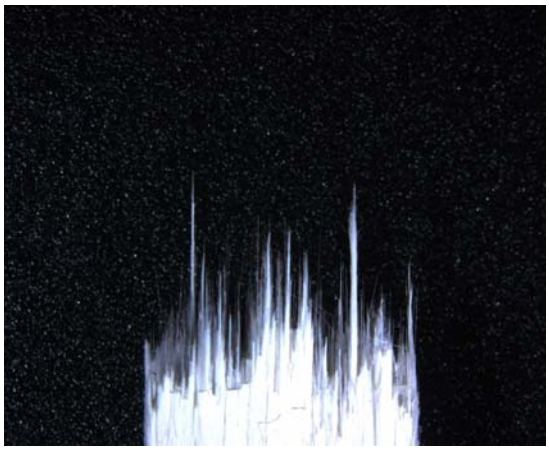

Figure 70. Creep Fracture Surface of N610/Mon/Alumina at 1100°C, 80 MPa

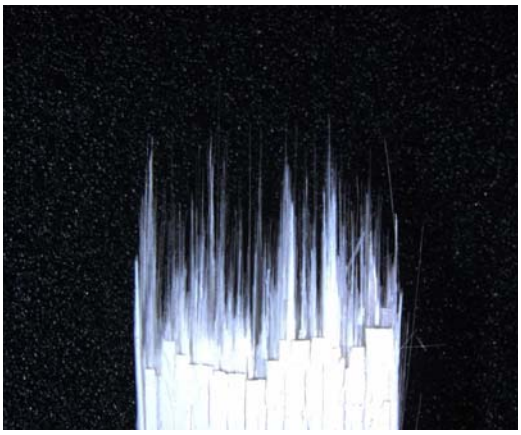

Figure 71. Creep Fracture Surface of N610/Mon/Alumina at 1100°C, 100 MPa

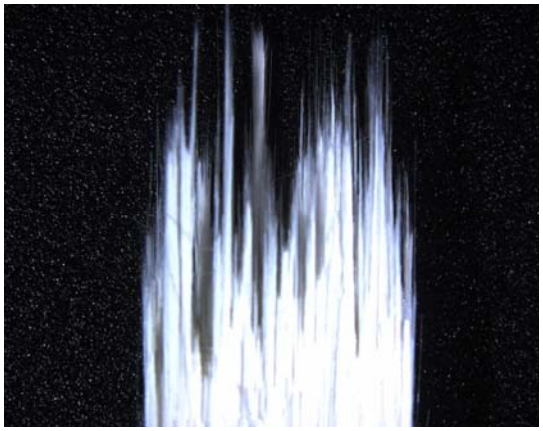

Figure 72. Creep Fracture Surface of N610/Mon/Alumina at 1100°C, 120 MPa

Side views of these fracture surfaces can be see in Figure 73 from a creep stress of 40 MPa, in Figure 74 from a creep stress of 80 MPa, in Figure 75 from a creep stress of

100 MPa, and in Figure 76 from a creep stress of 120 MPa. Specimen thicknesses are all approximately 3.6 mm.

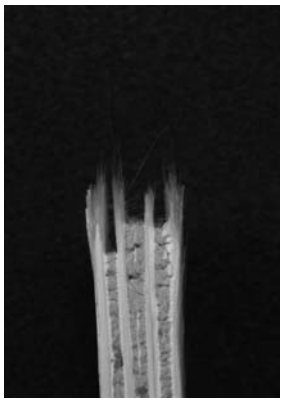

Figure 73. Creep Fracture Surface of N610/Mon/Alumina at 1100°C, 40 MPa (Side)

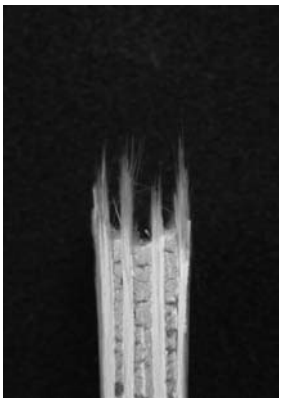

Figure 74. Creep Fracture Surface of N610/Mon/Alumina at 1100°C, 80 MPa (Side)

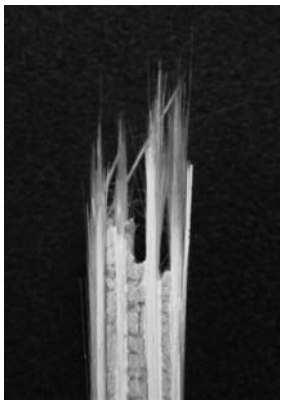

Figure 75. Creep Fracture Surface of N610/Mon/Alumina at 1100°C, 100 MPa (Side)

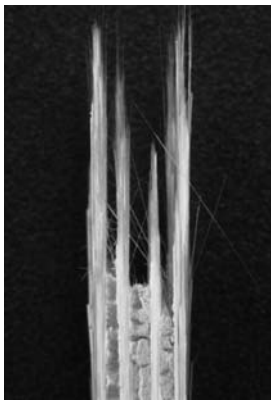

Figure 76. Creep Fracture Surface of N610/Mon/Alumina at 1100°C, 120 MPa (Side)

Fiber pullout is evenly distributed among each of the 0° plies, although lengths vary between plies. Even though fibers experience maximum stress values at the plane of the matrix crack (16:27), they fail at a different location. Fiber failure location depends on many factors, including internal flaws, sintering with the matrix, and degradation/oxidation.

Fracture surface at 1000°C with a creep stress of 80 MPa can be seen in Figure 77, with a side view in Figure 78. Specimen thickness is approximately 10 mm and thickness is approximately 4mm.

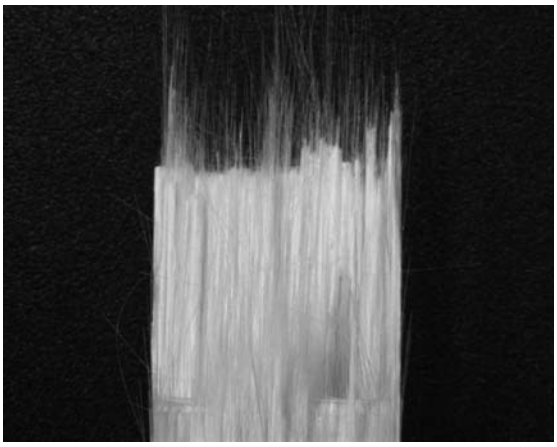

Figure 77. Creep Fracture Surface of N610/Monazite/Alumina at 1000°C

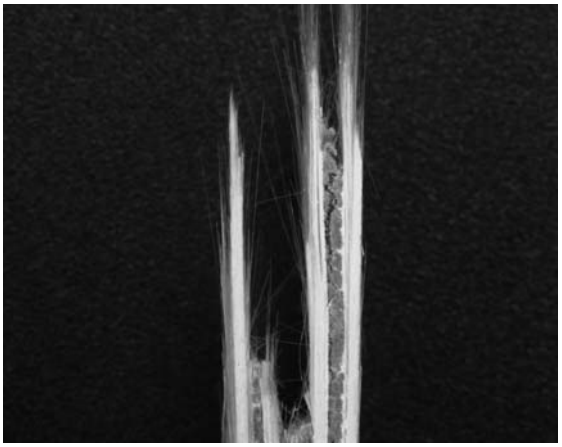

Figure 78. Creep Fracture Surface of N610/Monazite/Alumina at 1000°C (Side)

Again, the fracture surface is covered with uniformly distributed fiber pullout. Transverse plies failed at very different heights, which can barely be seen in the picture. Pullout length is again fairly long for a small creep strain at failure, as in the 1100°C tests.

Fracture surfaces for the N610/Monazite/Alumina specimens tested in creep at 900°C are shown in Figure 79 from a creep stress of 80 MPa, in Figure 80 from a creep stress of 120 MPa, in Figure 81 from a creep stress of 130 MPa, in Figure 82 from a creep stress of 140 MPa, and in Figure 83 from a creep stress of 150 MPa. Side views can be seen in Figure 84 – Figure 88. Specimen widths are all approximately 10 mm and thicknesses are approximately 4.2 mm.

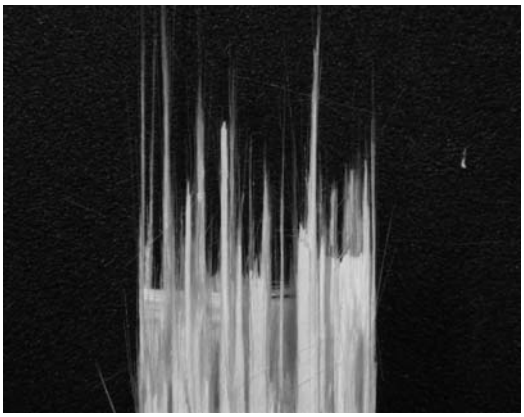

Figure 79. Creep Fracture Surface of N610/Mon/Alumina at 900°C, 80 MPa

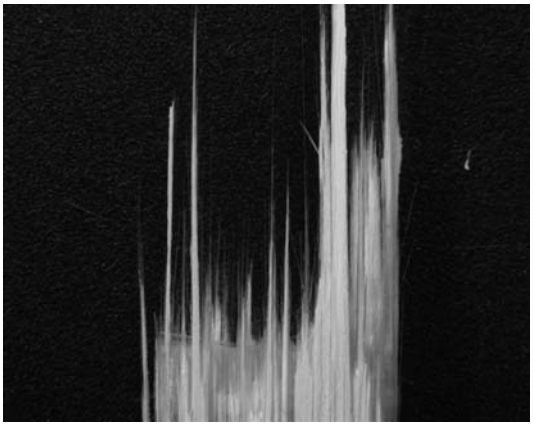

Figure 80. Creep Fracture Surface of N610/Mon/Alumina at 900°C, 120 MPa

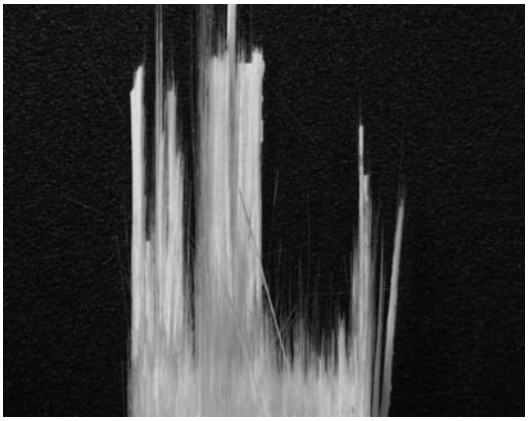

Figure 81. Creep Fracture Surface of N610/Mon/Alumina at 900°C, 130 MPa

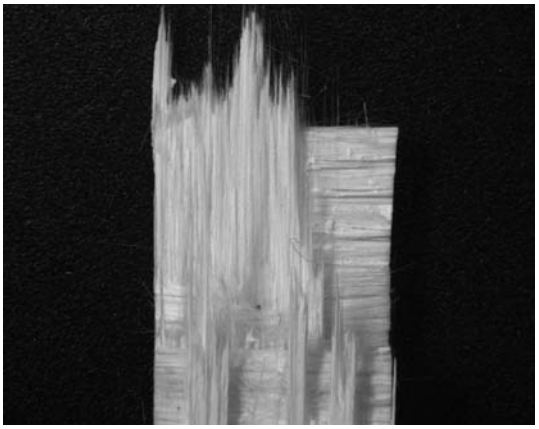

Figure 82. Creep Fracture Surface of N610/Mon/Alumina at 900°C, 140 MPa

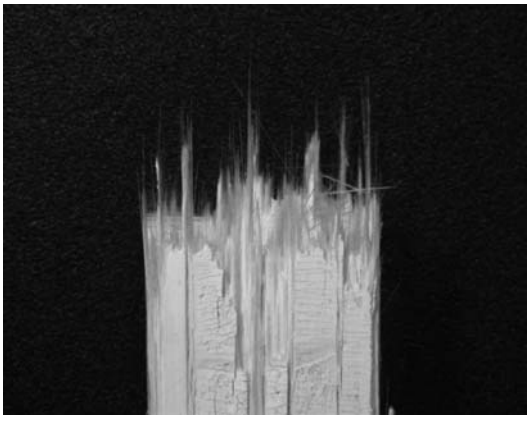

Figure 83. Creep Fracture Surface of N610/Mon/Alumina at 900°C, 150 MPa

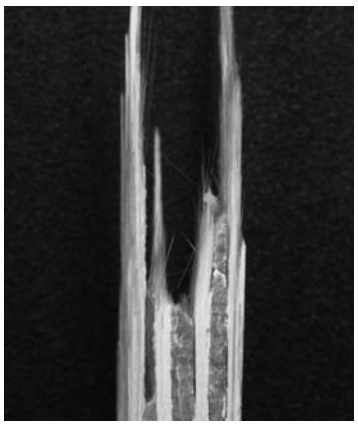

Figure 84. Creep Fracture Surface of N610/Mon/Alumina at 900°C, 80 MPa (Side)

Figure 85. Creep Fracture Surface of N610/Mon/Alumina at 900°C, 120 MPa (Side)

Figure 86. Creep Fracture Surface of N610/Mon/Alumina at 900°C, 130 MPa (Side)

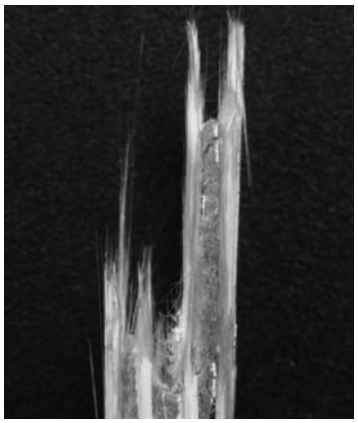

Figure 87. Creep Fracture Surface of N610/Mon/Alumina at 900°C, 140 MPa (Side)

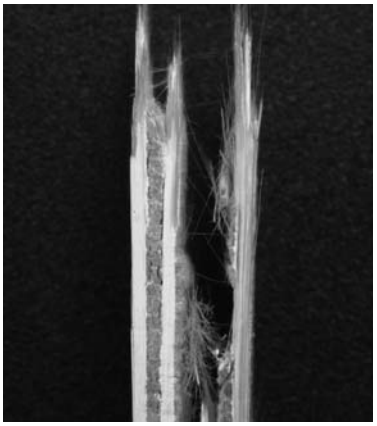

Figure 88. Creep Fracture Surface of N610/Mon/Alumina at 900°C, 150 MPa (Side)

Fracture surfaces show randomly distributed and bundled regions fiber pullout at all stress levels except 150 MPa. Test time for the creep stress of 150 MPa was two orders of magnitude lower than those at 130 and 140 MPa, and three orders of magnitude lower

than those at 80 and 120 MPa. Longer exposure to elevated temperature, in tests at lower than 150 MPa stress levels, may have caused the fibers to sinter together causing the bundled pullout. Length of fiber pullout does not show any dependence on stress level.

On a microscopic scale, fractures surfaces all display the same characteristics from every temperature and stress level. Generally, they show planar fracture across the 90o plies and randomly distributed lengths of fiber pullout. Pullout is seen as both single filaments and in bundles with no dependence on temperature or stress level. Micrographs produced using the SEM will thus be discussed in a general sense referring to all creep tests.

Figure 89 shows a good example of crack deflection, where a surface crack caused the matrix to fail, but was deflected after propagating through only a few of fibers in the tow. Also seen in the picture is the lack of matrix infiltration into the fiber tows. Matrix material builds up on the outer surface of the composite, but does not work its way in between the fibers. This is caused by bridging of the fibers due to the presence of monazite coating. The monazite fills the spaces between the fibers not allowing the matrix to penetrate.

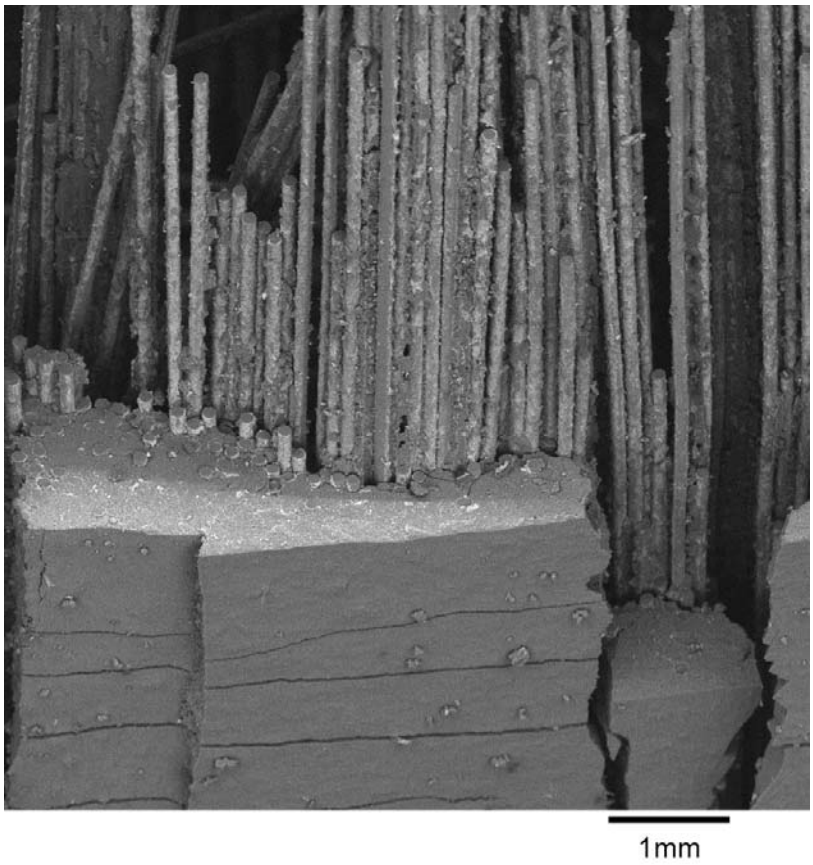

Figure 89. SEM Image showing Crack Deflection at 200x Magnification

At 1000x magnification the debonding of the fiber can barely be seen as gaps between the pulled out fibers and the matrix material. Residue of the monazite coating and small bits of matrix are still attached to the fiber surfaces. Figure 90 is a close up of the matrix/fiber interface showing crack deflection. Figure 91 is a view of just the pulled out fibers showing coating and matrix particles still attached to the fibers.

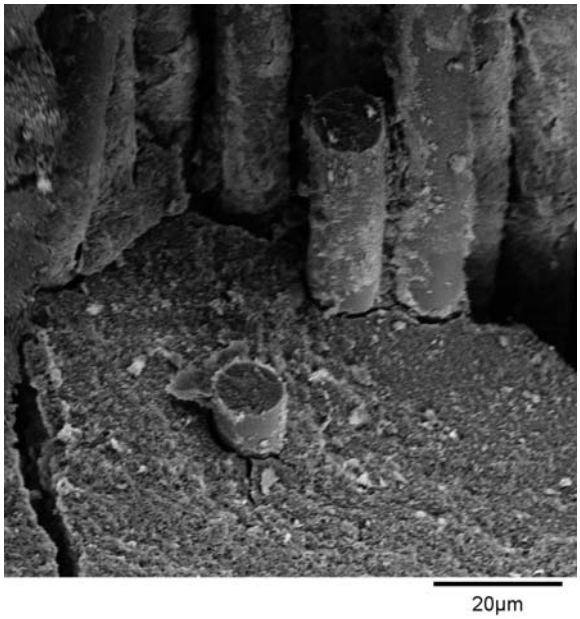

Figure 90. SEM Image shows Crack Deflection at 1000x Magnification

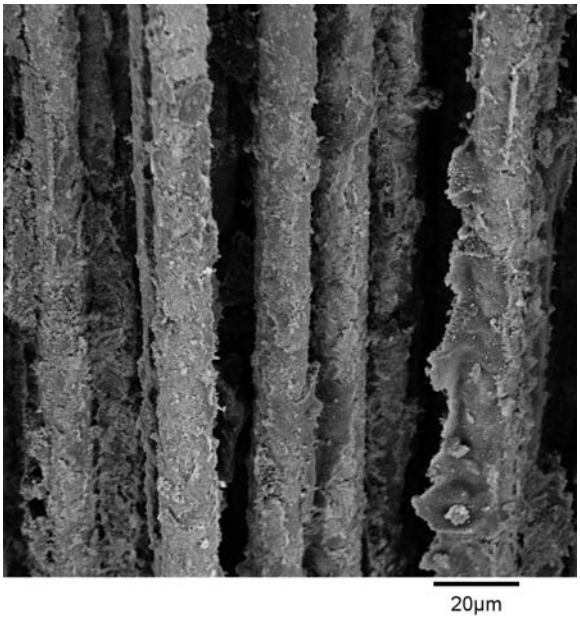

Figure 91. SEM Image shows Pulled Out Fibers at 1000x Magnification

Debonding of the fiber from the matrix can clearly be seen in Figure 92, where the fibers have pealed away from the matrix material. Figure 93 shows a surface flaw that propagated inward causing a large bundle of fibers to debond and pullout, leaving a large hole. Other fibers, still attached to the matrix material, pulled out as a bundle as well from the opposite direction.

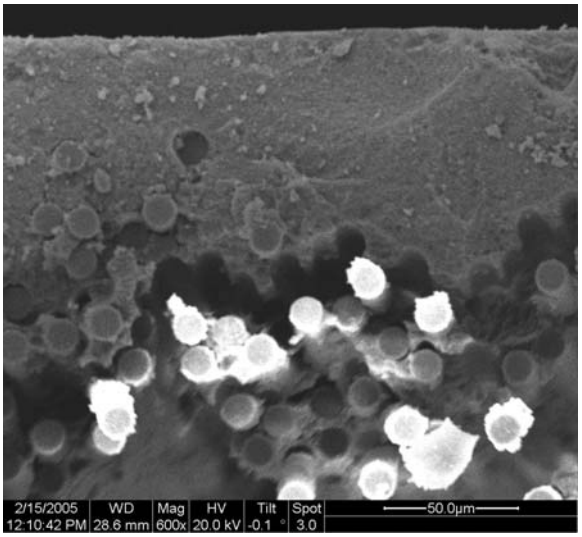

Figure 92. SEM Image shows Fiber/Matrix Debonding at 600x Magnification

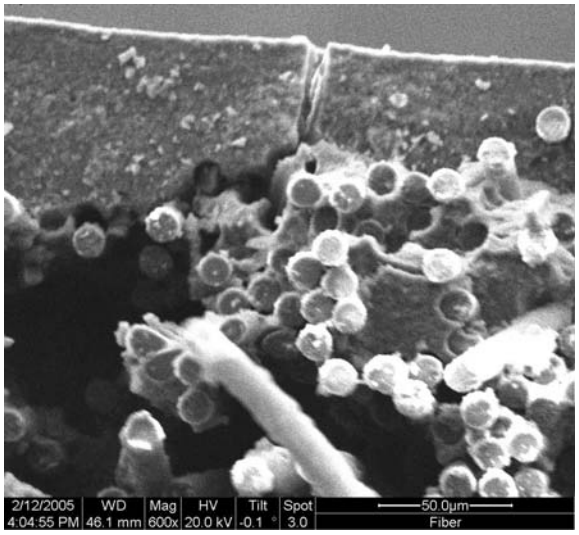

Figure 93. SEM Image shows Surface Flaw and Fiber Pullout at 600x Magnification

Figure 94 and Figure 95 both show regions of extensive fiber pullout. Even though the fibers are bunched up in a tow, pullout lengths still vary greatly within the tow showing that the monazite coating has prevented the fibers from sintering together at elevated temperatures. The pictures also show small regions of bundled fibers which have fractured along the same plane and may have become sintered together allowing a crack to propagate straight through the bundle. Some sockets resulting from pullout can also be seen in both images as holes from single fibers or from bundles which pulled out together.

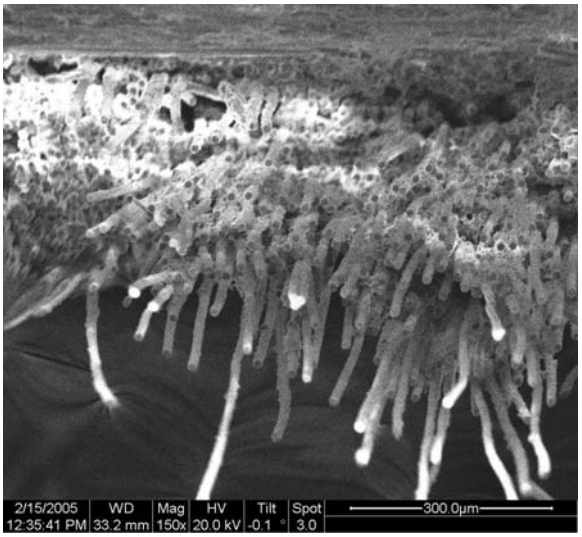

Figure 94. SEM Image shows Fiber Pullout at 150x Magnification

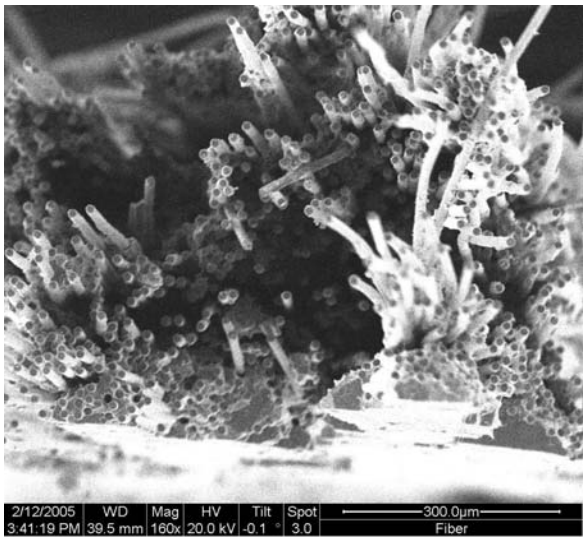

Figure 95. SEM Image shows Fiber Pullout at 150x Magnification (2)

Figure 96 shows a region of fibers adjacent which have fractured along the same plane as the adjacent 90^{o} ply. Again matrix volume is higher at the edge of the ply and fibers are much more sparsely distributed.

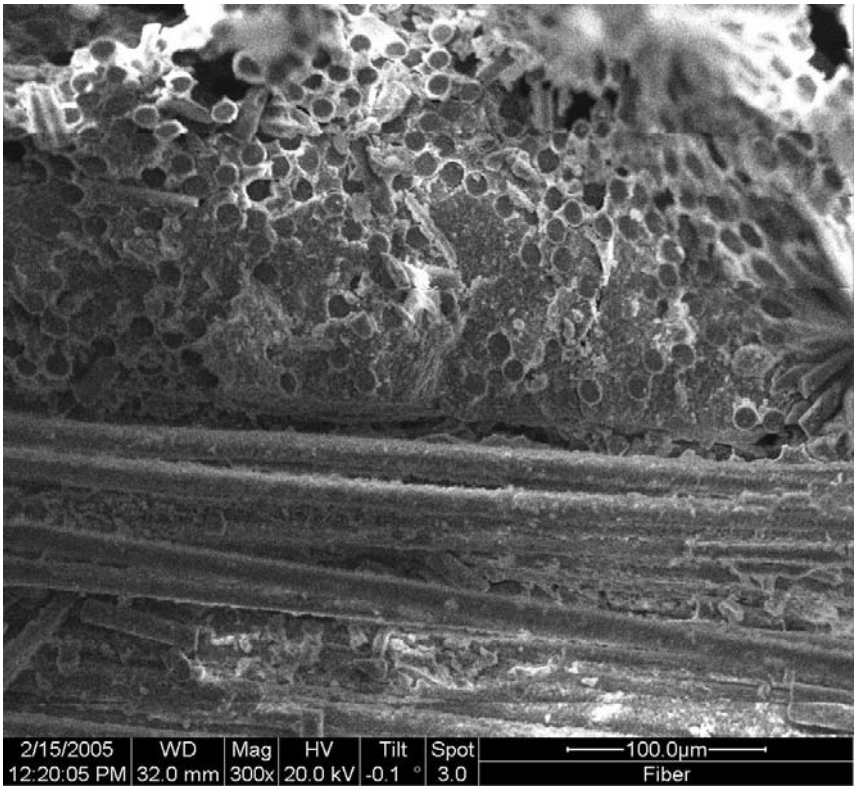

Figure 96. SEM Image shows Planar Fracture in a 0^{o} Ply at 300x Magnification

For N610/Alumina specimens tested in creep at 900^{o}C, fracture surfaces also resemble tensile fracture surfaces. Fiber pullout is less uniformly distributed than in tensile test specimens, with plies displaying mostly planar fractures at different levels. Figure 97 shows the fracture surface for the specimen with a creep stress of 73 MPa, with side view in Figure 98. Figure 99 shows the fracture surface for the specimen with a creep stress of 80 MPa, with side view in Figure 100. Specimen widths are approximately 10 mm and thicknesses are approximately 3 mm.

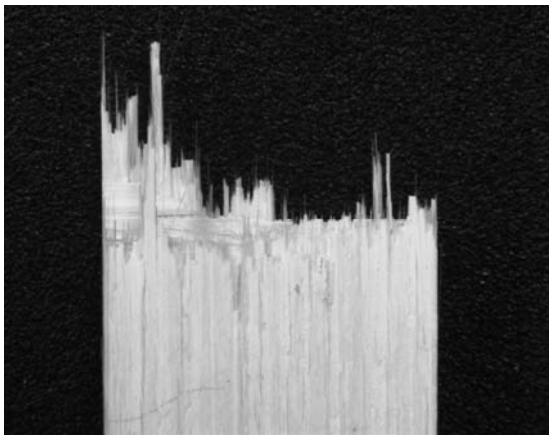

Figure 97. Creep Fracture Surface for N610/Alumina at 900°C, 73 MPa

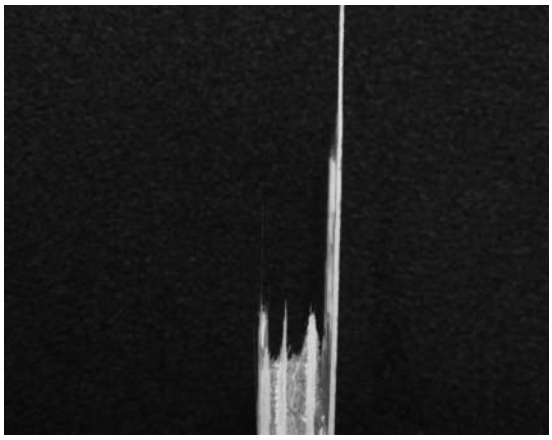

Figure 98. Creep Fracture Surface for N610/Alumina at 900°C, 73 MPa (Side)

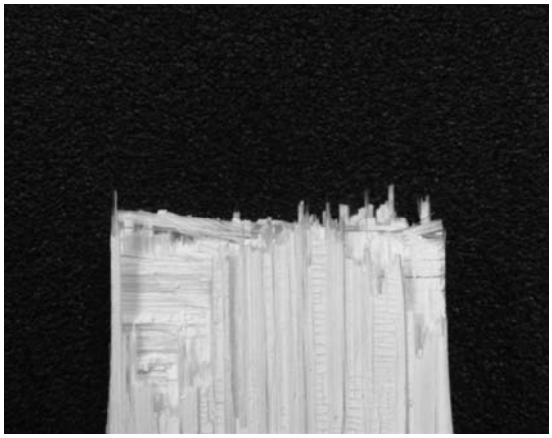

Figure 99. Creep Fracture Surface for N610/Alumina at 900°C, 80 MPa

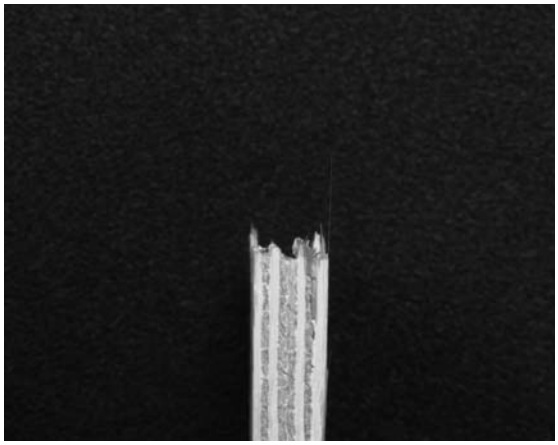

Figure 100. Creep Fracture Surface for N610/Alumina at 900°C, 80 MPa (Side)

Microstructural images of fracture surfaces also look like those from tensile test. Large sections of planar fracture can be seen with small amounts of fiber pullout. Figure 101 shows a few sections of perfectly planar fractures surrounded by sections where large bundles of fibers have been pulled out together. Three plies can be seen in the lower magnification image in Figure 102, having fracture at the dame level. Some areas show bundles of fibers that have been pullout out where there is less matrix material.

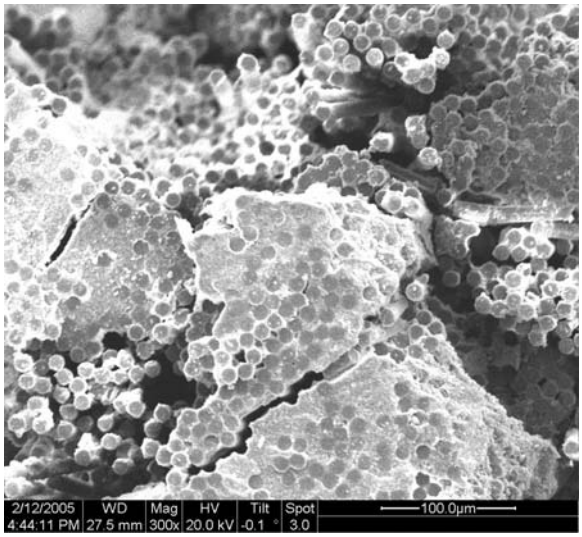

Figure 101. SEM Image shows Planar Fracture Surfaces at 300x Magnification

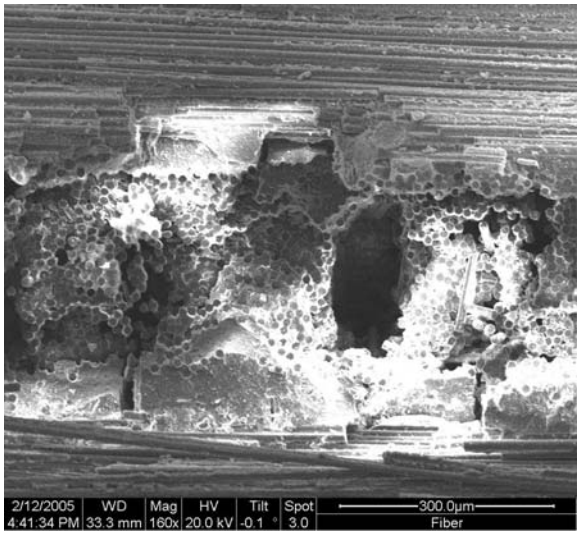

Figure 102. SEM Image shows Planar Fracture Across 3 Plies at 160x Magnification

VI. Concluding Remarks

Conclusions

Results have shown that the addition of monazite coating to the fibers of the N610/Alumina composite has significantly increased its performance in both monotonic tension and creep at all test temperatures and creep stress levels. In addition by significantly increasing the tensile strength, the monazite fiber coating has allowed the composite to operate at higher stress levels than the N610/Alumina composite alone. Extensive fiber pullout in both tensile and creep test fracture surfaces indicates the monazite coating is providing the weak fiber/matrix interface needed to cause the fibers to debond readily from stress intensities caused by oncoming matrix cracks. While the monazite coating has improved creep resistance by a large amount, the composite only exhibits acceptable creep behavior for 900^{o}C or below. At that temperature it can achieve a creep life of at least 100 h for creep stresses at or below 67% of its tensile strength. This corresponds with Johnson et al, who say that "the diffusional creep of the fine grain oxides is simply too high at temperatures above ~900^{o}C to be useful" (20:33)

Recommendations

Fine grained oxide fibers, such as Nextel 610, have been shown to exhibit high strength, but poor creep resistance when compared to Si-based non-oxide fibers. However, recently developed fibers, such as Nextel 720, have demonstrated adequate creep resistance between 1000^{o}C and 1200^{o}C (20:47), with the benefit of inherent

oxidation resistance. The increased creep resistance of N720 fibers is better than that of other oxide fibers due to its mullite content (~55 vol%), which is a secondary phase existing as needles (elongated grains) surround the alumina grains. Both the presence of a secondary phase and the elongated grains have shown to improve creep resistance (20:33). Creep is inhibited by the resistance to the sliding motion of grains during creep. Uninhibited grain motion produces crack-like cavities and wedge shaped flaws. Increased test temperature and stress level enhance this damage process (32:349).

In recent years, N720 fibers have been tested mainly in aluminosilicate matrices, which is more creep resistant than a pure alumina matrix (27). A type of aluminosilicate that has shown promise as a matrix material in recent years is Mullite ($3Al_2O_3 \cdot 2SiO_2$). Mullite and N720 fibers (which contain mullite grains), used together would produce a composite with very little thermal mismatch, with coefficients of thermal expansion of 5.3 x $10^{-6}/^oC$ and 6 x $10^{-6}/^oC$ respectively (9). This would result in less microcracking during processing of the composite.

Creep resistance could be improved by the addition of monazite fiber coating, shown by Boakye et al not to degrade the N720 fiber at temperatures up to 1200^{o}C. Monazite coated N720 fibers also showed increased strength over uncoated fibers at 1200^{o}C heat treatments (6:2800).

A N720/Monazite/Mullite composite would possess much better creep resistance than the N610/Monazite/Alumina; however further research would need to be in order to increase the strength of the N720 fiber. Although the room temperature strength of the N720 fibers is less than that of the N610 fibers, at 1200^{o}C the single filament strength of N720 is ~1450 MPa, while the strength of N610 is only ~830 MPa (20:32). N720

becomes the stronger fiber at approximately 950^{o}C, which is the temperature regime for use of CMCs. Similar targeted flaw reduction techniques, used to produce the high strength in the N610 fiber could be used to increase the strength of N720 fibers. Further efforts would need to be made to determine the effect of the larger grain size of N720, and flaw population on creep resistance. N720 fibers also provide a cost benefit over N610 fibers of $88/kg ($44/kg for > 455kg) (20:47).

Bibliography

1. "3M Fiber Selection Guide," in *3M Nextel Textile Notebook*. Product Brochure. St. Paul, MN: 3M Corporation, no date.

2. "3M Ceramic Fiber Typical Properties," in *3M Nextel Textile Notebook*. Product Brochure. St. Paul, MN: 3M Corporation, no date.

3. Adams, Donald F. and others. *Experimental Characterization of Advanced Composite Materials* (Third Edition). New York: CRC Press, 2003.

4. Boakye, E.E., M.D. Petry, R.S. Hay, and L.M. Douglas. "Monazite Coatings on Nextel 720, 610, and Tyranno-SA Fiber Tows: Effects of Precursers on Fiber Strength," *Ceramic Engineering Society Proceedings*, **21** [4]:229-36 (2000).

5. Boakye, Emmanuel, Randall S. Hay, and M. Dennis Petry. "Continuous Coating of Oxide Fiber Tows Using Liquid Precursers: Monazite Coatings on Nextel 720," *Journal of the American Ceramic Society*, **82** [9]: 2321-31 (1999).

6. Boakye, Emmanuel, Randall S. Hay, Pavel Mogilevsky, and L.M. Douglas. "Monazite Coatings on Fibers: II, Coating Without Strength Degradation," *Journal of the American Ceramic Society*, **84** [12]: 2793-801 (2001).

7. Cazzato, A, M. Colby, D. Daws, J. Davis, P. Morgan, J. Porter, S Butner, and B. Jurf.. "Monazite Interface Coatings in Polymer and Sol-Gel Derived Ceramic Matrix Composites," *Ceramic Engineering Society Proceedings*, **18** [3]:269-78 (1997).

8. Center of Lightweight Structures. "Natural Fibre Composites: From Upholstery to Structural Components." Excerpt from unpublished article. n. pag. http://www.clc.tno.nl/projects/recent/flax.html. Netherlands, no date.

9. Chawla, K. K. *Composite Materials Science and Engineering.* New York: Springer-Verlag, 1987.

10. Chawla, K.K., H. Liu, J. Janczak-Rusch, and S. Sambasivan. "Microstructure and Properties of Monazite ($LaPO_4$) Coated Saphikon Fiber/Alumina Matrix Composites," *Journal of the European Ceramic Society*, **20**: 551-59 (2000).

11. Chou, Tsu-Wei and Prashant G. Karandikar. "Damage Processes and Non-Linearity in Ceramic Matrix Composites," in *High-Temperature Ceramic-Matrix Composites I: Design, Durability, and Performance*. Ed. A.G. Evans and R. Naslain. Westerville, OH: The American Ceramic Society, 1995.

12. Davis, J.B., D.B. Marshall and P.E.D. Morgan. "Monazite-Containing Oxide/Oxide Composites," *Journal of the European Ceramic Society*, **20**: 583-87 (2000).

13. Davis, J.B., D.B. Marshall and P.E.D. Morgan. "Oxide Composites of Al_2O_3 and $LaPO_4$," *Journal of the European Ceramic Society*, **19**: 2421-26 (1999).

14. DiCarlo, James A. and Sunil Dutta. "Continuous Ceramic Fibers for Ceramic Matrix Composites," in *Handbook on Continuous Fiber-Reinforced Ceramic Matrix Composites.* Ed. Richard L. Lehman, Said K. El-Rahaiby, and John B. Wachtman, Jr.Westerville, OH: The American Ceramic Society, 1995.

15. Engesser, John Mark. *Monotonic, Creep-Rupture, and Fatigue Behavior of Carbon Fiber Reinforced Silicon Carbide (C/SiC) at an Elevated Temperature.* MS thesis, AFIT/GMS/ENY/04M-01. School of Engineering and Management, Air Force Institute of Technology (AU), Wright-Patterson AFB OH, March 2004.

16. Evans, A.G., F.W. Zok, and T.J. Mackin. "The Structural Performance of Ceramic Matrix Composites," in *High Temperature Mechanical Behavior of Ceramic Composites.* Ed. Shanti V. Nair and Karl Jakus. Boston: Butterworth-Heinemann, 1995.

17. Goldsby, J.C., H.M. Yun, G.N. Morscher, and J.A. DiCarlo. "Annealing Effects on Creep of Polycrystalline Alumina-Based Fibers," *Materials Science and Engineering*, **A242**: 278-83 (1998).

18. Herakovich, Carl T. *Mechanics of Fibrous Composites.* New York: John Wiley & Sons, Inc., 1998.

19. Holmes, J.W. and Xin Wu. "Elevated Temperature Creep Behavior of Continuous Fiber-Reinforced Ceramics," in *High Temperature Mechanical Behavior of Ceramic Composites.* Ed. Shanti V. Nair and Karl Jakus. Boston: Butterworth-Heinemann, 1995.

20. Johnson, David W. and others. *Ceramic Fibers and Coatings: Advanced Materials for the Twenty-First Century*. The National Academy of Sciences: Washington D.C., 1998.

21. Keller, Kristen A. Materials Engineer, AFRL/MLLN. Personal Communication. 15 January 2005.

22. Keller, Kristen A., Tai-Il Mah, Triplicane A. Parthasarathy, Emmanuel E. Boakye, Pavel Mogilevsky, and Michael K. Cinibulk.. "Effectiveness of Monazite Coatings in Oxide/Oxide Composites After Long-Term Exposure at High Temperature," *Journal of the American Ceramic Society*, **86** [2]: 325-32 (2003).

23. Keller, K.A., T. Mah , T.A. Parthasarathy, E.E. Boakye, and M. Cinibulk. "Evaluation of All-Oxide Composites Based on Coated Nextel 610 and 650 Fibers," *Ceramic Engineering Society Proceedings*, **22** [3]:667-75 (2001).

24. Keller, Kristin A., Triplicane A. Parthasarathy, Tai-Il Mah, Michael K. Cinibulk, and E.E. Boakye. "Evaluation of Monazite Fiber Coatings in Dense Matrix Composites," *Ceramic Engineering Society Proceedings*, **20** [3]:451-61 (1999).

25. Kerans, Ronald J. and Triplicane A. Parthasarathy. "Crack Deflection in Ceramic Composites and Fiber Coating Design Criteria," *Composites: Part A: Applied Science and Manufacturing*, **30**: 521-24 (1999).

26. Kuo, Dong-Hau, Waltraud M. Kriven, and Thomas J. Mackin. "Control of Interfacial Properties Through Fiber Coatings: Monazite Coatings in Oxide-Oxide Composites," *Journal of the American Ceramic Society*, **80** [12]: 2987-96 (1997).

27. Levi, Carlos G., James Y. Yang, Brian J. Dalgleish, Frank W. Zok, and Anthony G. Evans. "Performance and Processing of an All-Oxide Ceramic Composite," *Journal of the American Ceramic Society*, **81** [8]: 2077-86 (1998).

28. Lewis III, David. "Continuous Fiber-Reinforced Ceramic Matrix Composites: A Historical Overview," in *Handbook on Continuous Fiber-Reinforced Ceramic Matrix Composites.* Ed. Richard L. Lehman, Said K. El-Rahaiby, and John B. Wachtman, Jr.Westerville, OH: The American Ceramic Society, 1995.

29. Schmidt, S., S. Beyer, H. Knabe, H. Immich, R. Meistring, and A. Gessler. "Advanced Ceramic Matrix Composites Materials for Current and Future Propulsion Technology Applications." *Acta Astronautica*, 55:409-420 (2004).

30. Schwartz, C., S.C. Lee, and P.V. Mosher. "Properties of Silicon Carbide Fiber Reinforced Carbon Composites," in *Damage and Oxidation Protection in High Temperature Composites: Volume 1.* Ed. G.K. Haritos and O.O. Ochoa. New York: The American Society of Mechanical Engineers, 1991.

31. Steel, Steven G. *Monotonic and Fatigue Loading Behavior of an Oxide/Oxide Ceramic Matrix Composite.* MS thesis, AFIT/GMS/ENY/00M-02. School of Engineering and Management, Air Force Institute of Technology (AU), Wright-Patterson AFB OH, March 2000.

32. Suresh, S. “High Temperature Crack Growth in Unreinforced and Wisker-Reinforced Ceramics Under Cyclic Loads,” in *High Temperature Mechanical Behavior of Ceramic Composites.* Ed. Shanti V. Nair and Karl Jakus. Boston: Butterworth-Heinemann, 1995.

33. “Turbine Engine Technology.” Informational Pamphlet. Wright-Patterson AFB, OH: AFRL/PRT, no date.

34. Upadhya, K. “High Performance High Temperature Materials for Rocket Engines and Space Environment,” in *Processing, Fabrication & Application of Advanced Composites.* Ed. K. Upadhya. Materials Park, OH: ASM International, 1993.

35. Wilson, D.M. and L.R. Visser. “High Performance Oxide Fibers for Metal and Ceramic Composites,” *Composites Part A: Applied Science and Manufacturing*: 1005-1013 (1995).

36. Zawada, Larry P., Randall S. Hay, Shin S. Lee, and James Staehler. “Characterization and High-Temperature Mechanical Behavior of an Oxide/Oxide Composite,” *Journal of the American Ceramic Society*, **86** [6]: 981-90 (2003).

37. Zawada. L.P. and Lee, S.S. “The Effect of Hold Times on the Fatigue Behavior of an Oxide/Oxide Ceramic Matrix Composite,” in Thermal and Mechanical Test Methods and Behavior of Continuous-Fiber Ceramic Matrix Composites, ASTM 1309. Ed. Jenkins, M.G. and others, American Society for Testing and Materials, Philadelphia, PA, 1996.

38. Zolandz, Robert and Richard L. Lehman. “Crystalline Matrix Materials for Use in Continuous Filament Fiber Composites,” in *Handbook on Continuous Fiber-Reinforced Ceramic Matrix Composites.* Ed. Richard L. Lehman, Said K. El-Rahaiby, and John B. Wachtman, Jr.Westerville, OH: The American Ceramic Society, 1995.

REPORT DOCUMENTATION PAGE

Form Approved
OMB No. 074-0188

1. REPORT DATE *(DD-MM-YYYY)*	**2. REPORT TYPE**	**3. DATES COVERED** *(From – To)*
21-03-2005	**Master's Thesis**	Aug 2003 – Mar 2005

TITLE AND SUBTITLE

Creep Behavior of an Oxide/Oxide Composite with Monazite Coating at Elevated Temperatures

5a. CONTRACT NUMBER

5b. GRANT NUMBER

5c. PROGRAM ELEMENT NUMBER

AUTHOR(S)

Musil, Sean, S., 1st Lt, USAF

5d. PROJECT NUMBER

5e. TASK NUMBER

5f. WORK UNIT NUMBER

7. PERFORMING ORGANIZATION NAMES(S) AND ADDRESS(S)
Air Force Institute of Technology
Graduate School of Engineering and Management (AFIT/EN)
2950 Hobson Way
WPAFB OH 45433-7765

8. PERFORMING ORGANIZATION REPORT NUMBER

AFIT/GAE/ENY/05-M14

9. SPONSORING/MONITORING AGENCY NAME(S) AND ADDRESS(ES)

AFRL/PRTC	AFRL/MLLN
Attn: Dr. Joseph Zelina	Attn: Dr. Ronald Kerans
1950 Fifth Street	2977 P Street
WPAFB OH 45433-7251	WPAFB OH 45433-7734

10. SPONSOR/MONITOR'S ACRONYM(S)

11. SPONSOR/MONITOR'S REPORT NUMBER(S)

12. DISTRIBUTION/AVAILABILITY STATEMENT
APPROVED FOR PUBLIC RELEASE; DISTRIBUTION UNLIMITED.

13. SUPPLEMENTARY NOTES

14. ABSTRACT

This study focuses on experimental investigation of stress-rupture behavior (creep response) of an oxide/oxide composite in a cross-ply (0/90) lay-up at elevated temperature. The test material, Nextel 610/monazite/alumina composite, employs monazite, an oxidation-resistant interfacial coating designed to improve performance at elevated temperatures. The experimental program included monotonic tensile tests to failure and creep-rupture tests at elevated temperatures. Tensile tests served to establish an ultimate tensile strength (UTS) for the material. The ensuing creep-rupture tests involved stress levels at varying percentages of the UTS. Stress-rupture curves at 900 and 1100°C were established. A family of creep curves for various constant stress levels at 900 and 1100°C was produced. Composite microstructure, as well as damage and failure mechanisms were also investigated.

15. SUBJECT TERMS
Ceramic Matrix Composites, Composite Materials, Ceramic Coatings, Ceramic Fibers, Ceramic Materials, Fiber Reinforced Composites, Monazite, Creep, Oxides

16. SECURITY CLASSIFICATION OF:			**17. LIMITATION OF ABSTRACT**	**18. NUMBER OF PAGES**	**19a. NAME OF RESPONSIBLE PERSON**
REPORT	**ABSTRACT**	**c. THIS PAGE**			Dr. Marina B. Ruggles-Wrenn, AFIT/ENY
U	**U**	**U**	**UU**	126	**19b. TELEPHONE NUMBER** *(Include area code)* (937) 255-3636, ext 4641; e-mail: marina.ruggles-wrenn@afit.edu

Standard Form 298 (Rev: 8-98)
Prescribed by ANSI Std. Z39-18